

BOSTON UNIVERSITY
COLLEGE OF ENGINEERING

Dissertation

**NEXT GENERATION NEAR INFRARED (NIR) AND SHORTWAVE
INFRARED (SWIR) WEARABLES FOR BREAST CANCER IMAGING**

by

SAMUEL S. SPINK

B.S., University of Rhode Island, 2017
M.S., Boston University, 2020

Submitted in partial fulfillment of the
requirements for the degree of
Doctor of Philosophy

2023

© 2023 by
Samuel S. Spink
All rights reserved, except for Chapter 2,
which is © 2021 by SPIE and Chapter 4,
which is under review by SPIE (2023)

Approved by

First Reader

Darren Roblyer, Ph.D.
Associate Professor of Biomedical Engineering
Associate Professor of Electrical and Computer Engineering

Second Reader

Irving Bigio, Ph.D.
Professor of Biomedical Engineering
Professor of Electrical and Computer Engineering

Third Reader

David Boas, Ph.D.
Professor of Biomedical Engineering
Professor of Electrical and Computer Engineering

Fourth Reader

Adam T. Eggebrecht, Ph.D.
Associate Professor of Radiology
Washington University in St. Louis

Fifth Reader

Naomi Ko, M.D., M.P.H.
Associate Professor of Medicine
Boston University School of Medicine

DEDICATION

I would like to dedicate this work to my incredible family and friends, as they, above all,
have made my life so fulfilling.

ACKNOWLEDGMENTS

To Darren, thank you for taking me on as a Ph.D. student with no prior optics experience and being a supportive, helpful, and fair mentor over the last six years. You have provided me with invaluable knowledge and experience, but, more importantly to me, you have governed your lab in a manner that has offered the perfect balance of independence and direction, all while motivating via support and constructive criticism rather than unnecessarily harsh discipline. I am very grateful for the work environment you have created, and your leadership by example.

To current and former BOTLab members, I thank you for all the helpful conversations, cathartic experiment venting sessions, and even friendships that have formed. And a special thanks to Matt, who provided the initial direction and mentorship I needed during my rotation in Darren's lab to realize just how cool optics can be.

To my committee members: Irving Bigio, David Boas, Adam Eggebrecht, and Naomi Ko – thank you for constructive feedback over the last four years. In addition to committee meetings, I want to thank Irving for partaking in weekly joint lab meetings with our lab, and Adam for meeting with me 1-on-1 on numerous occasions via Zoom.

To Mom, Dad, Gram, Auntie Jan, Uncle Jimmy, Adam, and Liz – thank you all for the love, support, security, opportunities, and laughs you have given me over my 28 years thus far. I am forever grateful for having such an amazing family that cares so much for me. I love you all unconditionally.

And to my many incredible friends, past and present, thank you for making every day worthwhile. I live for shared moments with the people I love, and my friends and

family have provided with far too many to count. I look forward to all of the moments to come.

**NEXT GENERATION NEAR INFRARED (NIR) AND SHORTWAVE
INFRARED (SWIR) WEARABLES FOR BREAST CANCER IMAGING**

SAMUEL S. SPINK

Boston University College of Engineering, 2023

Major Professor: Darren Roblyer, Ph.D., Associate Professor of Biomedical
Engineering, Associate Professor of Electrical and Computer
Engineering

ABSTRACT

Neoadjuvant chemotherapy (NAC) is a common breast cancer treatment that involves administering chemotherapy for 3-6 months prior to surgery. This treatment enables more breast-conserving surgeries and even allows for the omission of surgery in some cases. However, about 31% of patients receiving NAC do not respond to the treatment. Therefore, there is a need for real-time methods to predict treatment response and improve patient outcomes. Over the last two decades, diffuse optical imaging has been investigated as a potential solution to this problem. This noninvasive and inexpensive technology uses near or shortwave infrared (NIR or SWIR) light to illuminate tissue, and detects multiply-scattered photons. However, bulky instrumentation and complicated imaging procedures have limited the clinical adoption of this technology. Furthermore, measured biomarkers including oxy- and deoxy-hemoglobin (HbO₂ and HHb, respectively), water, and lipid, have had mixed results in terms of prognostic capability. To address these limitations, a new wearable optical probe technology was developed and validated in this project, including a high-optode density NIR probe for monitoring hemodynamics and a first-generation SWIR probe for

quantifying water and lipid. Measurements on tissue-mimicking channel flow phantoms confirmed the ability of the NIR probe to quantify absorption contrast in vitro, and a cuff occlusion measurement demonstrated sensitivity to HbO₂ and HHb in vivo.

Hemodynamic oscillations at the respiratory rate were also explored in healthy volunteers and breast cancer patients as a potential new biomarker. It was demonstrated that traditional and novel breathing-related hemodynamic metrics provide tumor contrast and can potentially track treatment response. A deep-learning algorithm was developed to extract water and lipid concentrations from multi-distance SWIR measurements. The SWIR probe was validated by comparing measured water and lipid concentrations against ground truth values in emulsion phantoms. This work represents a significant step toward the development of technologies for frequent breast cancer treatment monitoring in the clinic and potentially at home.

TABLE OF CONTENTS

DEDICATION.....	iv
ACKNOWLEDGMENTS	v
ABSTRACT.....	vii
TABLE OF CONTENTS.....	ix
LIST OF TABLES... ..	xiii
LIST OF FIGURES.....	xiv
CHAPTER ONE: BACKGROUND AND SIGNIFICANCE	1
1.1 Breast cancer.....	1
1.1.1 Breast cancer prevalence and staging	1
1.1.2 Breast cancer treatment and subtypes	2
1.1.3 Treatment response monitoring	5
1.2 Diffuse optical imaging overview.....	6
1.2.1 Diffuse optics theory	6
1.2.2 Overview of DOI characteristics and modalities	7
1.2.3 Continuous wave DOI and DOT.....	8
1.3 DOI in breast cancer treatment monitoring	11
1.3.1 Review of longitudinal breast cancer studies involving DOI	11
1.3.2 Paced breathing: overview and potential as prognostic biomarker	13
1.3.3 Limitations to current DOI technologies	16
1.4 Portable and wearable NIRS devices	17
1.5 Shortwave infrared diffuse optical imaging.....	18

CHAPTER TWO: A HIGH OPTODE-DENSITY WEARABLE DIFFUSE OPTICAL PROBE FOR MONITORING PACED BREATHING HEMODYNAMICS IN BREAST TISSUE.....	20
2.1 Introduction.....	22
2.2 Instrument design.....	25
2.2.1 Wavelength selection.....	25
2.2.2 Optode topology.....	26
2.2.3 Printed circuit board (PCB) design.....	28
2.2.4 Biocompatible probe housing.....	30
2.3 System characterization and validation.....	31
2.3.1 Performance testing.....	31
2.3.2. In vitro validation with flow phantoms.....	35
2.3.3 In vivo validation with cuff occlusion.....	39
2.4 Paced breathing hemodynamics in healthy breast tissue.....	42
2.4.1 Breast tissue depth penetration modeling.....	42
2.4.2 Healthy volunteer breast study: paced breathing.....	44
2.4.3 Healthy volunteer breast study: hemodynamic metric quantification.....	48
2.5 Discussion.....	51
2.6 Supplementary Information.....	58
CHAPTER THREE: INITIAL CLINICAL FEASIBILITY STUDY.....	63
3.1 Introduction.....	63
3.2 Healthy volunteer repeatability and variation study.....	63

3.3 Longitudinal monitoring of NAC patients in the clinic	67
3.4 Discussion.....	71
CHAPTER FOUR: A SHORTWAVE INFRARED DIFFUSE OPTICAL WEARABLE	
PROBE FOR QUANTIFICATION OF WATER AND LIPID CONTENT USING DEEP	
LEARNING.....	
4.1 Introduction.....	76
4.2 Comparison of SWIR and NIR in simulation.....	78
4.2.1 Wavelength and source-detector separation selection for simulation.....	78
4.2.2 Simulation workflow	79
4.2.3 Forward and inverse models: Monte Carlo and deep neural network	80
2.4 Simulation results.....	83
4.3 Instrument design and characterization	83
4.3.1 Printed circuit board and probe housing	83
4.3.2 Performance characterization.....	85
4.4 In vitro validation.....	87
4.3.1 Water-in-oil emulsion phantoms.....	87
4.4.2 Dilution of oil-in-water emulsion with D ₂ O	90
4.5 Discussion.....	92
4.6 Supplementary Information	96
CHAPTER FIVE: CONCLUSIONS AND FUTURE DIRECTIONS	
5.1 Conclusions.....	97
5.2 Future directions	98

APPENDIX.....	101
BIBLIOGRAPHY...	103
CURRICULUM VITAE.....	116

LIST OF TABLES

Table 2.1. System characteristics of high-optode density wearable probe. Dynamic range, drift, and precision refer to mean values across all 392 S-D pairs. *Cited from our prior work [84].....	34
Table S2.1. Depth penetration estimates using photon hitting density (PHD) from simulations.....	60
Table 3.1. Patient characteristics.....	68
Table 4.1. Performance characteristics of SWIR probe. SNR and drift values are shown for just the shortest and longest S-D separations (7 mm and 16 mm).....	86
Table S4.1. Parameters that describe the training data used for each of the DNNs in this study.....	96

LIST OF FIGURES

- Figure 2.1. a) Simulated optode topologies. Tomographic reconstruction results for ΔHHb (b) and ΔHbO_2 (c) from various simulated chromophore perturbations in an embedded inclusion (tumor). Simulation ground truth is indicated on the y-axes and reconstructed values are indicated on the x-axis..... 28
- Figure 2.2. Bottom (a) and top (b) copper layers of rigid-flex PCB, as well as back (c) and tissue-facing (d) sides of encased probe. The dimensions of the bare PCB are $\sim 6\text{ cm} \times 6\text{ cm}$, while the encased probe is 8 cm in diameter and 1 cm thick. e) The peripheral control box, with two probes connected via HDMI cable. The dimensions of the box are 42.9 cm x 32.5 cm x 14.5 cm. f) The wearable probe attached to the curved surface of human bust model.. 29
- Figure 2.3. Signal to noise for probe source-detector separations. Horizontal displacement (jitter) within an S-D separation was added for ease of visualization, and does not reflect true S-D separation variation. 32
- Figure 2.4. Results from flow phantom experiments for channels whose upper edge were (a) 7 mm, (b) 19 mm, and (c) 28 mm below the background phantom surface. Only 850 nm data is shown. The first column, labeled “Channel $\Delta\mu_a$ ”, depicts the mean $\Delta\mu_a$ values as a function of time across all S-D pairs that probe the width of the channel. Flow began after ~ 0.5 minutes. For each S-D separation (going from 22 mm to 50 mm), the sample sizes (number of S-D pairs within channel) were as follows: n=28, 12, 20, 20, 18. The second column, labeled “Final $\Delta\mu_a$ ”, shows the mean and standard deviation of channel $\Delta\mu_a$ values at the final time point of the flow experiment. The third column, labeled “Channel Contrast”, depicts spatial contrast as a function of S-D separation. The final column shows a topographic reconstruction of the final $\Delta\mu_a$ values (in x-y space) for each channel depth, each shown for the S-D separation that corresponded to the highest final $\Delta\mu_a$. For (a), this was 22 mm, for (b) this was 41 mm, and for (c), this was 50 mm. The colorbar represents $\Delta\mu_a$ in units of mm^{-1} , and the horizontal dashed lines indicate the true boundaries of the channel 38
- Figure 2.5. Results from cuff occlusion experiment on healthy volunteer. The top row depicts the mean time traces (solid lines) and standard deviations (shaded regions) for ΔHbO_2 (red) and ΔHHb (black) across all channels with a S-D separation of (a) 22 mm (n=72), (b) 36 mm (n=40), and (c) 50 mm (n=24). d) Topographic

reconstructions from 22 mm separations showing changes in ΔHbO_2 (upper row) and ΔHHb (lower row) spatially and temporally, with the four pairs of frames referring to the time points designated by the four black arrows in (a). The first column is during baseline, second column just before the end of the occlusion, third column shortly after the end of occlusion, and fourth column the final time point. The colorbar is in units of μM , and each frame represents a 50 mm x 50 mm area. 41

Figure 2.6. Depth at 10% of peak photon-hitting density, grouped by wavelength and S-D separation. 43

Figure 2.7. a) Paced breathing protocol. The grey rectangle between the probe and right breast represents the worn phantom. b) Representative example of band-pass filtered mean $\Delta\mu_a$ time traces from a right breast measurement for 750 nm (red) and 850 nm (black) at 22 mm S-D separation. Each time trace is the mean across $n=72$ S-D pairs. The vertical dashed lines indicate the start and end of paced breathing at 0.05 Hz. c) The time traces for the 22 mm S-D separation for the contralateral worn phantom on breast measurement. d) Boxplots showing the distribution of SAR values across all S-D pairs and trials for the breast measurements, grouped by S-D separation. The horizontal line inside the boxplots indicates the median, while the edges of the box indicate the 25th and 75th percentiles. Whiskers extend to the minimum and maximum values. For breast SARs, total number of S-D pairs from S-D=22 mm to S-D=50 mm that met the QC criteria (and thus are included in this figure) are as follows: $n=1616, 620, 804, 616, 418$. e) Representative example of band-pass filtered mean $\Delta\mu_a$ time traces from a right leg measurement at 22 mm S-D separation. f) The time traces for the contralateral worn phantom on leg measurement. g) Same boxplots as in (d), but for leg SARs. The total number of S-D pairs are: $n=1242, 482, 616, 420, 248$ 48

Figure 2.8. a) Band-pass filtered mean time traces of ΔHHb (black) and ΔHbO_2 (red) for a right breast measurement from a healthy volunteer. Each time trace is the mean value across all 72 channels that have a 22 mm S-D separation. Paced breathing at 0.05 Hz occurred between dashed lines, while normal breathing was performed before the first dashed line and after the second. b) The corresponding SO_2, resp topographic map at 22 mm S-D separation for this trial. c) The same visualization presented in (a) for a different subject's left breast. d) The same visualization presented in (b) for the subject in (c). e) Distribution of ΔHbO_2 amplitudes across all S-D pairs and trials, presented in boxplots. Number of measurement points from S-D=22 mm to S-D=50 mm are as follows: $n=795, 309, 388, 303, 191$. f)

Distribution of ΔHHb amplitudes across all S-D pairs and trials. Number of measurement points are as follows: n=696, 273, 344, 260, 164. g) Distribution of SO_2 , resp values across all S-D pairs and trials. Number of measurement points are as follows: n=683, 272, 330, 255, 146. The horizontal line inside the boxplots indicates the median, while the edges of the box indicate the 25th and 75th percentiles. Whiskers extend to the minimum and maximum values. The insets show zoomed-in version on the boxes without the whiskers to better visualize relationships between hemodynamic metrics and S-D separation.....	50
Supplementary Figure S2.1. Simulation geometry utilized for optode configuration comparisons. The inclusion mimics a 35 mm diameter breast tumor embedded in healthy breast tissue.	58
Supplementary Figure S2.2 a) Side view of the silicone channel phantom with three channels at varying depths. The nominal depth refers to the distance between the surface of the phantom and the upper edge of the channel. b) Top view of the silicone phantom with right-angle tubing adapters connected to each channel. These enable the channels to be pre-filled with the first solution. Tubing is connected to the adapters for one of the three channels, showing how the syringe pump can dispense the second solution into the channel. Not shown here are the syringe pump, syringe, and waste container.....	59
Supplementary Figure S2.3 Results from flow phantom experiments for channels whose upper edge were (a) 7 mm, (b) 19 mm, and (c) 28 mm below the background phantom surface. Only 750 nm data is shown. The first column, labeled “Channel $\Delta\mu_a$ ”, depicts the mean $\Delta\mu_a$ values as a function of time across all S-D pairs that probe the width of the channel. Flow began after ~0.5 minutes. For each S-D separation (going from 22 mm to 50 mm), the sample sizes (number of S-D pairs within channel) were as follows: n=28, 12, 20, 20, 18. The second column, labeled “Final $\Delta\mu_a$ ”, shows the mean and standard deviation of $\Delta\mu_a$ values at the final time point of the flow experiment. The third column, labeled “Channel Contrast”, depicts spatial contrast as a function of S-D separation. The final column shows a topographic reconstruction of the final $\Delta\mu_a$ values (in x-y space) for each channel depth, each shown for the S-D separation that corresponded to the highest final $\Delta\mu_a$. For (a), this was 22 mm, for (b) this was 41 mm, and for (c), this was 50 mm. The colorbar represents $\Delta\mu_a$ in units of mm^{-1} , and the horizontal dashed lines indicate the true boundaries of the channel.	60

Supplementary Figure S2.4 Depictions of the deformable phantom described in Section 4.2. (a) View of phantom adhered to bust model. b) Top-view bust model/phantom shown in (a). c) Demonstration of the deformability of the phantom, with a finger making an indent into the phantom by pressing.	61
Figure 3.1. Coefficients of variation by subject for (a) StO ₂ and (b) SrO ₂ , and left breast to right breast ratio of these same metrics (c and d).	66
Figure 3.2. a) Spatial map of THb at baseline for Subject 3 on the tumor-bearing breast. b) Same map as (a), but for the contralateral unaffected breast. c) Spatial map of HbO ₂ ,PB/HbO ₂ -2,abs at baseline for Subject 2 on the tumor-bearing breast. d) Same map as (c), but for the contralateral unaffected breast.	70
Figure 3.3. Longitudinal trends in (a) StO ₂ , (b) SrO ₂ , and (c) HbO ₂ ,PB/HbO ₂ ,abs, normalized to baseline levels	71
Figure 4.1. Absorption of endogenous chromophores in healthy breast tissue from 600-1700 nm (for water and lipid) and 600-1300 nm (for HbO ₂ and HHb). Tissue concentrations for this example are as follows: water = 51.5%, lipid = 40%, HbO ₂ = 11.3 μM, HHb = 5.3 μM. The shaded region (980 nm – 1300 nm) refers to desired SWIR wavelength region for our probe design.	78
Figure 4.2. a) Simulation flowchart for the comparison of SWIR and NIR wavelengths. b) A table of architecture and training parameters for the DNNs used in this study. c) Loss (MSE) as a function of epoch during training for both the SWIR and NIR DNNs. d) All 25,000 recovered water values plotted vs. ground truth for SWIR and NIR wavelengths. e) Same as (d), but for lipid. f) Bar plots of the mean and standard deviation of differences between recovered and ground truth values for both SWIR and NIR.	82
Figure 4.3. a) Sample-facing and side views of the encased SWIR probe, with optical elements labeled. b) The probe attached to its external control hardware (the microcontroller) via HDMI. c) An example of how the probe might be worn on the forearm of a human subject with a Velcro strap.	85
Figure 4.4. Data processing flowchart for in vitro validation experiments.	88

Figure 4.5. a) Rd vs. lipid concentration for S-D separation = 7 mm. b) Same as (a), but for SD separation = 10 mm. c) Recovered water vs. true water. The inset zooms in on the 25% water data point, showing the length of the error bars. These error bars refer to the standard deviation across the 10 consecutive time points that were acquired for each phantom. All four subfigures have these error bars, but they are barely visible when zoomed out. d) same as (c), but for lipid recovery. 89

Figure 4.6. a) Rd vs H2O concentration for S-D separation = 7 mm. (b) Same as (a), but for S-D separation = 10 mm. c) Recovered H2O vs. ground truth compared to the identity line. For all subfigures, error bars are presented as the standard deviation across the 10 consecutive time points for each phantom measurement. Error bars are present but barely visible. 92

Figure A1. Tomographic reconstructions of channel flow phantom at final time point of experiment (nigrosin dye filling channel). The top row shows results for the channel whose upper edge was 7 mm from the surface of the background phantom, while the middle and bottom row show results for depths of 19 mm and 28 mm, respectively. The left slices show views along the length of the channel, the middle slices are cross-sectional views of the circular side of the channel, and the right slices are bird's-eye views of the channel. The colormap shows the reconstructed, normalized $\Delta\mu_a$ at each voxel. The regularization process distorts the scale of $\Delta\mu_a$, rendering the units arbitrary. The white dotted lines indicate the boundaries of the actual channel.. 102

CHAPTER ONE: BACKGROUND AND SIGNIFICANCE

1.1 Breast cancer

1.1.1 Breast cancer prevalence and staging

In 2020, it is projected that 276,480 new cases of invasive breast cancer will be diagnosed in the United States, and it is more broadly estimated that 1 in 8 women will be diagnosed with breast cancer in her lifetime [1]. Like other forms of cancer, breast cancer involves the rapid, uncontrolled growth and proliferation of cells, which results from genetic mutations. This uncontrolled growth generally leads to the formation of a mass of cancerous cells, known as a tumor. Breast cancers are often most broadly categorized based on the origin of the abnormal growth: cancer that originates in the lobules, or milk-producing glands, is referred to as lobular carcinoma, while cancer that originates in the ducts that connect lobules to the nipple is referred to as ductal carcinoma. Carcinoma in situ refers to cancer that has not spread outside of the origin source (lobules or ducts) or broken through the basement membrane, while invasive cancer has spread to, at a minimum, other regions of the breast. Breast cancer progression is generally categorized into five main stages (0 – IV) based on tumor size and spread into adjacent tissues, lymph nodes, and distant tissues [2]. As the cancer spreads to distal regions of the body, it becomes increasingly difficult for clinicians to cure. Locally advanced breast cancer (LABC) refers to cancer that has spread into the breast skin, chest wall, and/or axillary lymph nodes, but has yet to spread to organs outside of the breast tissue. This form of cancer is primarily of interest in this work. Statistics on locally advanced breast cancer are not well documented, but ~82,900 new cases of “regional” breast cancer (Stage II),

which has significant overlap in definition with LABC, will be diagnosed in the U.S in 2020 [3]. Some cases of Stage I and III breast cancer, depending on tumor size, are considered LABC, so this number is likely an underestimate.

1.1.2 Breast cancer treatment and subtypes

Breast cancer treatment strategies can vary greatly depending on a number of factors, such as molecular subtype, stage, age, menopausal status, biological and genetic characteristics, and patient preference. For carcinoma in situ, multiple treatment pathways may be employed, and the threat of progression is often unknown. Surgical removal of the cancerous tissue or radiation and/or hormone therapy are common. For invasive, late-stage metastatic cancer, systemic therapies are the primary form of treatment, with those being chemotherapy, targeted therapy, and hormonal therapy. However, in invasive, early-stage cancer, such as LABC, some combination of these therapies will be used prior to or after surgery [2]. Breast cancer molecular subtype has been shown to be particularly critical in the selection of treatment strategy. While there are many molecular subtypes that are being explored clinically, the most commonly identified subtypes refer to presence of hormone receptors (HR+/-) and amplification of the human epidermal growth factor receptor 2 (HER2+/-). Breast cancers lacking both the expression of HR and amplification of HER2 are known as triple negative breast cancers (TNBC). Each of these subtypes have different prognosis, pattern of spread, and treatment options.

Even with some form of therapy and surgery, the 5-year survival rate for LABC patients is 76% [4]. For this condition, it is becoming common to treat with neoadjuvant

chemotherapy (NAC) in order to reduce the size of the tumor at the time of surgery, enabling a more breast-conserving surgery, such as a lumpectomy instead of a mastectomy. From 2010 to 2015, the usage of NAC increased from 19.5% to 33.7% for TNBC patients, 21.5% to 39.8% for HER2+/HR- patients, and 17.0% to 33.7% for HER2+/HR+ patients [5]. However, for HER2-/HR+ patients, NAC usage only increased from 13.0% to 16.8% [5]. The prevalence of NAC usage varies with subtype due to the variation in treatment effectiveness as a function of subtype. Response to NAC is assessed through histopathology at the time of surgery, and may be classified as a pathologic complete response (pCR), partial response, or no response. It has been demonstrated that the pCR classification, which refers to the absence of residual cancer at the time of surgery, is well correlated with long-term survival, making it a very relevant measure of treatment response [6]–[9]. Data from the National Cancer Database indicates that while roughly 39% of HER2+/HR- and 23% of TNBC patients achieve pCR after NAC, only 0.3% of HER2-/HR+ patients exhibit pCR [10]. Therefore, most recent NAC studies have become particularly interested in improving outcomes for HER2+ and TNBC patients, with some recent clinical trials indicating that, with optimized treatment, pCR response rates may even be as high as 68% and 80%, respectively, for these subtypes [11], [12].

In order to improve outcomes and reduce the burden of toxic side effects of treatment to patients, the possibility of adaptive therapy, in which treatment strategy is dynamically altered as a function of treatment response, is the current standard of care. As noted by Esserman in a recent Clinical Cancer Research translation article, it would

be ideal to escalate and modify treatment for patients who are not responding to their current regimen, and de-escalate treatment for patients who are responding well [13]. The I-SPY-2.2 trial is a proposed trial that would include random assignment to alternative treatment regimens for patients who do not appear to be progressing toward a pCR outcome [13]. Of course, this necessitates the ability to predict pCR outcome during the initial NAC regimen, which is a primary source of motivation for the project described herein.

Beyond just altering treatment regimen to optimize outcomes prior to surgery, it has also been proposed that a pCR outcome may warrant the omission of surgery altogether. A review article by Heil et al. details the factors that must be considered when designing clinical trials that may justify this treatment strategy [14]. One challenge that this treatment pathway presents is that, historically, the surgically removed specimen was used to determine if pCR had been achieved. Therefore, omitting surgery due to the achievement of pCR would first require determining pathologic response through an alternative method. Multiple feasibility studies have already indicated that image-guided biopsies can identify pCR and non-pCR as a substitute for the assessment of surgical specimens, generally requiring 6-12 biopsies [15], [16]. One of these studies even exhibited 100% accuracy and 0% false negative rate across 34 patients [15]. As a result, there is currently an ongoing clinical trial that will omit surgery for patients who exhibit pCR after NAC (HER2+ and TNBC patients only), instead having them move directly to adjuvant whole breast radiation therapy [17]. If proven effective, this would be a major shift in breast cancer treatment strategy, and would only increase the value of being able to predict

treatment response as early as possible, so treatment strategies could be altered to allow for more pCR outcomes and fewer surgical procedures. Furthermore, as multiple biopsies still are associated with a significant degree of patient burden, alternative methods of predicting pCR during NAC and assessing pathologic response after the completion of NAC would be ideal, even if they may be used in concert with biopsy to reduce the total number of biopsies necessary.

1.1.3 Treatment response monitoring

While knowledge of treatment response at early time points during NAC could have significant value, the means of reliably tracking such a response are currently limited. Most forms of treatment response monitoring rely on tracking changes in tumor volume over time. Common methods of obtaining this information include palpation by a clinician and mammography, but there is often disagreement between these methods, and their predictive value with respect to pathologic response is fairly low [18]–[20]. Better correlated with pathologic outcome are metrics derived from magnetic resonance imaging (MRI), although these have been shown to have low specificity [21], [22]. Furthermore, there are two major limitations to the utility of MRI in predicting treatment response: (1) MRI-derived metrics are generally indicative of tumor size, but they lack sensitivity to other functional forms of tumor contrast that may precede changes in tumor size, and (2) it would be expensive, burdensome, and impractical to have frequent MRI-imaging as the standard of care for monitoring treatment response. Another form of imaging that has addressed the first limitation is fluorodeoxyglucose positron emission tomography (FDG-PET), which offers information related to the metabolism of tumors, and has been shown

have predictive power of treatment response within the first weeks of NAC [23], [24]. Still, the practical frequency of performing FDG-PET scans is a limiting factor, and it requires the use of a radioactive label. Over the last two decades, diffuse optical imaging (DOI), an imaging technique that uses near-infrared light to probe deep tissue metabolism and molecular characteristics, has been studied as a less expensive functional imaging modality for this application, and its clinical relevance with respect to predicting treatment response has shown great promise [25]–[28].

1.2 Diffuse optical imaging overview

1.2.1 Diffuse optics theory

Prior to expanding on the work that has been done with diffuse optical imaging in breast cancer, the principles and theory of diffuse optical imaging (DOI) will be broadly overviewed, and details pertinent to the work herein will be discussed. Light transport in biological tissue can be modeled with the radiative transport equation (RTE), which is an integro-differential equation that describes how light propagates in a volume that contains absorbing and scattering elements [29]. This equation, which is based on the law of conservation of energy, defines light radiance as a function of position, time, and direction of light travel, and it relates radiance to the underlying optical properties of tissue, namely the absorption and reduced scattering coefficients (μ_a and μ_s'). This equation is difficult to solve analytically, and numerical solutions are computationally expensive. However, if it can be assumed that the medium is highly scattering relative to its absorption, a diffusion approximation to the RTE can describe light transport in tissue

[30]. While most imaging modalities are primarily interested in rejecting scattered photons and only observing ballistic photons, DOI modalities relate diffusely scattered light intensity to the absorption and reduced scattering coefficients. Absorption can be further related to concentrations of absorbing agents, or chromophores, in tissue, and scattering can be related to tissue structure.

1.2.2 Overview of DOI characteristics and modalities

Some of the clinical strengths of DOI modalities are that they are label-free, noninvasive, and relatively inexpensive, making them very useful for frequent monitoring.

Additionally, detected photon depth penetration can extend up to multiple centimeters, allowing for functional imaging of subcutaneous tissue [31]. The trade-off comes primarily in the form of spatial resolution, which, depending on the number of light sources and detectors and their geometry, can range from approximately 0.5 to 10 mm [32], [33].

There are three primary forms of diffuse optical imaging, namely time domain (TD-DOI), frequency domain (FD-DOI), and continuous wave (CW DOI). For all three methods, the illumination wavelength is generally in the near-infrared window (~650-1000 nm). With TD-DOI, a pulse of light very short in duration is emitted into tissue, and a fast detector is used to assemble the temporal point spread function (TPSF) of reflected light some distance away from the source. With FD-DOI, the source illumination is modulated in time on the order of MHz, and the amplitude attenuation and phase delay of the reflected light signal is captured by a detector some distance away from the source. Both of these methods allow one to separate the effects of absorption and scattering, and

quantify each in an absolute manner. CW-DOI, on the other hand, simply involves the illumination of tissue with a constant light intensity, or light modulated at a very low (~kHz) frequencies, and the detection of the reflected intensity. This technique does not allow for the separation of absorption and scattering effects, and only relative changes in absorption can be computed [34]. For all of these methodologies, the number of sources and detectors can be varied to obtain enhanced spatial information. Despite the limitations of CW-DOI, it remains a very useful technique for monitoring dynamic changes in absorption, and relatedly hemoglobin, due its simplicity, inexpensive cost, potential for fast sampling, and ease of incorporation of a large number of sources and detectors [35]–[37]. The wearable probe being validated and tested in this proposal is a CW device, and thus this technique will be elaborated on in more detail.

1.2.3 Continuous wave DOI and DOT

CW-DOI, as previously stated, enables the extraction of relative changes in absorption. This technique is also often called near-infrared spectroscopy, or NIRS. It is common to incorporate many sources and detectors into a CW-DOI device in order to enable the reconstruction of spatial absorption maps, both topographically and tomographically. Here, topographic reconstruction typically refers to use of spatial interpolation of multiple point measurements each analyzed using the Modified Beer-Lambert Law (MBLL) to generate relatively low-resolution 2D spatial maps, while tomographic reconstruction refers to more complex methods of reconstructing 3D volumes. Many of the commercially and clinically available NIRS devices utilize the differential form of the MBLL (dMBLL) by default to compute changes in oxy- and deoxy-hemoglobin (HbO_2

and HHb) [38]. The dMBLL requires that assumptions be made about the initial optical properties of the sample, as well as constant scattering. The assumption that scattering is constant allows changes in detected light to be related to changes in absorption only. The dMBLL is presented below as Equation 1.1.

$$(1.1) \quad \Delta OD(t, \lambda) = -\log\left(\frac{I_t(\lambda)}{I_0(\lambda)}\right) = \Delta\mu_a^t(\lambda) \cdot DPF(\lambda) \cdot d$$

In this equation, $\Delta OD(t, \lambda)$ is optical density at time t and wavelength λ , while $I_t(\lambda)$ and $I_0(\lambda)$ refer to detected light intensity at time t and at baseline (or $t = 0$), respectively.

The term $\Delta\mu_a^{i,t}$ refers to the change in the i th absorption coefficient (with i being a wavelength index) at time t , while DPF and d are the differential pathlength factor and source-detector separation, respectively. The DPF is a wavelength-dependent parameter that linearly relates changes in absorption to changes in optical density, and it is dependent on sample optical properties. The formulation of the DPF that is used in this work is shown below as Equation 1.2.

$$(1.2) \quad DPF(\lambda) = \frac{1}{2} \left(\frac{\mu'_s(\lambda)}{\mu_a(\lambda)} \right)^{1/2} \left[1 - \frac{1}{\left(1 + d \cdot (3\mu'_s(\lambda) \cdot \mu_a(\lambda))^{1/2} \right)} \right]$$

Acquisition of data with multiple sources and detectors involves the employment of either time-multiplexing, frequency-multiplexing, or code-multiplexing to distinguish between unique source-detector pairs. The first mode refers to sequential scanning of

each optode (also referred to as source-detector pair, channel) such that only one optode is active at a given time. Frequency-multiplexing, on the other hand, involves the modulation of sources at unique low frequencies and subsequent demodulation of detected light, allowing for parallel optode activity. Code-multiplexing involves assigning a unique bit sequence to each source-detector pair. Frequency- and code-multiplexing allow for faster acquisition, but time-multiplexing is simpler to implement. While the dMBLL is certainly useful for obtaining hemodynamic information at individual points and in course 2D spatial regions, it is sometimes desirable to perform more complex 3D tomographic reconstructions in order to localize contrast to particular points in 3D space. While there exists a number of methods of performing diffuse optical tomography (DOT), the Rytov approximation in particular will be outlined here, for it is the primary form of tomography being investigated in this work. This is a linearization technique that relates perturbations in detected light intensity from unique source-detector pairs to changes in the absorption coefficient of individual voxels of a 3D volume through a sensitivity matrix. More specifically, the Rytov approximation models fluence in a medium as the product of an unperturbed, background fluence and an exponential term representing a perturbation [39]. To assemble the sensitivity matrix that relates changes in measured light to changes in absorption coefficient, a forward model of light propagation in a sample volume with baseline optical properties (matching those of the tissue or sample being measured) is employed, with the forward model of choice generally being the finite element method [40]. The inverse problem that must be solved to extract changes in absorption coefficient is ill-posed, however, for there are generally

thousands to hundreds of thousands of voxels, but only tens to hundreds of source-detector pairs [41]. Therefore, regularization and inversion algorithms must be implemented, with one common form of this inversion being the Moore-Penrose pseudo-inversion with Tikhonov regularization [33], [42].

1.3 DOI in breast cancer treatment monitoring

1.3.1 Review of longitudinal breast cancer studies involving DOI

Research in the field of DOI will now be linked to the previously outlined application of breast cancer treatment response monitoring. Many studies involving DOI as a tool for monitoring breast cancer treatment response have utilized FD-DOI or TD-DOI to obtain absolute concentrations of HbO₂, HHb, H₂O, and lipid content at baseline and time points leading up to the midpoint of NAC [25], [26], [28], [43]–[46]. While not always statistically significant, these studies have generally found that decreases in HHb and H₂O, and an increase in lipid at various time points between one week and midpoint of chemotherapy (compared to baseline) are well correlated with pCR. A composite metric known as the tissue optical index (TOI), defined as $[H_2O] * [HHb] / \text{lipid}$, has also been shown to reveal high tumor contrast, and its reduction at early time points during NAC is also well correlated with pCR [26], [47]. One of these studies even showed statistically significant optical contrast in HbO₂ between responders and non-responders as early as one day into chemotherapy [43]. Some studies have even shown that baseline tumor properties, namely tissue oxygen saturation (StO₂) and total hemoglobin (THb) alone may have predictive power with respect to tumor response [48], [49]. Data from a large,

multi-center study involving FD-DOI measurements indicated that predictive power of measurements *during* NAC may also depend on baseline values *before* NAC [28]. With respect to reported changes in hemoglobin, it is hypothesized that tumor metabolism as well as tumor vascular structure and integrity may be responsible for the observed changes.

More recently, the Hielscher Lab at Columbia university has been using CW-DOI to explore optical biomarkers derived from fast hemodynamics in response to breath holds, occurring on the order of seconds to tens of seconds [50]–[52]. This group has demonstrated that metrics derived from time-dependent breath hold hemodynamic response curves may be able to differentiate between healthy and cancerous breast tissue, and that these metrics can predict pCR at the two-week point of NAC with strong negative predictive value (94%) and moderate positive predictive value (71%). It was found that HHb increased during breath holds and subsequently decreased after releasing the hold, and that a faster rate of this HHb decrease correlates with pCR. A preclinical study of a rat breast cancer model supported these findings, demonstrating that changes in HbO₂ during simulated breath holds can differentiate treatment and control groups, and that furthermore this changes in this metric precede tumor volume changes [53]. During the simulated breath holds there was a decrease in HbO₂, and the magnitude of this decrease rose during tumor growth and lowered during treatment. Another demonstration of fast hemodynamic contrast came from a study that showed that compression-induced hemodynamics are able to differentiate responders from non-responders within the first month of chemotherapy [54]. It has been previously reported that tumor angiogenesis

generally produces abnormal vascular structures with heterogeneous permeability [55]. Vascular density, vessel diameter, and tortuosity are also known to vary in tumors when compared to healthy vasculature [56]. With this in mind, it is reasonable to believe that hemodynamics will vary between these tissue types in response to a perturbation.

1.3.2 Paced breathing: overview and potential as prognostic biomarker

One type of hemodynamic response which has yet to be well characterized in breast tissue is the response to the respiratory cycle. The respiratory cycle refers to cyclic inspiration and expiration, and respiration at a fixed frequency is known as paced breathing. During inspiration, contraction of primarily the diaphragm along with other secondary muscles results in ribcage expansion and rising of the chest, subsequent decrease of intrathoracic pressure, and resultant airflow into the lungs [57], [58]. Gas exchange occurs between alveoli in the lungs and capillaries, replenishing blood oxygen and removing carbon dioxide. Expiration, which generally is passive, refers to the return of the diaphragm to its relaxed position, pushing upward against the lungs, causing air to be expelled from them. Active expiration can also be performed, involving the recruitment of abdominal muscles to assist in the rise of the diaphragm in a manner that more forcibly expels air [59]. This cycle has effects on the cardiovascular system as well. The decrease in intrathoracic pressure brought on by inspiration is accompanied by an increase in the pressure gradient between the right atrium and systemic circulation, resulting in increased venous return, and right ventricular stroke volume [60], [61]. Furthermore, cardiac output increases during inspiration as a result of increased pulmonary resistance and resultant reduced left atrium filling [60], [62]. The inverse of

these trends occurs during expiration, and these respiratory-dependent trends are known to further affect heart rate variability (HRV) and arterial blood pressure, with inspiration causing increased heart rate and decreased arterial blood pressure [63].

The effect of these respiratory-induced cardiovascular changes on peripheral blood vessels is further detailed by Franceschini et al. and Wolf et al. [64], [65]. During inspiration, the decrease in intrathoracic pressure creates a pressure gradient between extrathoracic vessels and the intrathoracic vessels and the heart. As veins are ~20 times more compliant than arteries, this pressure difference primarily results in volume changes in venous compartments, decreasing venous blood volume while increasing venous return to the heart. Franceschini et al. notes that due to the presence of vein valves, the decrease in venous return during expiration does not match the increase during inspiration, creating a respiratory pump effect that modulates central venous pressure, and, resultantly, venous blood volume, at the respiratory rate.

While these cardiorespiratory trends exist regardless of the particular breathing rate, the magnitude of these effects has been shown to be respiratory rate-dependent in some cases. For example, it has been shown that the amplitude of HRV is dependent on the respiratory frequency, and that HRV amplitude generally peaks at a relatively low breathing rate of 0.1 Hz [66], [67]. Additionally, it has been demonstrated that slow, deep breathing can improve gas exchange efficiency by decreasing dead space [68]. A study that monitored blood oxygen saturation in subjects exposed to high altitude conditions found that arterial saturation increased during paced breathing at 0.1 Hz, compared to normal breathing rates [69]. Less explored is the effect of the particular respiratory rate

on amplitude of hemodynamic oscillations at that rate. It is possible that slower, paced breathing further increases the pressure gradients discussed between intrathoracic and extrathoracic vessels, resulting in increased amplitude of the induced volume oscillations. It has been previously reported that deep, paced breathing below typical spontaneous breathing rates should increase venous return, which supports the hypothesis that such deep paced breathing rates could increase the amplitude of venous volume oscillations [70]. As opposed to simply trending in one direction, it is also possible that the amplitude of such oscillations peaks at a particular slow paced breathing rate, but then may decline at even lower rates.

With respect to DOI, it has been previously shown that blood volume oscillations occurring at the respiratory rate during paced breathing can be detected in the brain and in periphery [71], [72]. Such oscillations have also been exploited to extract venous oxygen saturation in pigs, the thighs of human subjects, and in the brains of neonates [64], [65]. The hemodynamic response to paced breathing is currently unexplored, however, in breast tissue. It is evident that the respiratory cycle impacts systemic hemodynamics, and therefore it may be feasible to detect oscillations in breast tissue hemodynamics. With the previously described differences between tumor and healthy vasculature, metrics derived from these oscillations may prove to be novel sources of contrast between cancerous and healthy tissue. Additionally, paced breathing likely offers a more patient-friendly protocol when compared to breath holds, for many of the breath hold protocols involved 30-second breath holds, which can be very difficult and uncomfortable to perform. With all of this considered, from both a physiological and

practical standpoint, paced breathing hemodynamics are an exciting, and potentially promising, avenue to explore in search of new optical biomarkers for tumor contrast and treatment response. Part of the significance of this work lies in capitalizing on this minimally explored space.

1.3.3 Limitations to current DOI technologies

In addition to the lack of exploration that has been done related to breast tissue hemodynamics, there are other drawbacks to existing DOI technologies for monitoring breast cancer treatment response. The devices mentioned for all of these previous studies either require an operator to scan a handheld probe in a point-by-point manner over breast tissue to generate spatial maps [25], [26], [28], [43], [46], the patient to insert herself into a fixed, rigid optical fiber array in a prone position [44], [45], [49], or the patient to insert herself into a fixed, rigid optical fiber array while bending over [50]–[52]. Each of these configurations presents limitations. All of them lack ideal patient comfort, and each have other practical limitations. The handheld probe is portable to an extent, but it is incapable of taking fast measurements spatially due to the necessary point by point scanning. Fixed arrays of sources and detectors may allow for better temporal resolution, such as in the case of the Hielscher group, but portability and flexibility are limited, and patients may be less willing to attend multiple imaging sessions. The wearable device previously designed in the Roblyer lab addresses these issues by offering improved flexibility and portability while providing significant spatial information and temporal resolution. Therefore, its validation through this work may promote the path to more patient-

friendly, clinically practical DOI utility, which in turn may enable more rapid clinical adoption and acceptance of DOI.

1.4 Portable and wearable NIRS devices

Although a wearable DOI probe for breast cancer monitoring has remained elusive, a number of portable and wearable NIRS devices have been developed for other applications. Even as far back as 20 years ago, Chance et al. developed a portable NIRS device with 16 channels that was tethered via cable to external control hardware, and continued to push the technology forward with the fabrication of a single channel, battery-powered flexible device for hematoma detection, which afforded increased portability and improved tissue contact [73], [74]. Wireless wearable NIRS devices have also been designed and fabricated, with one such probe intended for measuring cortical activation consisting of 4 sources (2 LEDs x 2 wavelengths) and 4 detectors [75]. A number of commercial wireless, wearable devices are also now available, such as the Portamon from Artinis (Einsteinweg, Netherlands) and the MOXY from Fortiori Design (Hutchinson, MN, USA) [76], [77]. These devices both primarily are used for monitoring muscle oxygenation. The Portamon consists of 6 sources (3 LEDs x 2 wavelengths) and 2 detectors, and the MOXY consists of 4 sources (1 LED x 4 wavelengths) and 2 detectors. These devices are more concerned with point measurements of oxygenation than they are spatial contrast, limiting their utility for breast tumor hemodynamic monitoring. While not wireless, an ambulatory DOT device with 8 sources (4 LEDs x 2 wavelengths) and 8 detectors has shown to be able to track hemodynamics in muscle while running and performing of exercises [78]. While this

device offers more spatial information compared to the other mentioned devices, having 64 unique NIRS channels spanning different positions in lateral space, it is still a relatively low optode density compared to the stationary DOT system designed and used by the Hielscher lab to measure hemodynamics in breast tissue (32 sources, 64 detectors). There exists another wearable, wired NIRS device that has 16 sources (8 LEDs x 2 wavelengths) and 8 detectors, but the probe configuration is fixed to be worn on the forehead for monitoring brain activity [79]. The reason spatial information is so important is that locally advanced breast tumors are most commonly 2 cm to 4 cm in size [80]. In order to observe and localize tumor contrast, it is necessary to be able to measure a large region with high spatial sampling. It is evident that low optode-density, and relatedly limited spatial information, are the primary shortcomings of current wearable DOI and NIRS technology for the application of monitoring breast tumor hemodynamics. This further emphasizes the significance of this work, for a wearable device with the high optode-density exhibited by the probe developed in the Roblyer Lab has yet to be validated or used to measure breast hemodynamics, in a healthy or affected population.

1.5 Shortwave infrared diffuse optical imaging

Up to this point, the DOI modalities discussed have focused exclusively on the NIR wavelength region (~600-1000 nm) and have mostly focused on hemoglobin quantification. However, the shortwave infrared (SWIR) region (~900-2000 nm) has recently gained attraction in the DOI community, owed to the relatively lower scattering and prominent water and lipid-related absorption features. As water and lipid content

have been shown to be correlated with treatment outcomes for breast cancer patients receiving NAC, their improved quantification using SWIR technology is worth exploring as well.

Previous studies investigating the use of SWIR DOI for water and lipid estimation are few in number, but some have been performed. Nachabe et al. utilized a hyperspectral CW SWIR system from 900-1600 nm with spectral constraints to quantify water and lipid concentrations *in vitro* and *ex vivo* [81]. Prior work in our own lab has explored the use of spatial frequency domain imaging (SFDI) to estimate these same features [82].

While these studies have investigated the ability of various DOI modalities to quantify water and lipid content, a wearable SWIR probe remains elusive, which, for reasons described previously, would have a significant impact on the clinical adoption of this technology, and could even enable at-home monitoring. The final portion of the work described herein, therefore, will focus on the design and validation of a wearable SWIR probe for quantifying water and lipid content with deep learning.

**CHAPTER TWO: A HIGH OPTODE-DENSITY WEARABLE DIFFUSE
OPTICAL PROBE FOR MONITORING PACED BREATHING
HEMODYNAMICS IN BREAST TISSUE**

Significance: Diffuse optical imaging (DOI) provides in vivo quantification of tissue chromophores such as oxy- and deoxy-hemoglobin (HbO₂ and HHb, respectively). These parameters have been shown to be useful for predicting neoadjuvant treatment response in breast cancer patients. However, most DOI devices designed for the breast are non-portable, making frequent longitudinal monitoring during treatment a challenge. Furthermore, hemodynamics related to the respiratory cycle are currently unexplored in the breast and may have prognostic value.

Aim: To design, fabricate, and validate a high optode-density wearable continuous wave (CW) diffuse optical probe for the monitoring of breathing hemodynamics in breast tissue.

Approach: The probe has a rigid-flex design with 16 dual-wavelength sources and 16 detectors. Performance was characterized on tissue-simulating phantoms, and validation was performed through flow phantom and cuff occlusion measurements. The breasts of N=7 healthy volunteers were measured while performing a breathing protocol.

Results: The probe has 512 unique source-detector (S-D) pairs that span S-D separations of 10 - 54 mm. It exhibited good performance characteristics: μ_a drift of 0.34%/hr, μ_a precision of 0.063%, and mean SNR \geq 24 dB up to 41 mm S-D separation. Absorption contrast was detected in flow phantoms at depths exceeding 28 mm. A cuff occlusion measurement confirmed the ability of the probe to track expected hemodynamics in vivo.

Breast measurements on healthy volunteers during paced breathing revealed median signal-to-motion artifact ratios ranging from 8.1 dB to 8.7 dB. Median ΔHbO_2 and ΔHHb amplitudes ranged from 0.39 μM to 0.67 μM and 0.08 μM to 0.12 μM , respectively.

Median oxygen saturations at the respiratory rate ranged from 82% to 87%.

Conclusions: A wearable diffuse optical probe has been designed and fabricated for the measurement of breast tissue hemodynamics. This device is capable of quantifying breathing-related hemodynamics in healthy breast tissue.

This work presented in Chapter 3 was published in the journal: Journal of Biomedical Optics in 2021 [83] with the following authors and corresponding institutions:

Samuel S. Spink^{a,†}, Fei Teng^{b,†}, Vivian Pera^a, Hannah M. Peterson^a, Tim Cormier^c, Alexis Sauer-Budge^{c,‡}, David Chargin^c, Sam Brookfield^c, Adam Eggebrecht^d, Naomi Ko^e, Darren Roblyer^a

^a Boston University, Dept. of Biomedical Engineering, Boston, MA, 02215, USA

^b Boston University, Dept. of Electrical and Computer Engineering, Boston, MA, 02215, USA

^c Boston University, Fraunhofer Center for Manufacturing Innovation, Boston, MA, 02446, USA

^d Washington University, Dept. of Radiology, St. Louis, MO, 63110, USA

^e Section of Hematology and Oncology, Women's Health Unit, Boston Medical Center, 801 Massachusetts Ave, First Floor, Boston, MA, 02118, USA

†Authors contributed equally to this work

‡ Currently at Exponent, Inc., Biomedical Engineering and Sciences Practice, Natick, MA 01760, USA

2.1 Introduction

An estimated 82,900 new cases of locally advanced breast cancer (LABC) will be diagnosed in 2020 (this estimate refers to the number of projected “regional” breast cancer cases, which has significant overlap in definition with LABC) [3]. The ability to predict neoadjuvant chemotherapy (NAC) treatment response for these patients is considered an important unmet clinical need, especially as NAC becomes increasingly common [5]. Accurate treatment response monitoring could lead to adaptive therapies, in which treatment strategy is dynamically altered as a function of treatment response in order to improve outcomes and reduce the burden of toxic side effects on patient. As noted by Laura Esserman in a recent *Clinical Cancer Research Translation Article*, a benefit of the neoadjuvant setting is that “we can rapidly evaluate new and promising therapies, and escalate if treatment is suboptimal, avoiding additional toxic therapy if responses are excellent [13].” Of course, this necessitates technologies capable of tracking response longitudinally during treatment.

Diffuse optical imaging (DOI), also commonly referred to as near infrared spectroscopy, or NIRS, is a label-free, noninvasive, and relatively inexpensive functional imaging modality that has been explored as a method of predicting NAC treatment response in the clinic. DOI technologies are used to quantify concentrations of oxy- and deoxy-hemoglobin (HbO_2 and HHb), H_2O , and lipid content in tissue. Measurement

penetration depth can extend up to several centimeters, allowing for functional imaging of subcutaneous tumors [31]. The performance trade-off comes primarily in the form of spatial resolution, which, depending on the number of light sources and detectors and their geometry, can range from approximately 0.5 to 10 mm [32], [33]. While time-domain (TD) and frequency-domain (FD) DOI devices enable absolute quantification of absorption and scattering coefficients and chromophore concentrations, continuous wave (CW) systems can quantify only relative changes in absorption and chromophore concentrations, but are simpler and less expensive. Many prior studies have utilized FD-DOI or TD-DOI to obtain absolute concentrations of HbO₂, HHb, H₂O, and lipid content at baseline and time points leading up to the midpoint of NAC [25], [26], [28], [43]–[46]. These studies have generally found that decreases in HHb and H₂O, and an increase in lipid at various time points between one week and midpoint of chemotherapy (compared to baseline) are well correlated with a pathologic complete response (pCR). One of these studies even showed statistically significant optical contrast in HbO₂ between responders and non-responders as early as one day into chemotherapy [43].

There are a number of drawbacks to existing DOI technologies for monitoring breast cancer treatment response. Devices typically require an operator to scan a handheld probe in a point-by-point manner over breast tissue [25], [26], [28], [43], [46], or the patient to insert herself into a fixed, rigid optical fiber array in a prone position or while bending over [44], [45], [50]–[52]. These configurations may be awkward for the patient due to the required body position and/or the contact with an operator. The handheld probe is portable to an extent, but requires laborious point-by-point scanning.

Tomographic fixed arrays of sources and detectors allow for better temporal resolution with high spatial information, but portability and flexibility are limited, they require more space for usage and storage, and patients may be less willing to attend multiple imaging sessions. Wearable and portable DOI and NIRS technologies solve several of these issues, but most current technologies suffer from either low optode-density or poor mechanical fit to breast tissue, limiting their application in the monitoring of breast tumor hemodynamics [76]–[79]. We have previously developed a wearable probe that offers improved breast tissue contact by incorporating a rigid-flex printed circuit board [84], but this device was limited as it had only 12 sources and 1 detector that all share the same source-detector (S-D) separation.

In this work we developed a high optode-density wearable CW probe with 32 LED sources and 16 detectors. It is both mechanically flexible and able to provide high spatial resolution, and is suited to the dimensions of most locally advanced breast tumors [80]. We leveraged this new probe to explore paced breathing hemodynamics in breast tissue for the first time. It has been previously shown that blood volume oscillations at the respiratory rate during paced breathing can be detected in the brain and in periphery [71], [72]. Such oscillations have also been used to extract venous oxygen saturation in pigs, the thighs of human subjects, and in the brains of neonates [64], [65]. We hypothesize that metrics derived from these oscillations may prove to be novel sources of contrast between cancerous and healthy tissue in the breast. Additionally, compared to breath holds, which have recently been explored in the context of NAC monitoring [51], [52],

paced breathing offers a potentially more patient-friendly protocol, as it is easier to perform.

In the following sections we first describe the design and fabrication of the new high optode-density wearable probe. We then describe system characterization results, followed by both *in vitro* and *in vivo* validation through measurements on spatially-complex optical phantoms and the forearm of a healthy volunteer during a cuff occlusion. We then quantify breathing motion artifact, and lastly, quantify paced breathing hemodynamics in breast tissue through measurements on a group of seven healthy volunteers.

2.2 Instrument design

Factors considered in the design of the wearable probe included the tissue depth and sizes of locally advanced breast tumors, the near infrared absorption and scattering properties of human breast tissue, and the anticipated hemodynamic changes expected to occur. Design choices, methods, and results are described below.

2.2.1 Wavelength selection

The probe was designed to extract HbO₂ and HHb concentration changes. The choice of imaging wavelengths was determined in part by a condition number analysis previously shown to be useful for optimizing wavelength [35]. The condition number $\kappa(A)$ is defined in Equation 2.1 as:

$$(2.1) \quad \kappa(A) = \frac{\sigma_{max}(A)}{\sigma_{min}(A)}$$

where $A = \begin{pmatrix} \epsilon_{\lambda_1}^{\text{HbO}_2} & \epsilon_{\lambda_1}^{\text{HHb}} \\ \epsilon_{\lambda_2}^{\text{HbO}_2} & \epsilon_{\lambda_2}^{\text{HHb}} \end{pmatrix}$, the elements of A are the optical extinction coefficients for

HbO_2 and HHb at the chosen wavelength pair, and $\sigma_{\max}(A)$ and $\sigma_{\min}(A)$ are the maximum and minimum singular values of A . Extinction coefficients were taken from Zijlstra et al [85]. Optimized wavelength pairs correspond to a condition number closer to one. Dual wavelength pairs in the near infrared (NIR) wavelength band from 600 to 900 nm were tested using condition number analysis. 750 nm and 850 nm LEDs were chosen for the wearable probe based on their relatively small condition number (3.1) as well as the commercial availability of LEDs at these wavelengths.

2.2.2 Optode topology

The imaging probe was designed to measure the most prevalent tumor size ranges based on current epidemiological data, with a target range of 2 to 4 cm in diameter, which represent the 34 and 74 percentiles of locally advanced breast tumors sizes [80]. An overall probe diameter of 60 mm was chosen for all designs to accommodate a large range of tumor sizes.

Three optode topographies were considered and compared using Finite Element Method (FEM) simulations of a breast tumor hemodynamic challenge. The topographies are shown in Figure 2.1a and included a “12 pointed star” pattern, a “rectangular” pattern, and a “central rectangular” pattern. The “12-pointed star” pattern was an extension of our prior probe design which utilized a central hub with arms radiated outward [84]. Both the rectangular and central rectangular topographies have been utilized in prior tomographic NIRS systems for neuroimaging applications [86]–[89].

Each probe optode topology was tested using Nirfast, a Matlab software suite that utilizes FEM for numerically solving the photon diffusion equation [90]. A tumor-like inclusion was modelled on a homogeneous background and incremental increases and decreases in the inclusion absorption were simulated. The background HbO₂ and HHb concentrations were set to 15.6 μM and 5.2 μM , respectively, and were based on previously reported healthy breast tissue properties [91]. The inclusion was a 35 mm diameter sphere at a depth of 5 mm. Supplementary Figure S2.1 depicts this simulation geometry. HbO₂ was incremented or decremented by 3, 6, 9 and 12 μM and HHb was incremented or decremented by 1, 2, 3, or 4 μM . The magnitude of these changes roughly corresponds to the documented changes of chromophore concentrations for locally advanced breast tumors on the day one after their initial NAC infusion [43]. The reconstructed ΔHbO_2 and ΔHHb concentrations were compared with the ground truth for all simulations. Crosstalk between reconstructed ΔHbO_2 and ΔHHb was also evaluated. Scattering was assumed to be homogeneous and set to a wavelength-insensitive constant of 1 mm^{-1} for all simulations, which is a common reduced scattering coefficient for breast tissue [92].

Reconstructed chromophore changes were calculated within the 3D inclusion volume for FEM simulations conducted with each optode geometry. Results are shown in Figure 2.1b and 2.1c. Results were similar for each geometry with 35% to 40% of target changes recovered, meaning all geometries produced an underestimation of reconstructed ΔHbO_2 and ΔHHb . A 6 – 12 % crosstalk was observed between ΔHHb and ΔHbO_2 . The “central rectangular” pattern was chosen for the probe design because of the equivalent

simulation results and because of its relative ease of fabrication. This design has 7 S-D separation orders, ranging from 10 to 54 mm. There is a total of 512 unique S-D pairs.

2.2.3 Printed circuit board (PCB) design

The probe is shown in Figure 2.2. It was fabricated using a four-layer rigid-flex PCB

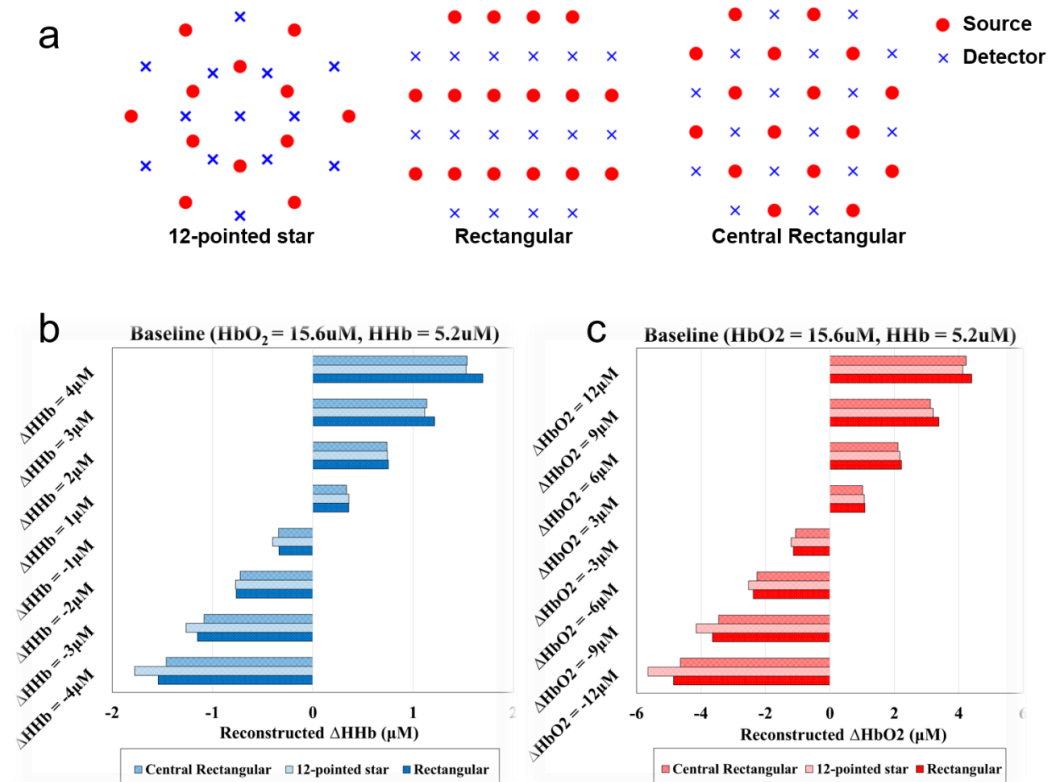


Figure 2.1. a) Simulated optode topologies. Tomographic reconstruction results for ΔHHb (b) and ΔHbO_2 (c) from various simulated chromophore perturbations in an embedded inclusion (tumor). Simulation ground truth is indicated on the y-axis and reconstructed values are indicated on the x-axis.

design. Nine rigid PCB “islands” are connected through 0.9 mm flexible connections that allow flexion between rigid neighbors. The bottom copper layer (shown in Figure 2.2a) is populated with several I²C compatible integrated circuits including an LED driver (MAX6964, Maxim Integrated), a bus buffer (PCA9600, NXP Semiconductors), and two analog multiplexers (MAX14661, Maxim Integrated). Additionally, MOSFET arrays

(SSM6N43FU, LF, Toshiba) are used to sequentially switch each LED. The middle layers of the PCB sit at the interface between the rigid and flexible substrates and facilitate trace routing.

The top copper layer (shown in Figure 2.2b) is populated with 32 LEDs (16 SMT750-23 and 16 SMT850-23, Roithner Lasertechnik) and 16 optical detectors (TSL250RD, ams). The LEDs are surface mount PLCC-2 packages with 750 nm and 850 nm center wavelengths. The detector is an 8-SOIC silicon photo detector module with a built-in transimpedance amplifier, and the maximum responsivity of this sensing module is $76.8\text{mV}/(\mu\text{W}/\text{cm}^2)$ at 770 nm.

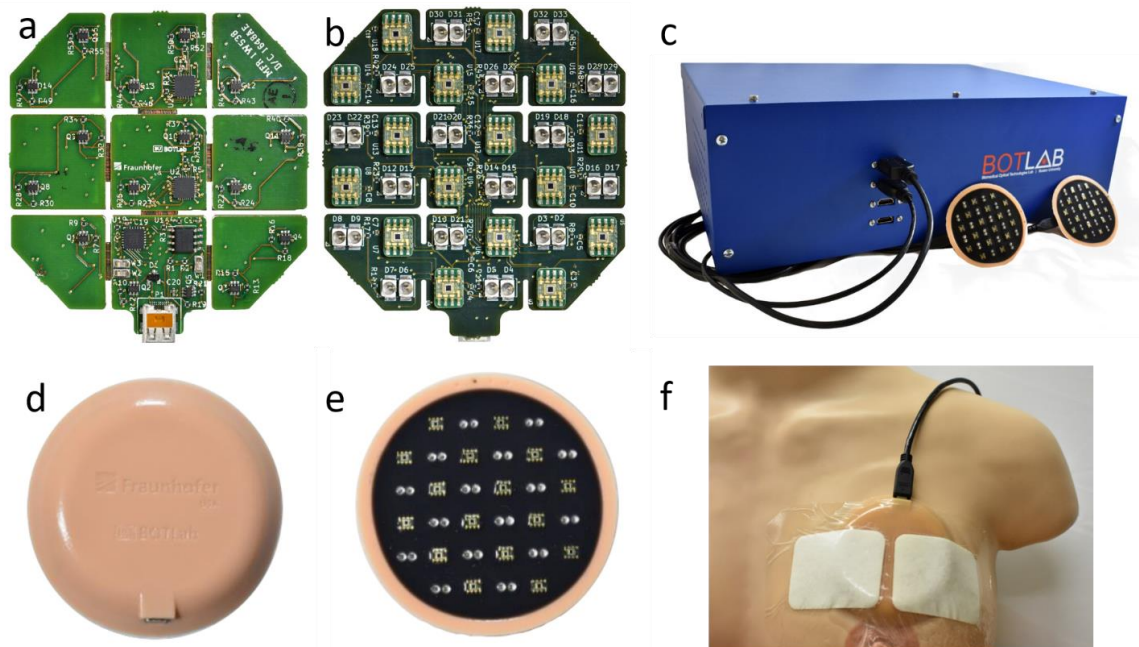


Figure 2.2. Bottom (a) and top (b) copper layers of rigid-flex PCB, as well as back (c) and tissue-facing (d) sides of encased probe. The dimensions of the bare PCB are $\sim 6\text{ cm} \times 6\text{ cm}$, while the encased probe is 8 cm in diameter and 1 cm thick. e) The peripheral control box, with two probes connected via HDMI cable. The dimensions of the box are $42.9\text{ cm} \times 32.5\text{ cm} \times 14.5\text{ cm}$. f) The wearable probe attached to the curved surface of human bust model.

The wearable probe communicates with a peripheral control box through an HDMI cable. A flexible ribbon micro-HDMI to micro-HDMI adapter cable connects directly to the probe, and then a more rigid micro-HDMI to HDMI cable connects the ribbon cable to the control box. The peripheral control box (shown in Figure 2.2c), powered externally by connection to a wall outlet, contains a DAQ board (USB-6361 OEM, National Instruments) with a 16-bit analog to digital converter, a current controller (FL591), and an Aardvark I²C adapter (TP240141, Total Phase). A custom Labview program on a PC sends commands via USB to both the DAQ board and Aardvark adapter. The Aardvark adapter communicates with the wearable probe via HDMI to control the sequential scanning of optodes, and analog signal from the probe is relayed back to the DAQ board, which digitizes the signal and sends it to the PC for data saving and display.

2.2.4 Biocompatible probe housing

The probe is designed to conform to the curved surface of breast tissue, and is potted and cured in a medical grade silicone housing. Figures 2.2d and 2.2e show the top and bottom sides of the probe encased in housing. It is made with skin-safe silicone (Ecoflex 00-30, Smooth-On Inc.) and pigments (Silc Pig, Smooth-On Inc.). The silicone and curing agent are mixed with the color dye, vacuumed, transferred to a 3D printed mold, further vacuumed and then cured. A black silicone layer is used on the bottom surface of the probe to reduce light crosstalk from emitters to detectors. The optical emitters and detectors protrude from the silicone surface by approximately 0.3 mm and indent the soft tissue of the breast. The total dimension is 8 cm wide and 1 cm thick, and its overall

weight is 41.8 grams. IV tape firmly secures the silicone probe over the curved surface of bust model as shown in Figure 2.2f.

2.3 System characterization and validation

2.3.1 Performance testing

The SNR of each S-D pair was evaluated using a custom silicone tissue-simulating phantom with optical properties that closely match reported healthy breast tissue values [91], [92]. These optical properties were confirmed using a benchtop frequency domain diffuse optical spectroscopy (FD-DOS) system [93], and were measured to be: $\mu_a = 0.006$ (750 nm), $\mu_a = 0.005 \text{ mm}^{-1}$ (850 nm) and $\mu'_s = 0.743 \text{ mm}^{-1}$ (750 nm), $\mu'_s = 0.635 \text{ mm}^{-1}$ (850 nm). Uncertainties for these (and subsequent) FD-DOS measurements are approximately 0.001 mm^{-1} , based on our prior work [94]. SNR was calculated according to Equation 2.2:

$$(2.2) \quad 10 \cdot \log_{10} \left(\frac{\text{mean}(V_p) - \text{mean}(V_d)}{\text{std}(V_p)} \right)$$

where V_p and V_d are the DC voltages collected for phantom and dark measurements, respectively. Phantom measurements were taken over the course of ~ 1 hour sampled at 0.2 Hz, while 5 dark measurements were taken sequentially at 0.2 Hz, prior to the phantom measurements. Dark measurements were taken with the LEDs off, and all measurements were taken under ambient fluorescent lighting. Figure 2.3 shows the results of this characterization, with mean SNR values of 27 dB, 26 dB, 27 dB, 24 dB, and 20 dB at the S-D separations of 22 mm, 30 mm, 36 mm, 41 mm, and 50 mm. SNR was at least 15 dB for all S-D pairs. At each separation order, SNR varied by as much as

11 dB, likely due to differences in optical coupling between the optical transducers and phantom.

We note that SNR and other performance metrics were determined for the 2nd to 6th order of optode separation, or roughly 22 mm to 50 mm separations. This included 392 S-D pairs (as opposed to all 512). These S-D pairs were typically used for physiological measurements, as 1st and 7th order optodes often experience optical detector saturation and low signal, respectively, on breast tissue. We also note that within each separation order the exact separation can vary up to ~3 mm due to the placement of the LEDs on the PCB. Optodes of the same separation are grouped order for ease of

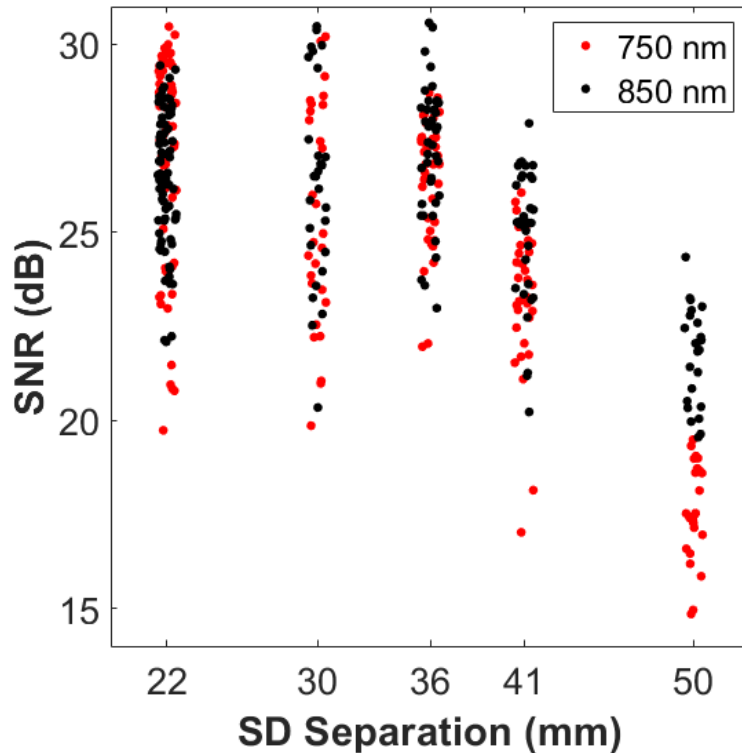


Figure 2.3. Signal to noise for probe source-detector separations. Horizontal displacement (jitter) within an S-D separation was added for ease of visualization, and does not reflect true S-D separation variation.

visualization, labeled with the mean separation. For example, the 2nd order, which refers to optodes whose separations range from ~21 mm to ~24 mm, will be labeled “22 mm”.

Other system performance characteristics are presented in Table 2.1. Dynamic range, drift, and precision metrics refer to the mean of the given metric across all 392 S-D pairs and were computed based on data collected during the same measurement described for the SNR calculation. Dynamic range was computed as the maximum measurable voltage of the photodiode (3.7 V) divided by the standard deviation of five sequential dark measurements.

For system drift and precision calculations, changes in voltages were first converted to $\Delta\mu_a$ values using the Modified Beer-Lambert Law (MBLL) [95], with the differential pathlength factor (DPF) computed based on the initial optical properties measured with the benchtop frequency domain system and the S-D separation [96]. Drift was calculated by computing the slope between the two endpoints of the 1-hour phantom measurement, with the starting point being the mean of the first 10 samples (~first 50 seconds) and the end point being the mean of the last 10 samples (~last 50 seconds). Slope values, in units of mm^{-1}/hr , were then normalized by the initial μ_a values at each wavelength to obtain percent change in μ_a (%/hr).

System precision was computed by first band-pass filtering the temporal $\Delta\mu_a$ and then calculating the standard deviation of the band-pass filtered signal. Precision was then reported as a coefficient of variation (%) by normalizing the standard deviation by the initial μ_a values each wavelength. The band-pass filter used was a 5th order Butterworth filter with cut-off frequencies of 0.045 Hz and 0.055 Hz. This filter was

selected in order to determine precision at 0.05 Hz, which is the breathing frequency of particular interest in subsequent physiological breast measurements.

The acquisition speed of the probe was determined by recording the time needed to sequentially scan the 392 S-D pairs of one probe. Normal operation of this system, however, involves the sequential scanning of two probes, so most measurements are acquired at a rate of 0.2 Hz, as opposed to 0.4 Hz. It should be noted that the forward current to LEDs can be dynamically altered to accommodate different S-D separations, and that the degree of forward current switching can alter acquisition speed. The cuff occlusion experiment described in Section 2.3.3 required no forward current switching, resulting in a higher acquisition rate of 0.33 Hz. Thermal characteristics shown in Table 2.1 are cited from our prior work [84].

Table 2.1. System characteristics of high-optode density wearable probe. Dynamic range, drift, and precision refer to mean values across all 392 S-D pairs. *Cited from our prior work [84].

Dimensions and Optodes		Performance Characteristics	
Diameter	80 (mm)	Dynamic Range	68 (dB)
Thickness	10 (mm)	Acquisition Rate	0.4 (Hz)
Wavelength	750/850 (nm)	Drift (μ_a)	0.34 (%/hr)
Total # Optodes	512	Precision (μ_a)	0.063 (%)
Orders of Optode Separation	7	Thermal Effect*	0.29 (%/°C)

2.3.2. *In vitro* validation with flow phantoms

Flow phantom experiments were performed to validate the ability of the wearable probe to quantify absorption at a range of depths and to localize absorption contrast spatially. A solid breast tissue mimicking phantom was fabricated (same optical properties as in section 2.3.1) that had three 10 mm diameter hollow channels at three depths. The depths were 7 mm, 19 mm, and 28 mm, with these depths referring to the distance between the surface of the solid phantom and the upper edge of the channel. The centers of the channels were laterally displaced by ~20 mm. Flow phantom experiments were performed by initially pre-filling the channels with a solution of 1% Intralipid in water, and then injecting a second solution containing 1% Intralipid, water, and nigrosin dye at a concentration of 0.05 mg/ml into one of the three channels. Supplementary Figure S2.2 depicts this flow phantom layout. The probe was adhered to the surface of the solid phantom with IV tape, centered above the channel through which the second solution was flowing. Baseline measurements were recorded for ~0.5 minutes at 0.2 Hz, after which a syringe pump controlled the dispensing of the nigrosin solution into one of the channels at a continuous rate while the probe continued to record measurements for ~3.5 minutes. This experiment was repeated for each of the three channels. The MBLL was used, as described previously, to convert raw data to $\Delta\mu_a$ values for each S-D pair.

Figure 2.4 shows results at 850 nm. The first column, labeled “Channel $\Delta\mu_a$ ”, shows time traces of mean $\Delta\mu_a$ values across all S-D pairs probing a location within the width of the channel. The location that a given S-D pair is probing is approximated as the midpoint (in x-y space) between the source and detector. There was a rise in $\Delta\mu_a$ at all

S-D separations at all three channel depths. The second column of Figure 2.4, labeled “Final $\Delta\mu_a$ ”, shows the mean and standard deviation of channel $\Delta\mu_a$ values at the final time point as a function of S-D separation. From Figure 2.4a, it is apparent that for a depth of 7 mm, the maximum detected change in absorption was captured by the 22 mm separation pairs. Figure 2.4b and 2.4c indicate that for depths of 19 mm and 28 mm, this maximum change was captured by 41 mm and 50 mm separation pairs, respectively. So, as expected, absorption contrast in deeper channels was better elucidated by longer S-D separations, due to the deeper penetration of detected photons at these longer separations.

The third column, labeled “Channel Contrast”, depicts a spatial contrast ratio as a function of S-D separation order. The contrast ratio equals the mean $\Delta\mu_a$ across S-D pairs that probe the channel divided by the mean of all pairs whose midpoints lie outside the channel. The spatial contrast for the 7 mm channel depth reached a maximum of 2.97 at a S-D separation of 22 mm, which dropped to 1.10 at a separation of 50 mm. For the 19 mm channel depth, the spatial contrast was overall reduced, with a maximum contrast of 1.76 at 22 mm separation, which reduced to 1.34 at 50 mm separation. For the 28 mm channel depth, the contrast was reduced further, with a maximum of 1.39 at 30 mm separation, which is also comparable to the ratios at 36 mm and 41 mm. For this channel depth, the minimum spatial contrast was observed at both the 22 mm and 50 mm separations (1.14 and 1.12). This figure depicts how spatial contrast is a function of both channel depth and S-D separation. Moving down the “Channel Contrast” column, one can see that as channel depth increased, the maximum achievable spatial contrast decreased. For a given channel depth, spatial contrast varied with S-D separation for a

number of reasons. Firstly, depth penetration increases with S-D separation, so spatial contrast was lower for S-D separations whose depth penetration did not reach the channel depth. Secondly, the approximation of the measurement location as the midpoint between source and detector becomes less accurate as S-D separation increases. For short S-D separations, this midpoint was relatively close to both source and detector, so the entire sample region probed by a given S-D pair was well approximated. At longer S-D separations, however, the midpoints were a less accurate approximation of the region being traversed by photons, and the longer photon path lengths blurred sources of absorption contrast that are smaller than the S-D separation. Relatedly, the coverage of the channel varied for different S-D separations, which is an artifact of the probe design and probe positioning. For example, for some 30 mm and 41 mm S-D pairs, both the source and detector for a given pair were positioned atop the true channel location. For all 36 mm S-D pairs, however, at least one of the two elements was laterally displaced from the channel, which means a smaller fraction of the photon paths traverse the channel. This explains the dip in spatial contrast ratio seen at 36 mm in Figure 2.4a and 2.4b.

Examples of topographic reconstructions of $\Delta\mu_a$ at 850 nm are presented in the final column of Figure 2.4. A single reconstruction incorporates only optodes that share the same S-D separation. For each flow phantom experiment, the separation group with the highest mean final $\Delta\mu_a$ within the channel (maximum point in second column of Figure 2.4), was visualized. In Figure 2.4a, this was 22 mm, in Figure 2.4b, this was 41 mm, and in Figure 2.4c, this was 50 mm. The midpoints between sources and detectors were used to approximate the measurement location of a S-D pair, as mentioned

previously, and then a cubic interpolation was performed between these points to generate the colormaps seen in the final column of Figure 2.4. Qualitatively, the highest $\Delta\mu_a$ values appear to be well localized to the ground truth channel location in Figure 4a and 4b, while spatial localization is less clear in the topographic map in Figure 2.4c. This is consistent with the spatial contrast ratios associated with these reconstructions. Videos of the topographic reconstructions over time for all three flow phantoms can be seen in

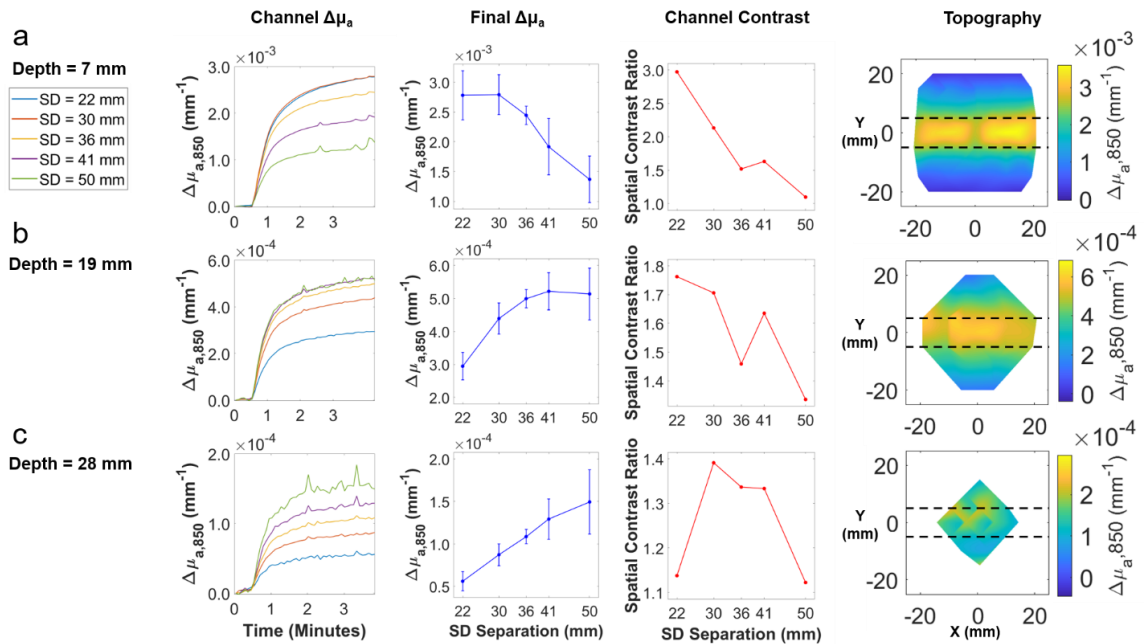


Figure 2.4. Results from flow phantom experiments for channels whose upper edge were (a) 7 mm, (b) 19 mm, and (c) 28 mm below the background phantom surface. Only 850 nm data is shown. The first column, labeled “Channel $\Delta\mu_a$ ”, depicts the mean $\Delta\mu_a$ values as a function of time across all S-D pairs that probe the width of the channel. Flow began after ~ 0.5 minutes. For each S-D separation (going from 22 mm to 50 mm), the sample sizes (number of S-D pairs within channel) were as follows: $n=28, 12, 20, 20, 18$. The second column, labeled “Final $\Delta\mu_a$ ”, shows the mean and standard deviation of channel $\Delta\mu_a$ values at the final time point of the flow experiment. The third column, labeled “Channel Contrast”, depicts spatial contrast as a function of S-D separation. The final column shows a topographic reconstruction of the final $\Delta\mu_a$ values (in x-y space) for each channel depth, each shown for the S-D separation that corresponded to the highest final $\Delta\mu_a$. For (a), this was 22 mm, for (b) this was 41 mm, and for (c), this was 50 mm. The colorbar represents $\Delta\mu_a$ in units of mm^{-1} , and the horizontal dashed lines indicate the true boundaries of the channel.

the Supplemental Information (<https://www.spiedigitallibrary.org/journals/journal-of-biomedical-optics/volume-26/issue-06/062708/High-optode-density-wearable-diffuse-optical-probe-for-monitoring-paced/10.1117/1.JBO.26.6.062708.full?tab=ArticleLinkSupplemental>), as well as the same figures presented in Figure 2.4, but for 750 nm data (Supplementary Figure S2.3). Tomographic reconstructions were not performed in this study, as it was decided that topographic reconstructions with the MBLI would serve as a simpler, more efficient first analysis of the probe performance, validation, and feasibility testing.

2.3.3 *In vivo validation with cuff occlusion*

A cuff occlusion experiment was performed on a healthy 25-year old male volunteer to validate the probe's ability to quantify hemodynamics *in vivo*. This measurement and all subsequent human subject measurements described were performed on subjects who gave written, informed consent under a protocol approved by the Institutional Review Board at Boston University. For this experiment, a pressure cuff was applied to the upper right arm (extending ~1-6 inches above the elbow), with the wearable probe adhered on the ventral proximal forearm with IV tape. For the first 2.5 minutes of the experiment, no pressure was applied to the cuff. The cuff pressure was then increased to 200 mmHg, where it remained for an additional 2.5 minutes. Pressure was then released, and an additional 2.5 minutes of recovery were monitored at zero pressure. Probe measurements were acquired at 0.33 Hz throughout the duration of the experiment. Beer's Law was used to calculate ΔHbO_2 and ΔHHb . The optical properties used to compute the DPF were as follows: $\mu_a = 0.021 \text{ mm}^{-1}$ (750 nm), $\mu_a = 0.023 \text{ mm}^{-1}$ (850 nm) and $\mu'_s = 0.72 \text{ mm}^{-1}$ (750

nm), $\mu'_s = 0.67 \text{ mm}^{-1}$ (850 nm). These optical properties are typical of the forearm region [97], [98].

Figure 2.5a shows the hemodynamic response to the cuff occlusion at a S-D separation of 22 mm. The red and black solid lines are equal to the mean ΔHbO_2 and ΔHHb values across all optodes sharing a 22 mm S-D separation, while the shaded region refers to the standard deviation across these optodes. It is evident that after the cuff pressure is increased, ΔHbO_2 decreased while ΔHHb increased, until the pressure was released at the 5-minute mark. At this point, ΔHbO_2 then rose and ΔHHb fell, over- and undershooting their baseline values, before eventually returning to near-baseline values. Figure 2.5b and 2.5c demonstrate that the magnitude of this response is decreased at longer separations of 36 mm and 50 mm, respectively. It is unclear if this attenuation with S-D separation is a true physiological phenomenon (i.e. hemodynamic response is greater in superficial tissues), or if signal is simply too noisy at longer S-D separations due to the presence of more attenuating muscle tissue. One-sample t-tests revealed statistically significant changes in ΔHbO_2 and ΔHHb just prior to pressure release at S-D separations of 22 mm, 30 mm, 36 mm, and 41 mm. The means and standard deviations in ΔHbO_2 for these S-D separations were $-6.91 \pm 7.09 \mu\text{M}$ ($p < 0.001$), $-5.93 \pm 6.40 \mu\text{M}$ ($p < 0.001$), $-2.24 \pm 4.56 \mu\text{M}$ ($p = 0.004$), and $-2.26 \pm 4.51 \mu\text{M}$ ($p = 0.008$). The corresponding mean changes in ΔHHb were $9.76 \pm 4.92 \mu\text{M}$ ($p < 0.001$), $7.99 \pm 4.49 \mu\text{M}$ ($p < 0.001$), $3.62 \pm 3.69 \mu\text{M}$ ($p < 0.001$), and $1.89 \pm 3.85 \mu\text{M}$ ($p = 0.009$).

Figure 2.5d shows topographic reconstructions for 22 mm separation optodes at various time points during the occlusion experiment. While the mean trends from the time traces indicate that ΔHbO_2 decreased and ΔHHb increased during the occlusion, the topographic maps at $T = 4.98$ minutes (the second pair of maps in Figure 2.5d) show that there is spatial variation of the hemodynamic response across the forearm locations. For

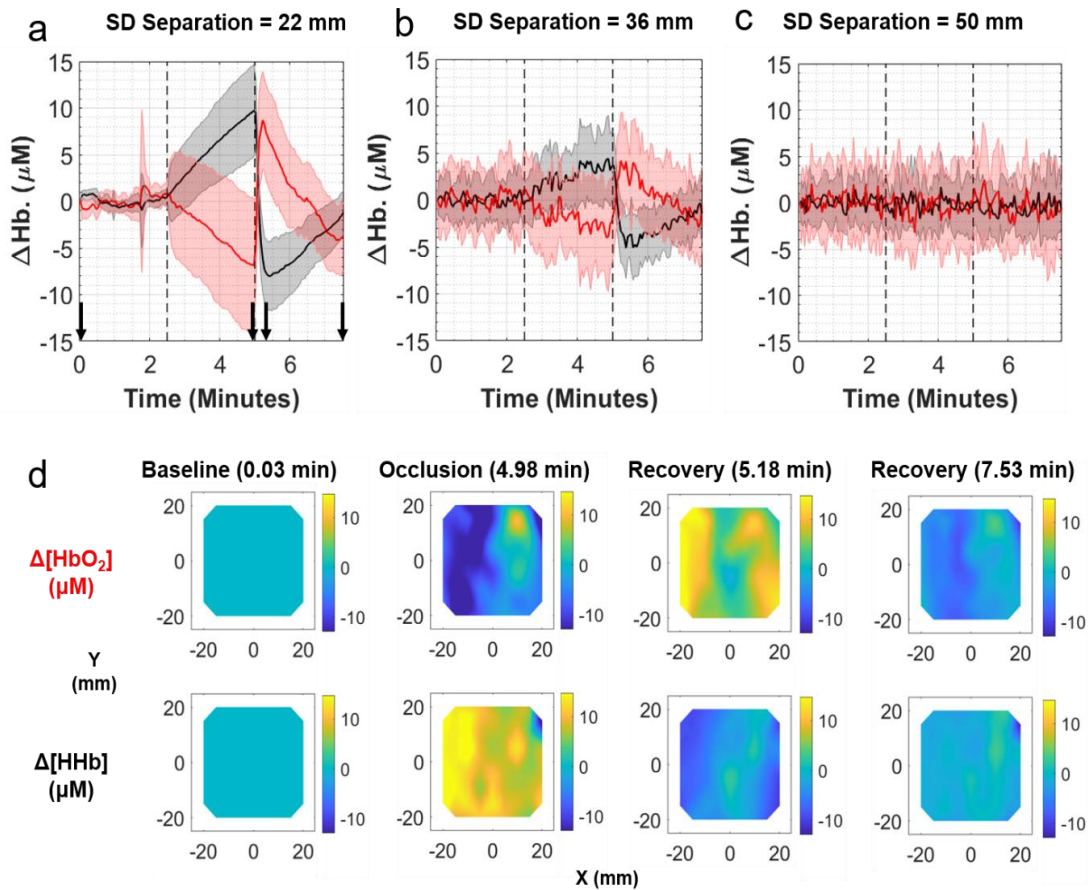


Figure 2.5. Results from cuff occlusion experiment on healthy volunteer. The top row depicts the mean time traces (solid lines) and standard deviations (shaded regions) for ΔHbO_2 (red) and ΔHHb (black) across all channels with a S-D separation of (a) 22 mm ($n=72$), (b) 36 mm ($n=40$), and (c) 50 mm ($n=24$). d) Topographic reconstructions from 22 mm separations showing changes in ΔHbO_2 (upper row) and ΔHHb (lower row) spatially and temporally, with the four pairs of frames referring to the time points designated by the four black arrows in (a). The first column is during baseline, second column just before the end of the occlusion, third column shortly after the end of occlusion, and fourth column the final time point. The colorbar is in units of μM , and each frame represents a 50 mm x 50 mm area.

example, it is interesting to note that at approximately $(x,y) = (10 \text{ mm}, 10 \text{ mm})$, there appears to be a rise in ΔHbO_2 in contrast with the surrounding decrease. A video of these topographic reconstructions at all five S-D separations over the duration of the occlusion can be found in the Supplemental Information (Supplementary Video S4, <https://www.spiedigitallibrary.org/journals/journal-of-biomedical-optics/volume-26/issue-06/062708/High-optode-density-wearable-diffuse-optical-probe-for-monitoring-paced/10.1117/1.JBO.26.6.062708.full?tab=ArticleLinkSupplemental>).

2.4 Paced breathing hemodynamics in healthy breast tissue

2.4.1 Breast tissue depth penetration modeling

Modeling was performed in order to quantify the approximate depth penetration of photons at the range of S-D separation orders available with the wearable probe. The photon hitting density (PHD) was calculated for a semi-infinite geometry using the Virtual Photonics Simulator (Virtual Photonics Initiative, Irvine, California) with the analytic solution to the standard diffusion approximation and an isotropic point source. A homogeneous sample was assumed, with the entire sample having identical breast optical properties. The simulated optical properties were as follows: $\mu_a = 0.0059 \text{ mm}^{-1}$ (750 nm), $\mu_a = 0.0074 \text{ mm}^{-1}$ (850 nm) and $\mu'_s = 0.88 \text{ mm}^{-1}$ (750 nm), $\mu'_s = 0.78 \text{ mm}^{-1}$ (850 nm). These optical properties are typical of breast tissue for premenopausal women [91], [92], which corresponds to the age range of the healthy volunteers in the subsequent breast measurements. A g value (anisotropy factor) of 0.8 was assumed, as well as an index of refraction of 1.4. A line profile of PHD perpendicular to the surface of the sample at the midpoint of the source and detector was assessed to quantify depth

penetration metrics. Along that profile, the location in depth of peak PHD was determined, as well as locations of 90%, 50%, and 10% of this peak, as described by Peterson et al [99].

The results from these simulations are listed in Supplementary Table S2.1. For all simulations, 750 nm and 850 nm pairs had similar depth penetrations, differing by at most 0.5 mm for S-D separation = 22 mm and by at most 1 mm at S-D separation = 50 mm. The peak PHD ranged from 4.3 to 9.5 mm with increasing S-D separation. 50% peak locations ranged from 9.4 mm to 19 mm across S-D separations, suggesting that sensitivity even at the shortest S-D separations can reach depths around 1 cm and beyond. Figure 2.6 depicts the 10% of peak PHD depths (indicative of the deepest simulated depth penetration), which ranged from 15.5 mm to 27.1 mm.

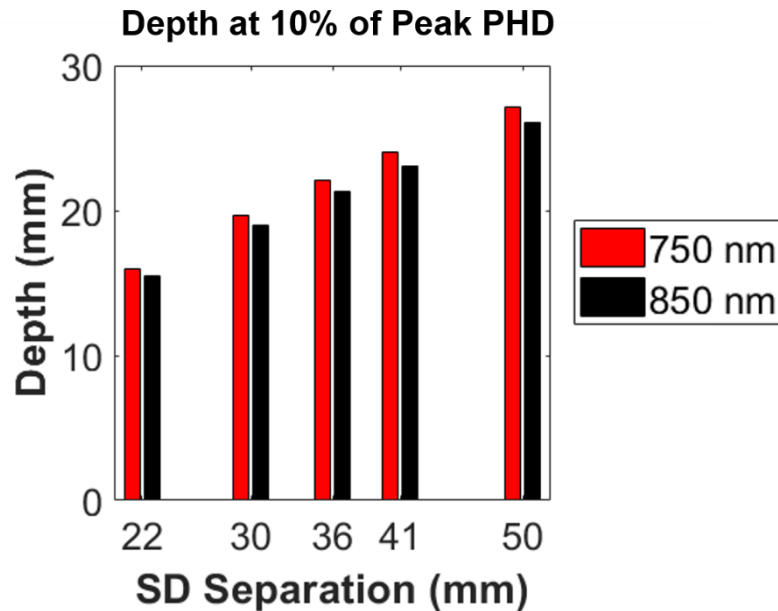


Figure 2.6. Depth at 10% of peak photon-hitting density, grouped by wavelength and S-D separation.

2.4.2 Healthy volunteer breast study: paced breathing

N=4 healthy female subjects were initially measured to determine if paced breathing hemodynamics could be quantified in breast tissue. Subjects were between the ages of 24 and 27. The subjects performed the following protocol: one wearable probe was adhered directly to breast tissue on one side with medical grade IV tape, with the lower edge of the probe centered at the upper edge of the areola. A second probe was adhered to the surface of a relatively small and deformable breast-simulating optical phantom (~9 x 9 x 1.5 cm), and this probe/phantom complex was adhered with additional IV tape to the contralateral breast in the same location. In order to simulate the interface between probe and breast tissue, this worn optical phantom was fabricated using a recipe that has been previously used to make phantoms with mechanical properties comparable to those of human breast tissue [100]–[102]. Demonstrations of this flexible phantom being adhered to a bust model and being deformed upon contact are shown in Supplementary Figure S2.4. The tissue-facing side of this worn phantom was lined with a layer of aluminum foil to ensure that photons did not penetrate tissue. The reasoning for this was that there would be no hemodynamic contrast in the phantom, but the probe/phantom complex would still experience torso/chest motion at the breathing frequency and generate optical signal from diffusely scattered light. Signal from the breast and contralateral phantom sides were then compared as a method of quantifying motion artifact. Probe measurements were taken at 0.2 Hz. Measurements were taken for 160 seconds at baseline (normal breathing), after which volunteers performed 8 cycles of paced breathing, with cycles consisting of a 5 second inhale, 10 second hold, and 5 second

exhale, yielding a slow breathing rate of 0.05 Hz. After the 8 cycles were completed, an additional 160 seconds of recovery (normal breathing) were monitored. This entire procedure was then repeated two additional times (3 trials total). The paced breathing was visually guided by an application on xhalr.org. Figure 2.7a summarizes this procedure. Of the four volunteers, two wore the probe/phantom complex on the right breast, while two wore the probe/phantom complex on the left breast. A breathing rate of 0.05 Hz was selected due to the limited bandwidth (0.1 Hz) of the system.

For each S-D pair from each trial of paced breathing, raw data was first converted to $\Delta\mu_a$ using the MBLL as described previously. The initial optical properties used for breast measurements were assumed to be the same as those used for simulations in Section 2.4.1. The optical properties for the worn phantom were measured by the same frequency domain device mentioned previously: $\mu_a = 0.007 \text{ mm}^{-1}$ (750 nm), $\mu_a = 0.007 \text{ mm}^{-1}$ (850 nm) and $\mu'_s = 0.933 \text{ mm}^{-1}$ (750 nm), $\mu'_s = 0.765 \text{ mm}^{-1}$ (850 nm). An FFT was then performed on the time points that corresponded to the duration of the paced breathing, and the amplitude peak nearest to 0.05 Hz was extracted (always a single bin in the FFT). Three quality control (QC) steps were performed at this stage in order to remove S-D pairs that did not meet the following criteria: pairs of adjacent 750 nm and 850 nm S-D pairs had to have 1) peak amplitudes that exceeded a frequency domain noise floor (approximated as the mean amplitude between 0.06 and 0.09 Hz); 2) peak locations that matched exactly (same frequency bin); and 3) peak amplitudes that exceeded the amplitude at the same frequency bin from the baseline breathing. Each S-D pair from the direct breast measurement that met these criteria was then compared to the

same S-D pair on the contralateral worn phantom, and a signal-to-artifact ratio (SAR) was computed according to Equation 2.3:

$$(2.3) \quad SAR = 10 \cdot \log_{10} \left(\frac{Amp_{breast,0.05Hz}}{Amp_{phantom,0.05Hz}} \right)$$

As a qualitative analysis, time-domain visualizations were also generated by band-pass filtering the entire time series. A 5th order Butterworth band-pass filter was used for all time trace filtering with a passband between 0.045 Hz and 0.055 Hz. The filter was generated using the “butter” function in Matlab (version 2018a), and filtering was performed using the “filtfilt” function, which performs forward and backward filtering of the time series in order to prevent phase distortion introduced by infinite impulse response (IIR) filters. The smoothing effect of this band-pass filter in both the forward and reverse directions artificially produces the symmetry observed in the time traces in Figures 2.7 and 2.8.

An additional group of N=3 female volunteers (ages 24-25) underwent the same protocol, except the probe and a more rigid optical phantom were adhered to the upper quadriceps of contralateral legs. Since leg motion is minimal during breathing compared to chest motion, a strong signal in this location would provide additional evidence that the probe is able to detect physiology related to paced breathing. This more rigid worn phantom had the following measured optical properties: $\mu_a = 0.005 \text{ mm}^{-1}$ (750 nm), $\mu_a = 0.003 \text{ mm}^{-1}$ (850 nm) and $\mu'_s = 0.709 \text{ mm}^{-1}$ (750 nm), $\mu'_s = 0.582 \text{ mm}^{-1}$ (850 nm). Optical properties of the rectus femoris were used when determining the DPF for

leg measurements, which were: $\mu_a = 0.012 \text{ mm}^{-1}$ (750 nm), $\mu_a = 0.012 \text{ mm}^{-1}$ (850 nm) and $\mu'_s = 0.70 \text{ mm}^{-1}$ (750 nm), $\mu'_s = 0.65 \text{ mm}^{-1}$ (850 nm) [103].

Representative examples of breast and contralateral phantom time traces from one subject are shown in Figure 2.7b and 2.7c, with 2.7b illustrating a clear rise in amplitude at both wavelengths during the paced breathing phase (between dashed vertical lines). Figure 2.7c shows the relatively low change in amplitude in the worn phantom. These traces are the mean values across all S-D pairs that share a 22 mm S-D separation. Figure 2.7e and 2.7f show the same type of representative examples for a subject from the leg measurement group. Overall, SAR values are relatively high for both breast and leg measurements, and the distributions of this metric in the two groups across all S-D pairs, all trials, and all subjects, are shown in Figure 2.7d and 2.7g. For breast measurements, there were 392 S-D pairs per trial x 3 trials per subject x 4 subjects = 4704 total S-D pairs analyzed. The median SARs for each S-D separation, from 22 mm to 50 mm, were 8.7 dB, 8.7 dB, 8.6 dB, 8.4 dB, and 8.1 dB. It should be noted that 86.6% of all S-D pairs from these breast measurements met the previously described QC criteria (the rest were not included in Figure 2.7d). 1.3% of all S-D pairs met the criteria but had a negative SAR, indicating the motion signal was higher than the breast signal. For leg measurements, there were only 3 subjects, so there were 3528 S-D pairs total. The leg SARs were overall higher than those of breast, with the medians at each S-D separation being 16.8 dB, 17.4 dB, 15.6 dB, 12.9 dB, and 9.0 dB. For the leg, 85.2% of S-D pairs met the QC criteria, while 0.2% had a negative SAR.

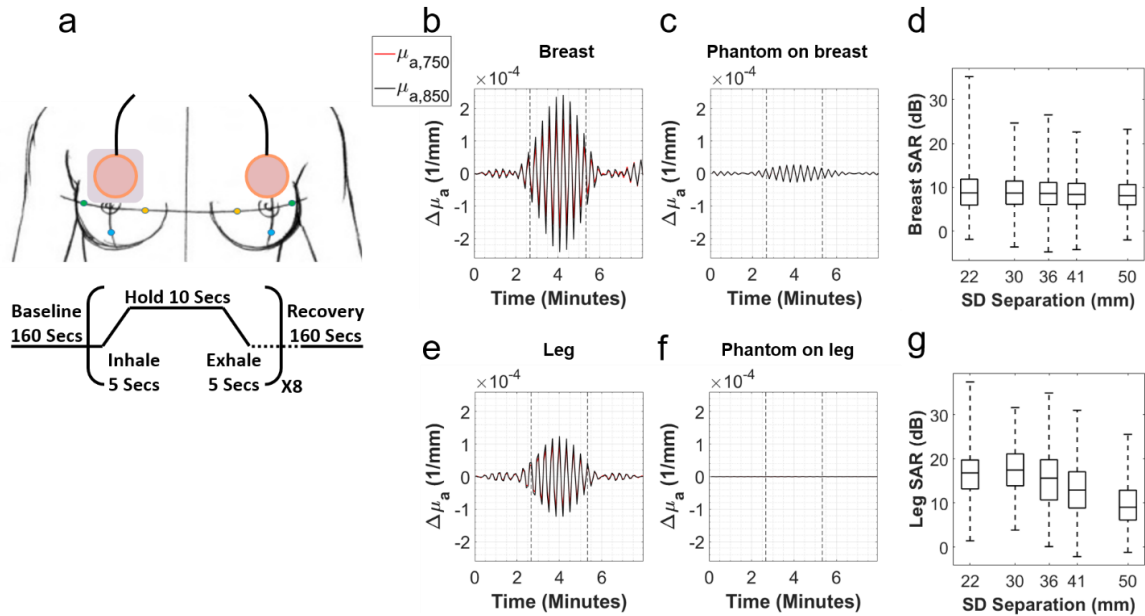


Figure 2.7. a) Paced breathing protocol. The grey rectangle between the probe and right breast represents the worn phantom. b) Representative example of band-pass filtered mean $\Delta\mu_a$ time traces from a right breast measurement for 750 nm (red) and 850 nm (black) at 22 mm S-D separation. Each time trace is the mean across $n=72$ S-D pairs. The vertical dashed lines indicate the start and end of paced breathing at 0.05 Hz. c) The time traces for the 22 mm S-D separation for the contralateral worn phantom on breast measurement. d) Boxplots showing the distribution of SAR values across all S-D pairs and trials for the breast measurements, grouped by S-D separation. The horizontal line inside the boxplots indicates the median, while the edges of the box indicate the 25th and 75th percentiles. Whiskers extend to the minimum and maximum values. For breast SARs, total number of S-D pairs from S-D=22 mm to S-D=50 mm that met the QC criteria (and thus are included in this figure) are as follows: $n=1616, 620, 804, 616, 418$. e) Representative example of band-pass filtered mean $\Delta\mu_a$ time traces from a right leg measurement at 22 mm S-D separation. f) The time traces for the contralateral worn phantom on leg measurement. g) Same boxplots as in (d), but for leg SARs. The total number of S-D pairs are: $n=1242, 482, 616, 420, 248$.

2.4.3 Healthy volunteer breast study: hemodynamic metric quantification

Data from the same $N=4$ healthy volunteers were further analyzed in order to quantify hemodynamic metrics related to paced breathing. Hemodynamics were only quantified for breast data, with worn phantom data excluded (one breast for each of four volunteers).

For each S-D pair in each trial of each subject, peak extraction of the $\Delta\mu_a$ amplitude at 0.05 Hz was performed in the same manner as described in Section 2.4.2. The same QC steps were employed as well, and, additionally, the noise floor was subtracted from each peak. Pairs of noise-subtracted $\Delta\mu_a$ amplitudes at 750 nm and 850 nm from adjacent optodes were then fit to Beer's Law to extract ΔHHb and ΔHbO_2 amplitudes. Oxygen saturation at the respiratory frequency, or $\text{SO}_{2,\text{resp}}$, was computed as $\Delta\text{HbO}_2 / (\Delta\text{HbO}_2 + \Delta\text{HHb})$. S-D pairs yielding negative ΔHbO_2 or ΔHHb amplitudes, or $\text{SO}_{2,\text{resp}}$ values below 0 or above 1 were discarded as an additional QC step.

Figure 2.8a shows overlaid time traces of ΔHbO_2 (red) and ΔHHb (black) at a S-D separation of 22 mm for the right breast of a volunteer. It is evident that the amplitude of ΔHbO_2 , and to a lesser extent ΔHHb , rose during the paced breathing phase of the protocol (between dashed vertical lines) compared to the baseline and recovery phases. Figure 2.8b shows a topographic reconstruction of $\text{SO}_{2,\text{resp}}$ for this same subject at 22 mm separation, generated using data from the entire duration of the 0.05 Hz paced breathing, showing high saturation throughout most of sampled region. In contrast, Figure 2.8c and 2.8d depicts the same time traces and topographic map for another subject whose $\text{SO}_{2,\text{resp}}$ was overall lower and more heterogeneous. Interestingly, the time trace for this subject appears to show a rise in amplitude toward the end of the recovery phase as well, which may be an artifact or a residual tendency to continue the paced breathing. Distributions of ΔHbO_2 amplitude, ΔHHb amplitude, and $\text{SO}_{2,\text{resp}}$ are shown in Figures 2.8e, 2.8f, and 2.8g, respectively, across all S-D pairs and trials from the N=4 subjects. For these distributions, there were 2352 ΔHHb and 2352 ΔHbO_2 values analyzed. ΔHbO_2

amplitude appears to decrease with S-D separation. The median ΔHbO_2 amplitudes for each S-D separation, from 22 mm to 50 mm, were 0.67 μM , 0.60 μM , 0.54 μM , 0.47 μM , and 0.39 μM . 84.4% of all ΔHbO_2 measurements met the QC criteria described previously, with excluded measurements being removed from these distributions. The median ΔHHb amplitudes were 0.12 μM , 0.09 μM , 0.08 μM , 0.08 μM , and 0.09 μM . For

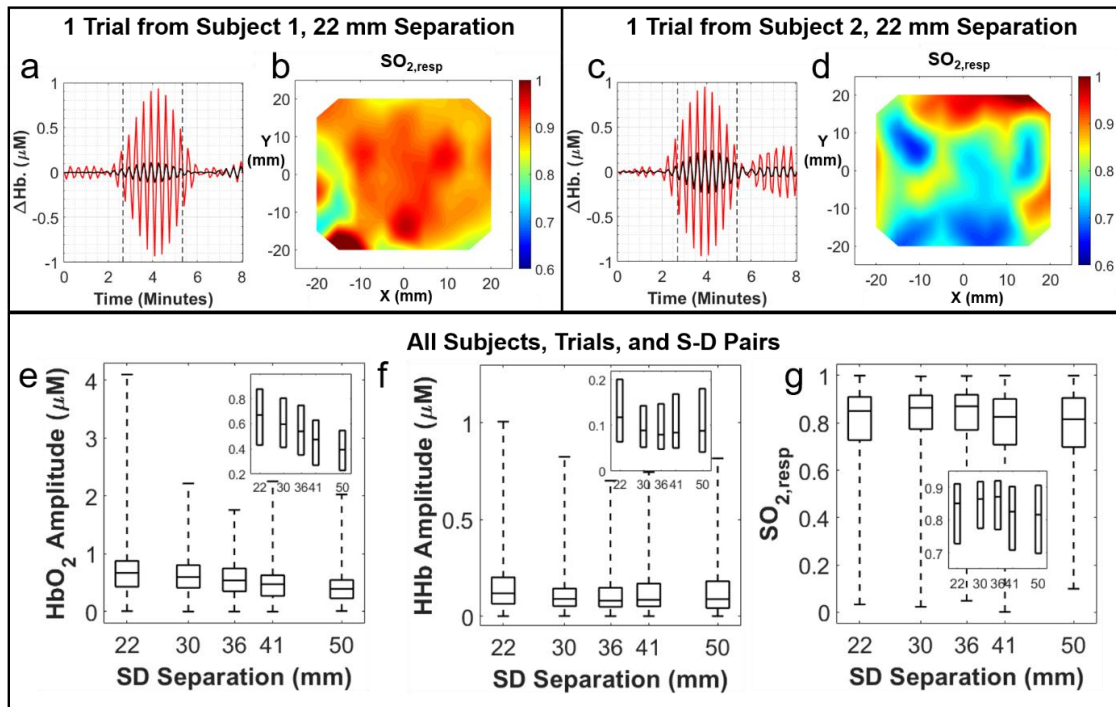


Figure 2.8. a) Band-pass filtered mean time traces of ΔHHb (black) and ΔHbO_2 (red) for a right breast measurement from a healthy volunteer. Each time trace is the mean value across all 72 channels that have a 22 mm S-D separation. Paced breathing at 0.05 Hz occurred between dashed lines, while normal breathing was performed before the first dashed line and after the second. b) The corresponding $\text{SO}_{2,\text{resp}}$ topographic map at 22 mm S-D separation for this trial. c) The same visualization presented in (a) for a different subject's left breast. d) The same visualization presented in (b) for the subject in (c). e) Distribution of ΔHbO_2 amplitudes across all S-D pairs and trials, presented in boxplots. Number of measurement points from S-D=22 mm to S-D=50 mm are as follows: n=795, 309, 388, 303, 191. f) Distribution of ΔHHb amplitudes across all S-D pairs and trials. Number of measurement points are as follows: n=696, 273, 344, 260, 164. g) Distribution of $\text{SO}_{2,\text{resp}}$ values across all S-D pairs and trials. Number of measurement points are as follows: n=683, 272, 330, 255, 146. The horizontal line inside the boxplots indicates the median, while the edges of the box indicate the 25th and 75th percentiles. Whiskers extend to the minimum and maximum values. The insets show zoomed-in version on the boxes without the whiskers to better visualize relationships between hemodynamic metrics and S-D separation.

ΔHHb , 73.9% of all measurements passed the QC criteria. While error in these measurements was not quantified directly, precision in $\Delta\mu_a$ for each wavelength and each S-D separation (derived from the previous drift measurement in Section 2.3.1), the extinction coefficients, and rules of error propagation were used to estimate uncertainty. For ΔHbO_2 , the uncertainties at each S-D separation were 0.03 μM , 0.02 μM , 0.03 μM , 0.03 μM , and 0.06 μM . For ΔHHb , they were 0.02 μM , 0.02 μM , 0.01 μM , 0.02 μM , and 0.03 μM .

The median $\text{SO}_{2,\text{resp}}$ values were 0.85, 0.86, 0.87, 0.83, and 0.82. For $\text{SO}_{2,\text{resp}}$, 71.7% of all measurements passed QC criteria. The computation of oxygen saturation metrics at AC frequencies generally assumes that ΔHbO_2 and ΔHHb are in-phase as a result of blood volume oscillations. While many measurements were in phase, the mean phase difference across all measurements that met the QC criteria was $19^\circ \pm 50^\circ$.

2.5 Discussion

We have described here a wearable continuous wave diffuse optical probe with 512 unique source-detector pairs ranging from 10 mm to 54 mm in S-D separation. Furthermore, we have demonstrated that hemodynamics related to the respiratory cycle can be quantified noninvasively *in vivo* in human subjects. Probe performance was characterized through measurements on tissue-simulating phantoms and validated *in vitro* through measurements on spatially complex flow phantoms and *in vivo* through a cuff occlusion measurement on a healthy volunteer.

There have been a number of portable and wearable NIRS devices developed for various medical applications. As far back as 20 years ago, Chance et al. developed a

portable NIRS device with 16 channels that was tethered via cable to external control hardware, and continued to push the technology forward with the fabrication of a single channel, battery-powered flexible device for hematoma detection, which afforded increased portability and improved tissue contact [73], [74]. A wireless, wearable NIRS device has also been fabricated for the purpose of measuring cortical activation [75]. A number of commercial wireless, wearable devices are also now available, such as the Portamon from Artinis (Einsteinweg, Netherlands) and the MOXY from Fortiori Design (Hutchinson, MN, USA) [76], [77]. These devices have few optodes and are primarily used to quantify point measurements of oxygenation. A wired ambulatory DOT device with 64 S-D pairs has shown to be able to track hemodynamics in muscles [78], and another 128-channel wired NIRS device has been developed for monitoring brain activity, although the configuration of this device is optimized to be fixed around human head [79]. Compared to prior wearable NIRS devices, our probe has the greatest number of source-detector pairs at 512, offering both high area coverage and high optode-density. While lower optode-density devices typically offer better tissue contact and flexibility, our rigid-flex design enables this high spatial sampling while preserving this flexibility. Also, while this device is designed for use on breast tissue, its flexibility is such that it could be extended to almost any other anatomical location that does not require extreme flexion. However, acquisition speed for other devices is generally higher, with the wired ambulatory DOT system showcasing speeds up to 250 Hz, for example.

The experiments in Section 2.3.2 and 2.3.3 validate the utility of this device. The flow phantom experiments demonstrate how the range of S-D separations and optode

positions offered allow for sensitivity to absorption contrast at a range of axial and lateral positions. Furthermore, the cuff occlusion experiment confirms that the probe can track the expected hemodynamic response to a perturbation *in vivo*.

The healthy volunteer study presented in Sections 2.4.2 and 2.4.3 demonstrates that paced breathing hemodynamics are likely quantifiable in breast tissue. The comparison between breast measurements and contralateral worn deformable phantom measurements suggests that the observed oscillations during paced breathing reflect actual physiology, although, as shown in Figure 2.7c, motion artifact at the breathing rate likely contributes to this signal as well. While the deformable phantom attempts to mimic the mechanical properties of breast tissue, probe contact with tissue and phantom may still differ, especially considering the variation in breast composition, shape, and size, and the motion artifact may be underestimated. Oscillations observed in leg measurements at the breathing rate, whose motion should not correlate with breathing-induced motion, confirm that the probe is sensitive to such hemodynamics *in vivo*. As expected, leg SAR values generally exceeded breast SAR values, which is likely in part due to the decreased motion artifact in the leg region. That said, distributions of breast SAR values overlapped with leg SAR distributions, which further supports the notion that these hemodynamics are measurable in breast tissue.

The ability to quantify the amplitudes of ΔHbO_2 and ΔHHb , and relatedly to derive $\text{SO}_{2,\text{resp}}$, offers a new slate of optical biomarkers in breast tissue that may be able to identify tumor contrast in breast cancer patients. The effects of respiratory-induced changes in peripheral blood vessels is detailed by Franceschini et al. and Wolf et al [64],

[65]. Briefly, during inspiration, a decrease in intrathoracic pressure creates a pressure gradient between extrathoracic vessels and the intrathoracic vessels and the heart. As veins are ~20 times more compliant than arteries, this pressure difference primarily results in volume changes in venous compartments, decreasing venous blood volume while increasing venous return to the heart. Franceschini et al. notes that due to the presence of vein valves, the decrease in venous return during expiration does not match the increase during inspiration, creating a respiratory pump effect that modulates central venous pressure, and, resultantly, venous blood volume, at the respiratory rate.

The $SO_{2,resp}$ parameter may be of particular interest in breast cancer treatment monitoring, for it may correlate with or be equal to the venous oxygen saturation SvO_2 . While tissue oxygen saturation, or StO_2 , has been monitored in breast tissue during NAC [25], [44], SvO_2 has yet to be quantified in breast or in breast tumors. The $SO_{2,resp}$ values calculated in breast tissue for the N=4 healthy subjects in this volunteer study are generally higher than reported values from previous noninvasive NIRS measurements of SvO_2 , with median breast values ranging from 82% to 87%. Franceschini et al. reported baseline SvO_2 values of 75-78% when probing the vastus medialis muscle (inner thigh) of a healthy adult volunteer (age not stated) [64]. Wolf et al. reported mean cerebral SvO_2 values of $73\% \pm 9\%$ across 15 neonates [65], while Kainerstorfer et al. reported mean cerebral SvO_2 values of $66\% \pm 14\%$ across 3 healthy adults (ages 25-49) [71]. Closer to our extracted values, Lynch et al. reported mean SvO_2 values of $79\% \pm 7\%$ on forehead measurements from 5 healthy volunteers (age not stated) [72]. However, there are some important differences to note between previous *in vivo* NIRS measurements of SvO_2 and

the breast measurements presented in this work. Firstly, the sample sizes are all small, and the age groups are different across studies, with some age groups unknown. Another important distinction between our study and the previous ones described is the breathing rate. The breathing rate in the neonate study was 0.5 Hz. For the vastus medialis measurement by Franceschini et al. and forehead measurements by Lynch et al., the breathing rates were 0.25 Hz and 0.18 Hz, respectively, which are close to spontaneous breathing rates. The study by Kainerstorfer et al. had subjects fix their breathing rate at 0.1 Hz. The breathing rate in our study of 0.05 Hz is the lowest rate of any of these studies. It may be possible that this slow breathing frequency is producing different physiological effects than spontaneous or near-spontaneous breathing. More exploration of the paced breathing frequency is needed to clarify this difference. Lastly, the extinction spectra source is not always reported, and the usage of different spectra across studies could lead to variation in SvO₂.

It should also be reiterated that a possible limitation, or complication, to our SO_{2,resp} measurements relates to the relative phase of the ΔHbO_2 and ΔHHb . As stated before, blood volume oscillations should produce in-phase hemodynamic changes. The spread of relative phases observed in this study may suggest there is some contribution from blood flow changes, which are known to produce out-of-phase oscillations [71]. It is also possible that phase extraction was inaccurate in some cases due to relatively low ΔHHb oscillations. Further exploration of relative phase will be a focal point of future studies in order to better understand the physiology related to these respiratory maneuvers.

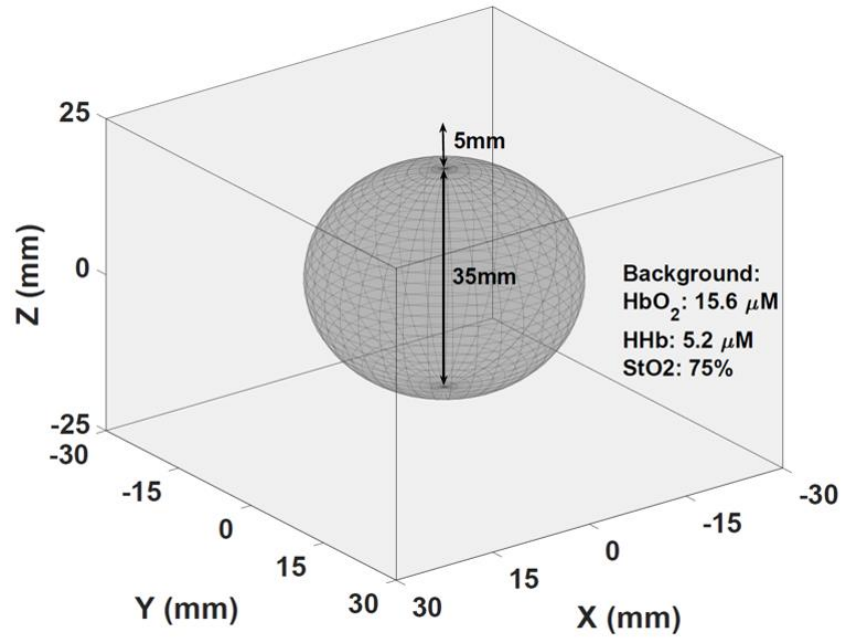
While we are not aware of other paced breathing studies aimed at human breast hemodynamics, there have recently been several studies exploring fast tumor hemodynamics in response to breath holds, occurring on the order of seconds to tens of seconds [50]–[52]. One study found that breath hold hemodynamic responses were able to predict pCR at the two-week point of NAC with strong negative predictive value (94%) and moderate positive predictive value (71%) [52]. A preclinical study of a rat breast cancer model yielded results consistent with these findings, demonstrating that changes in HbO₂ during simulated breath holds could differentiate treatment and control groups, and that optical changes preceded tumor volume changes [53]. Another clinical study demonstrated that compression-induced hemodynamics were able to differentiate responders from non-responders within the first month of chemotherapy [54].

This leads to an important limitation of this system, that being acquisition speed. With two probes being sequentially scanned at 0.2 Hz, bandwidth is greatly limited to just 0.1 Hz, preventing measurements at a wider range of frequencies, including those closer to spontaneous breathing. While subjects were able to perform the breathing protocol without difficulties, 0.05 Hz may be difficult for other subjects, for only a small sample size was measured here. The quantification of paced breathing hemodynamic metrics in breast tissue at 0.05 Hz still is significant, but more information about the underlying physiology, and perhaps greater prognostic potential, could be achieved with measurements at different breathing frequencies. Additionally, being a CW device, analysis is limited to relative quantification of optical properties and chromophore concentrations. Therefore, assumptions about initial optical properties of breast (and

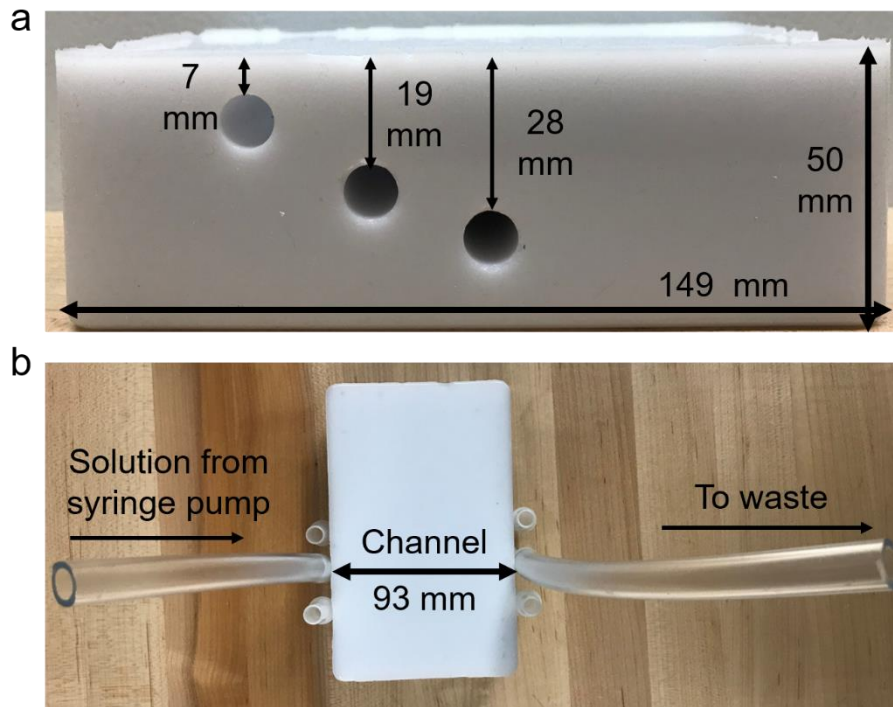
other various anatomical regions measured, such as leg and forearm) had to be made based on literature values. With respect to subject population of this study, the number and age range of subjects were both small, limiting conclusions that can be made about a broad population of healthy women. It is important to note that breast location and breast size may impact the quantification of these hemodynamic parameters. While these factors were not explored in this initial study, we plan to assess them going forward in a larger subject population. Also, as mentioned in Section 2.4.3, oscillations in ΔHHb may be below the noise floor of the probe in some instances. This could be a product of poor tissue contact for some optodes, which may increase noise and motion artifact. Alternative adhesives as well as more flexible silicone probe housings will be explored as methods of optimizing tissue contact.

We have demonstrated the utility of a custom high optode-density wearable diffuse optical probe through performance characterization, validation, and breast measurements. Optodes with S-D separations ranging from 22 mm to 50 mm had high SNR, high precision, and low drift, and validation experiments with flow phantoms and a cuff occlusion confirmed the ability to quantify absorption contrast, both spatially or temporally. Breast measurements with a worn phantom suggested that while motion artifact contributed to the measured signal (and may be underestimated), optical signal is reflective of actual hemodynamics, demonstrating the feasibility of quantifying breathing hemodynamics such as ΔHbO_2 and ΔHHb amplitudes as well as $\text{SO}_{2,\text{resp}}$ in breast tissue.

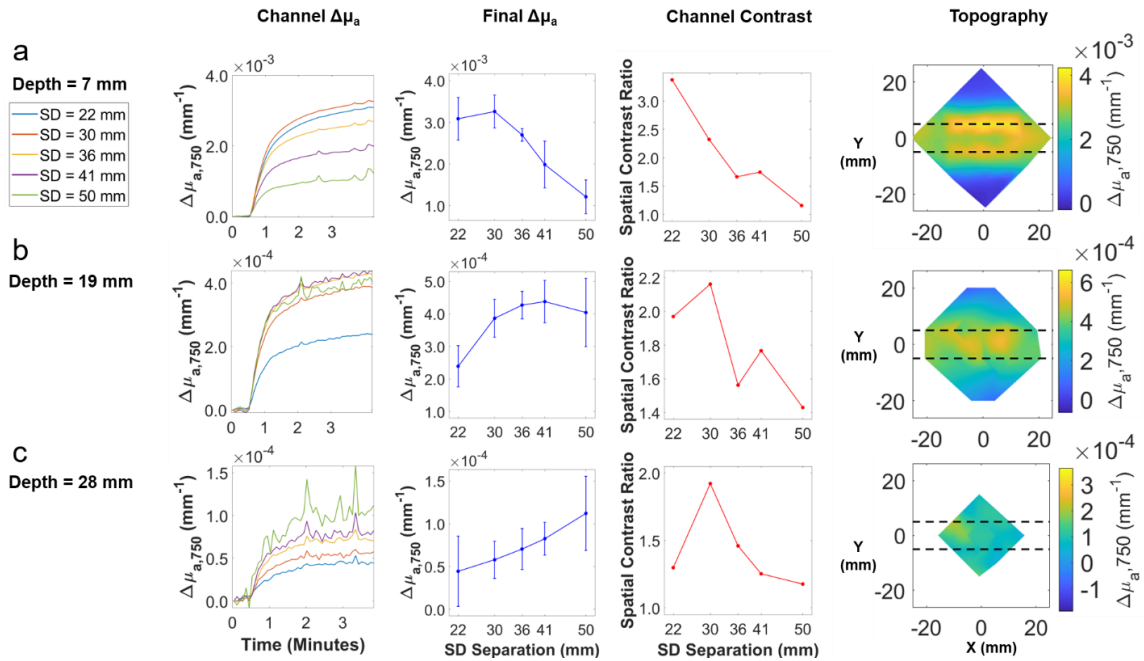
2.6 Supplementary Information



Supplementary Figure S2.1. Simulation geometry utilized for optode configuration comparisons. The inclusion mimics a 35 mm diameter breast tumor embedded in healthy breast tissue.



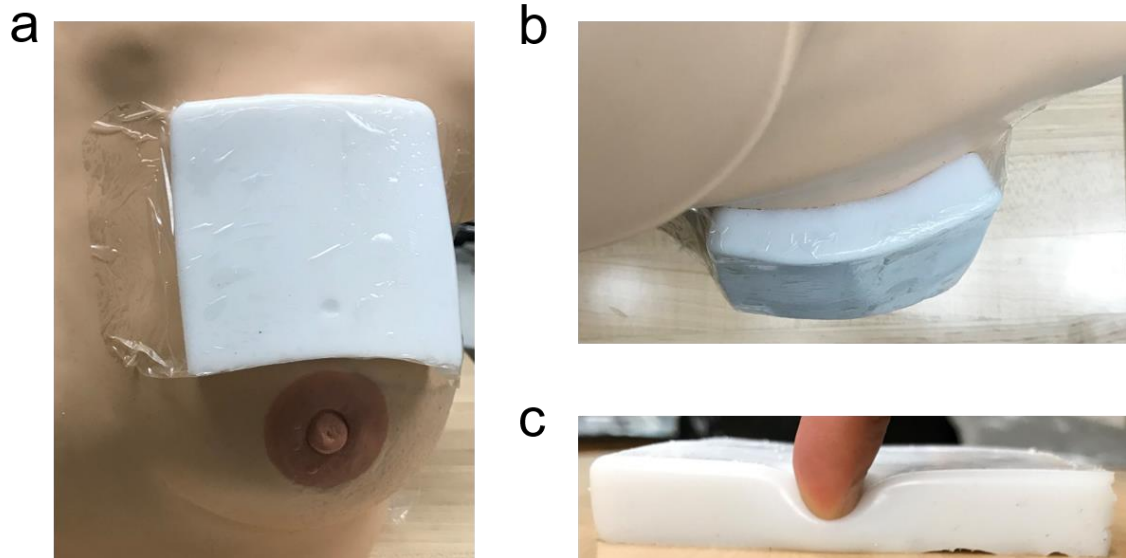
Supplementary Figure S2.2 a) Side view of the silicone channel phantom with three channels at varying depths. The nominal depth refers to the distance between the surface of the phantom and the upper edge of the channel. b) Top view of the silicone phantom with right-angle tubing adapters connected to each channel. These enable the channels to be pre-filled with the first solution. Tubing is connected to the adapters for one of the three channels, showing how the syringe pump can dispense the second solution into the channel. Not shown here are the syringe pump, syringe, and waste container.



Supplementary Figure S2.3 Results from flow phantom experiments for channels whose upper edge were (a) 7 mm, (b) 19 mm, and (c) 28 mm below the background phantom surface. Only 750 nm data is shown. The first column, labeled “Channel $\Delta\mu_a$ ”, depicts the mean $\Delta\mu_a$ values as a function of time across all S-D pairs that probe the width of the channel. Flow began after ~ 0.5 minutes. For each S-D separation (going from 22 mm to 50 mm), the sample sizes (number of S-D pairs within channel) were as follows: $n=28, 12, 20, 20, 18$. The second column, labeled “Final $\Delta\mu_a$ ”, shows the mean and standard deviation of $\Delta\mu_a$ values at the final time point of the flow experiment. The third column, labeled “Channel Contrast”, depicts spatial contrast as a function of S-D separation. The final column shows a topographic reconstruction of the final $\Delta\mu_a$ values (in x-y space) for each channel depth, each shown for the S-D separation that corresponded to the highest final $\Delta\mu_a$. For (a), this was 22 mm, for (b) this was 41 mm, and for (c), this was 50 mm. The colorbar represents $\Delta\mu_a$ in units of mm^{-1} , and the horizontal dashed lines indicate the true boundaries of the channel.

Supplementary Table S2.1 Depth penetration estimates using photon hitting density (PHD) from simulations

S-D Separation	22 mm		30 mm		36 mm		41 mm		50 mm	
	750 nm	850 nm	750 nm	850 nm	750 nm	850 nm	750 nm	850 nm	750 nm	850 nm
Depth at PHD Peak (mm)	4.5	4.3	6.1	5.8	7.2	6.9	8.1	7.7	9.5	9.1
Depth at 90% Peak (mm)	6.3	6	8.3	8	9.7	9.3	10.8	10.3	12.5	12
Depth at 50% Peak (mm)	9.8	9.4	12.5	12	14.3	13.8	15.7	15.1	19	17.4
Depth at 10% Peak (mm)	16	15.5	19.7	19	22.1	21.3	24	23.1	27.1	26.1



Supplementary Figure S2.4 Depictions of the deformable phantom described in Section 4.2. (a) View of phantom adhered to bust model. b) Top-view bust model/phantom shown in (a). c) Demonstration of the deformability of the phantom, with a finger making an indent into the phantom by pressing.

Supplementary Video S1:

This video displays 10 panels in a 2 x 5 format. The upper row shows topographic reconstructions of $\Delta\mu$ over time for the 750 nm S-D pairs at the five S-D separations for the 7 mm depth flow phantom experiment. From left to the right, the S-D separations are 22 mm, 30 mm, 36 mm, 41 mm, and 50 mm. The bottom row shows the topographic reconstructions of $\Delta\mu$ for the 850 nm S-D pairs. The colorbar in each row applies to all S-D separations for that row.

Supplementary Video S2:

The format of this video is the same as in Supplementary Video 1, except this video displays topographic reconstructions for the 19 mm depth flow phantom experiment.

Supplementary Video S3:

The format of this video is the same as in Supplementary Video 1, except this video displays topographic reconstructions for the 28 mm depth flow phantom experiment.

Supplementary Video S4:

This video displays 10 panels in a 2 x 5 format. The upper row shows topographic reconstructions of ΔHbO_2 over time at the five S-D separations during the cuff occlusion experiment. From left to the right, the S-D separations are 22 mm, 30 mm, 36 mm, 41 mm, and 50 mm. The bottom row shows the topographic reconstructions of ΔHHb . The colorbar in each row applies to all S-D separations for that row. The time is shown above all panels in addition to the phase of the experiment (baseline, perturbation, recovery).

CHAPTER THREE: INITIAL CLINICAL FEASIBILITY STUDY

3.1 Introduction

With the NIR wearable probe's ability to quantify paced breathing hemodynamics in healthy breast tissue validated, the next goal was to assess clinical feasibility and determine if the probe was sensitive to tumor contrast and neoadjuvant chemotherapy (NAC) response. In addition to exploring the sensitivity of paced breathing-related metrics, traditional diffuse optical imaging (DOI) parameters, namely absolute concentrations of oxy- and deoxy-hemoglobin (HbO₂ and HHb, respectively), total hemoglobin (THb), and tissue oxygen saturation (StO₂) would be quantified as well through off-phantom calibration. In order to quantify repeatability and expected variation across breasts of both paced breathing and traditional DOI biomarkers, which would contextualize any observed clinical trends, another group of N=4 healthy volunteers first performed move and replace measurements. Then, N=3 breast cancer patients were measured in the clinic longitudinally during their NAC regimens. In part due to the COVID-19 pandemic, patient accrual was limited, resulting in the low number of subjects in this initial study. However, it would still be useful to determine if any promising results were observed in this group, in addition to testing the practicality of implementing this probe and its related protocols in the clinic.

3.2 Healthy volunteer repeatability and variation study

In order to assess repeatability and contralateral breast variation for both traditional and paced breathing metrics, N=4 healthy volunteers had probes worn on both breasts while performing three trials of the paced breathing protocol described in Chapter 2. Paced

breathing metrics were quantified in the same manner described in Chapter 2, and, additionally, StO_2 and absolute concentrations of HbO_2 , HHb , and THb were measured using off-phantom calibration. Here, the paced breathing metrics, namely HbO_2 amplitude, HHb amplitude, and oxygen saturation at the respiratory rate, are referred to as $\text{HbO}_{2,\text{PB}}$, HHb_{PB} , and SrO_2 , respectively. Absolute concentrations of HbO_2 and HHb are referred to as $\text{HbO}_{2,\text{abs}}$ and HHb_{abs} , respectively. Additional composite metrics combining traditional and paced breathing biomarkers were also explored.

The process for computing the absolute concentrations and their related composite metrics using off-phantom calibration is briefly described here. A calibration phantom with known optical properties was measured with the probes that would be worn by the subjects. These known optical properties were mapped to theoretical diffuse reflectance (R_d) values for each source-detector (S-D) pair using the P1 approximation to the radiative transport equation (RTE). With these theoretical R_d values and corresponding measured voltages from the phantom, a linear mapping of measured voltage to R_d was determined for each individual S-D pair, which could then be applied to the subsequent subject breast measurements to compute R_d values during their baseline measurements (prior to paced breathing). Next, an assumption about tissue scattering was made for breast tissue, and the P1 approximation to the RTE was again used, this time to compute the absolute absorption coefficient μ_a from the R_d and an assumed μ'_s . Pairs of μ_a values at 750 nm and 850 nm were then fit to Beer's law (as described in Chapter 2) to extract $\text{HbO}_{2,\text{abs}}$ and HHb_{abs} , and the composite metrics THb and StO_2 were defined as $\text{THb} =$

$\text{HbO}_{2,\text{abs}} + \text{HHb}_{\text{abs}}$ and $\text{StO}_2 = \text{HbO}_{2,\text{abs}}/(\text{HbO}_{2,\text{abs}} + \text{HHb}_{\text{abs}})$, respectively. Literature values for pre-menopausal healthy breast tissue were used to make μ'_s assumptions [91].

Figure 3.1 shows results for the StO_2 and SrO_2 metrics from the healthy volunteer measurements. As seen in Figure 3.1a, the coefficient of variation (CV) in StO_2 across the three repeated trials per subject was $<2.5\%$ for all subjects, with a mean value of 1.4% . For SrO_2 (Figure 3.1b), the CV was $<7.3\%$ for all subjects, with a mean value of 4.6% . This increase in CV for the paced breathing metric is likely explained by the increased variability of the manner in which subjects perform the paced breathing. In other words, the breathing protocol introduces more variation to the measurement in comparison to the static, single time point-derived traditional metric. Mean CV values for $\text{HbO}_{2,\text{abs}}$ and HHb_{abs} were 3.4% and 3.6% , respectively. Mean CV values for $\text{HbO}_{2,\text{PB}}$ and HHb_{PB} were 28% and 30% , but these were heavily influenced by large values from a single trial for a single subject. Removing that trial, mean CV values were 15% and 17% , respectively. This still suggests that the breathing protocol and its related metrics have much higher variability than the traditional DOI metrics individually, but that this variability is reduced for the composite metric SrO_2 .

Figures 3.1c and 3.1d depict the variation in StO_2 and SrO_2 , respectively, across contralateral breasts within the same subjects, represented as a left breast to right breast ratio for a given metric. These bar plots suggest that for all subjects, there is little variation across breasts within the same subject for these two metrics. The mean \pm standard deviation across all subjects was 0.99 ± 0.03 and 1.04 ± 0.06 for StO_2 and SrO_2 , respectively. For $\text{HbO}_{2,\text{abs}}$ and HHb_{abs} , the ratios were 0.93 ± 0.08 and 1.00 ± 0.05 , and

for $\text{HbO}_{2,\text{PB}}$ and HHB_{PB} , the ratios were 0.74 ± 0.28 and 0.63 ± 0.24 . Removing the same trial mentioned previously from this dataset, however, results in $\text{HbO}_{2,\text{PB}}$ and HHB_{PB} ratios of 0.79 ± 0.22 and 0.67 ± 0.20 , respectively. The large standard deviations for $\text{HbO}_{2,\text{PB}}$ and HHB_{PB} were expected based on the larger CV values for these metrics, but it may be of interest to note that the mean ratio values were well below 1. This indicates that there may be some inherent variation across breasts for these paced breathing related metrics, although more subjects would be needed to confirm the statistical significance of this finding.

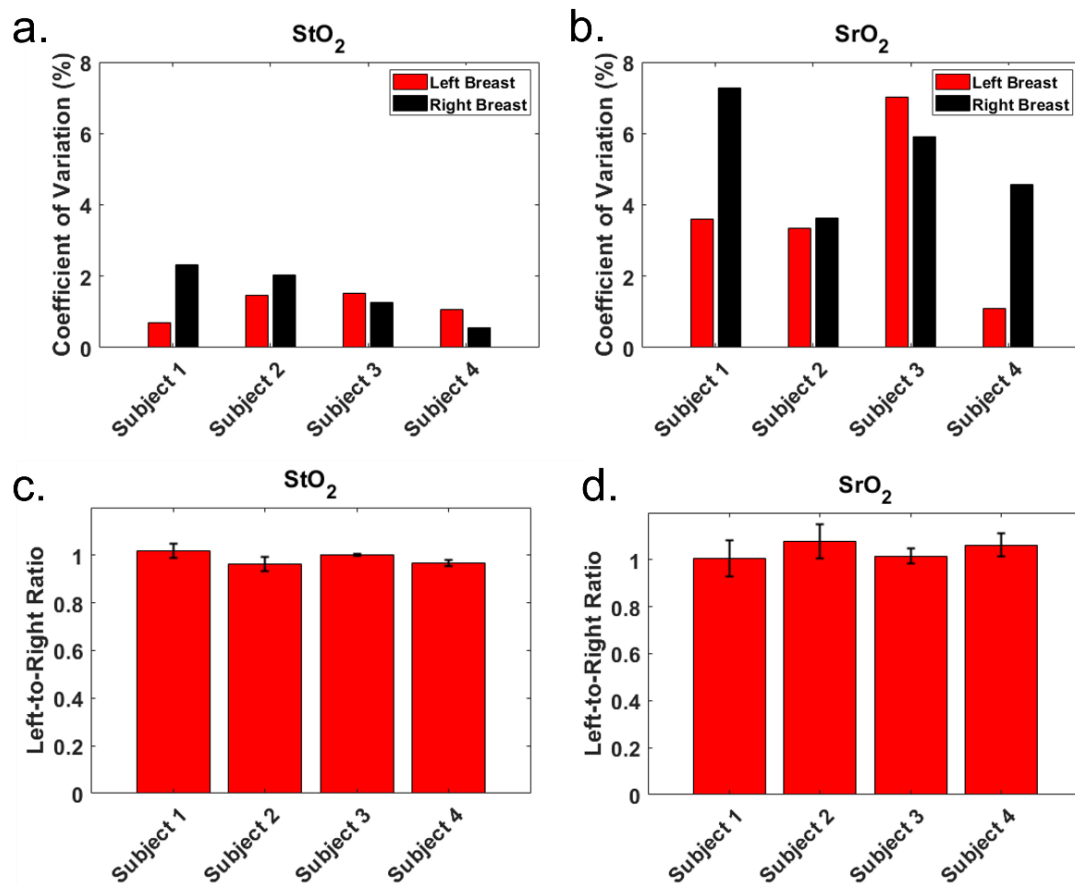


Figure 3.1. Coefficients of variation by subject for (a) StO_2 and (b) SrO_2 , and left breast to right breast ratio of these same metrics (c and d).

3.3 Longitudinal monitoring of NAC patients in the clinic

The clinical feasibility study involved measuring N=3 breast cancer patients at four different time points during their NAC regimens – at baseline (prior to chemotherapy), on day 2 (~24 hours after first chemotherapy infusion), at a midpoint (defined below), and pre-surgery (between the final chemotherapy infusion and surgery). The midpoint measurement was intended to be the exact midpoint in time of the NAC regimen, but for Subject 2, a scheduling error resulted in the midpoint measurement occurring ~25% into the NAC regimen's duration. All three subjects were measured at Boston Medical Center through an approved IRB protocol. Differences in measured metrics between pathologic complete responders (pCR, meaning no residual cancer at the time of surgery) and non-pCR patients were then explored. Patient characteristics are presented in Table 3.1. A fourth patient was measured as well, but her surgery has yet to be performed and thus her treatment outcome is not known at this time.

The spatial probe registration process at each time point is described here. During the baseline measurement visit, each subject changed into a hospital gown and was seated upright in a chair. A clinical research coordinator (CRC) then asked the subject to locate the approximate tumor location, and subsequently palpated the breast to confirm the location. The CRC then gently applied a blank sheet of transparent paper onto the tumor-bearing breast and marked the nipple, areola, and tumor locations on the paper. Other landmark features and the orientation of the paper were also labeled for ease of re-application. The transparent paper was then given to the probe operator, who traced a probe outline over the desired measurement location, centering the tumor within the

Table 3.1. Patient characteristics

Subject	1	2	3
Age	62	52	44
Menopausal status	Post	Post	Pre
Tumor location	Left breast, upper lateral quadrant	Right breast, upper medial quadrant	Left breast, upper lateral quadrant
Tumor size	~5 cm in diameter	~2 cm in diameter	~5 cm in diameter
PR (+/-)	+	-	-
ER (+/-)	-	+	-
HER2 (+/-)	+	-	+
Treatment regimen	6 x [carboplatin, docetaxel, pertuzumab, trastuzumab]	12 x [pembrolizumab, paclitaxel, carboplatin] 4 x [pembrolizumab, doxorubicin, cyclophosphamide]	4 x [pertuzumab, trastuzumab, paclitaxel]
Pathologic response	pCR	non-pCR	non-pCR

probe area. A surgical marker was then used to trace this same probe outline on the reverse side of the transparent paper, which was then realigned on the tumor-bearing breast and pressed to leave an imprint of the surgical marker where the probe should be worn. Next, the CRC adhered a probe to this location using medical grade IV tape. Another piece of transparent paper was then applied to the healthy contralateral breast in the same manner, and the nipple, areola, and landmark features were again labeled. A mirrored probe location was traced on this paper and pressed onto the unaffected breast, and a second probe was adhered to this site, providing a potential control for comparison

with the tumor site. These transparency sheets were stored, and at subsequent time points, they were realigned on the subject's breasts so that probes could be adhered at the same locations over time.

At each time point, subjects performed three trials of the paced breathing protocol described in Chapter 2, and a phantom calibration measurement was also performed. Paced breathing metrics were then computed using the same processing pipeline described in Chapter 2, and the traditional absolute metrics were computed using the off-phantom calibration described in the healthy volunteer repeatability/variation study. For Subjects 1 and 2 (age 62 and 52), post-menopausal breast tissue scattering values from literature were assumed, while for Subject 3 (age 44), pre-menopausal breast tissue scattering was assumed [91]. Subject 1 exhibited pCR, while Subjects 2 and 3 were non-pCR.

With only three subjects, no statistically significant conclusions could be drawn from this initial feasibility study, but individual and longitudinal time point data were explored for possibly promising sources of tumor contrast and trends. Figure 3.2a and 3.2b shows spatial maps of THb on the tumor-bearing and contralateral healthy breasts of Subject 3 at baseline. These maps illustrate an elevated level of THb in the tumor-bearing breast, which is consistent with previous findings, likely owed to tumor angiogenesis [25], [47]. Due to elevated interstitial fluid pressure in tumors, it was suspected that negative contrast might be observed in some of the paced breathing related metrics, as vascular oscillations at the respiratory rate might be dampened by the elevated surrounding pressure. However, an accumulation of vessels may still result in positive

contrast, even with reduced oscillation amplitude on a per vessel basis, and thus an additional composite metric was examined that normalized $\text{HbO}_{2,\text{PB}}$ by dividing by $\text{HbO}_{2,\text{abs}}$. The spatial maps of this metric for Subject 2 at baseline are shown in Figures 3.2c and 3.2d, which indeed show a reduced value in this normalized metric in the tumor-bearing breast. These are just individual instances of observed contrast that would need to be validated with many more subjects, but the goal of this analysis was to simply locate any potential sources of contrast that stood out, which is what is highlighted in this figure.

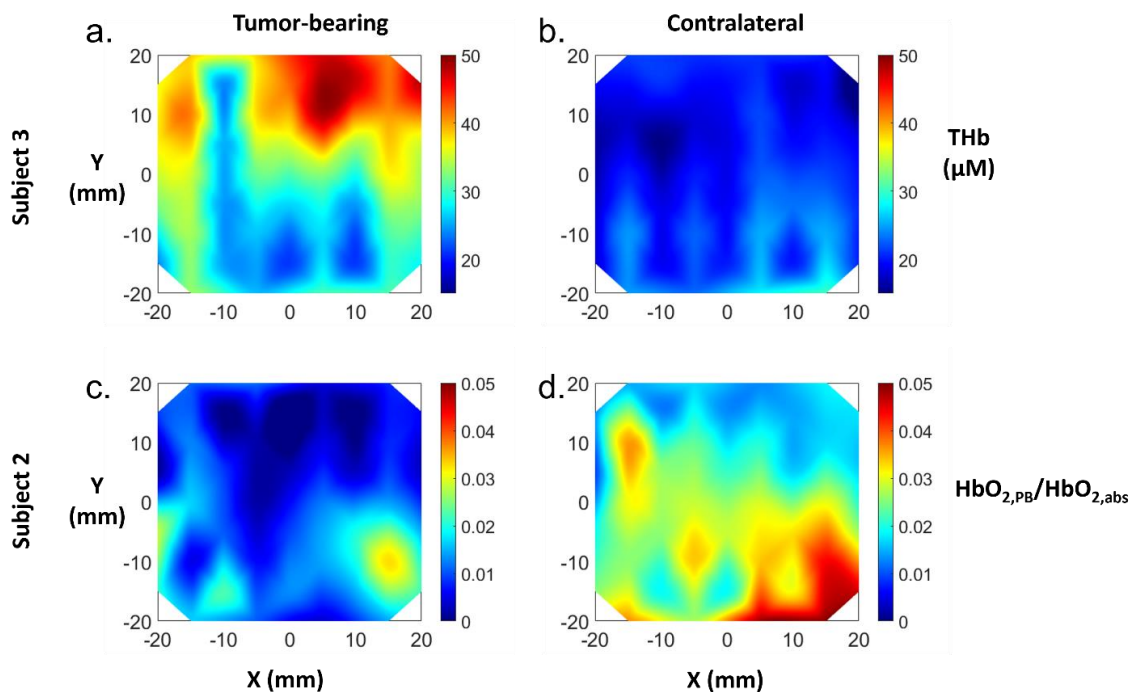


Figure 3.2. a) Spatial map of THb at baseline for Subject 3 on the tumor-bearing breast. b) Same map as (a), but for the contralateral unaffected breast. c) Spatial map of $\text{HbO}_{2,\text{PB}}/\text{HbO}_{2,\text{abs}}$ at baseline for Subject 2 on the tumor-bearing breast. d) Same map as (c), but for the contralateral unaffected breast.

Figure 3.3 depicts some of the longitudinal trends for metrics that showed separation between pCR and non-pCR subjects at the midpoint of surgery, normalized to baseline values. Figure 3.3a reveals a 54% drop in StO_2 from baseline in the pCR patient

(Subject 1), compared to a 9% increase and 8% decrease for the non-pCR Subjects 2 and 3, respectively. Interestingly, this large drop is nearly mitigated at the time of surgery for Subject 1. One of the paced breathing related metrics, SrO_2 , follows a similar trend to StO_2 , with a 20% decrease at midpoint for the pCR patient, compared to increases of 7% and 6% for the non-pCR patients (Figure 3.3b). Like StO_2 , this value also returns to near-baseline by the time of surgery. Finally, the composite metric $HbO_{2,PB}/HbO_{2,abs}$ is shown in Figure 3.3c. The pCR patient experienced a roughly 5-fold increase in this metric, or more specifically a 415% increase at midpoint, which was maintained at a 385% increase at the pre-surgery time point. Subjects 2 and 3, on the other hand, experienced increase of at most 50% in this metric.

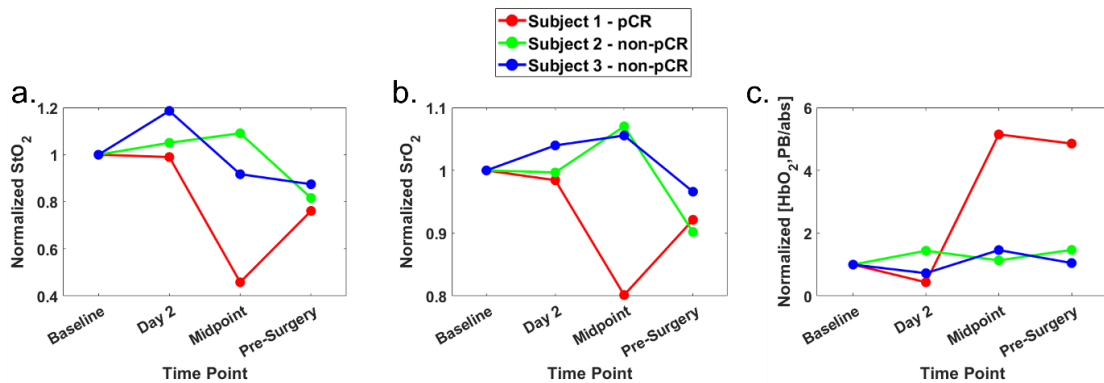


Figure 3.3. Longitudinal trends in (a) StO_2 , (b) SrO_2 , and (c) $HbO_{2,PB}/HbO_{2,abs}$, normalized to baseline levels.

3.4 Discussion

While low patient accrual limits the statistical analysis and conclusions that can be drawn from this feasibility study, it is worth noting that isolated incidents of tumor contrast and trends separating pCR from non-pCR patients were observed that could be validated in a larger subsequent study. It is also worth acknowledging that this wearable NIR probe and

the associated paced breathing protocol were successfully implemented in the clinic without major technical setbacks or challenges, suggesting that such a larger study would be possible.

The observed trends in both StO_2 and SrO_2 for Subject 1 can possibly be explained by hypoxia and necrosis in the tumor as the effective treatment kills tumor cells and vasculature. The rebound in these two metrics at the pre-surgery time point may indicate that the necrotic tissue has been cleared and replaced with healthy breast tissue that has regular oxygen supply and metabolism. This trend has not been observed in prior diffuse optics studies. In previous studies, low StO_2 at baseline and within the first 10 days of treatment have been correlated with a poor response to treatment, while high StO_2 correlated with pCR outcomes [48], [104]. In our study, minimal changes in StO_2 and SrO_2 at the earliest (day 2) time point post-treatment were observed, so the large decrease by the midpoint may still be consistent with these previous early time point findings.

The trend in $HbO_{2,PB}/HbO_{2,abs}$ has not been explored previously in breast cancer monitoring, and its large and maintained increase in the pCR patient may be explained by multiple simultaneous phenomena. As tumor cell death takes place, tumor vessels are killed and it is expected that absolute hemoglobin levels will decrease. As $HbO_{2,abs}$ is in the denominator of this metric, this would result in an increase in this metric as the patient responds positively to treatment. However, the inverse of $HbO_{2,abs}$ alone only showed a 3-fold increase during NAC, not the 5-fold increase observed with the composite metric. Therefore, it is believed that the simultaneous lowering of interstitial fluid pressure in the dying tumor results in expanded respiratory-induced vessel

oscillations, increasing the numerator of this metric, which is the $\text{HbO}_{2,\text{PB}}$ amplitude. The overall decrease in hemoglobin combined with the normalization of the tissue interstitial fluid pressure may result in amplified contrast between responding and non-responding patients.

Of course, this has only been one instance of this observed contrast and, as stated previously, this requires much more validation. It is also important to note that, while the trends shown in Figure 3.3 were highlighted due to the separation of the pCR patient from the two non-pCR patients, other trends that have been observed in previous breast cancer DOI studies may have been replicated had there been more subjects. For example, it has been shown that THb generally decreases in responders to treatment, which was the case for Subject 1. However, too much variability in this metric was observed in the two non-responders, rendering separation of the treatment groups impossible with this sample size, which is why this trend is not included in Figure 3.3.

Despite the limitations of this study, the practicality of using a wearable optical probe for breast cancer monitoring in the clinic has been demonstrated, and some metrics may offer promise in larger study. However, it must be considered that the paced breathing protocol itself may have too much associated variability, as shown in the healthy volunteer study from this chapter. Furthermore, not enough patients were measured to determine if the breathing process is achievable across a broad population, and the time burden associated with it may limit the clinical adoption. While a larger scale study with this wearable probe would certainly have value, as it could enable more

frequent treatment response monitoring, it may be preferable to focus exclusively on the traditional DOI biomarkers for these reasons.

**CHAPTER FOUR: A SHORTWAVE INFRARED DIFFUSE OPTICAL
WEARABLE PROBE FOR QUANTIFICATION OF WATER AND LIPID
CONTENT USING DEEP LEARNING**

Significance: The shortwave infrared (SWIR, approximately 900 – 2,000 nm) holds promise for label-free measurements of water and lipid content in thick tissue, with potential applications including the monitoring of hydration, volume status, edema, body composition, weight loss, and cancer. There are currently few point-of-care or wearable devices available that exploit the SWIR wavelength range, limiting clinical and at-home translation of this technology.

Aim: To design and fabricate a diffuse optical wearable SWIR probe for water and lipid quantification in tissue.

Approach: Simulations were first performed to confirm the theoretical advantage of SWIR wavelengths over near infrared (NIR). The probe was then fabricated, consisting of LEDs at three wavelengths (980, 1200, 1300 nm) and four source-detector (S-D) separations (7, 10, 13, 16 mm). In vitro validation was then performed on emulsion phantoms containing varying concentrations of water, lipid, and deuterium oxide (D₂O). A deep neural network (DNN) was developed as the inverse model for quantity estimation.

Results: Simulations indicated that SWIR wavelengths could reduce theoretical water and lipid extraction errors from ~6% to ~1% when compared to NIR wavelengths. The SWIR probe had good SNR (>32 dB up to 10 mm S-D) and low drift (<1.1% up to 10 mm S-D). Quantification error in emulsion phantoms was $2.1 \pm 1.1\%$ for water and $-1.2 \pm$

1.5% for lipid. Water estimation during a D₂O dilution experiment had an error of $3.1 \pm 3.7\%$.

Conclusions: This diffuse optical SWIR probe was able to quantify water and lipid content *in vitro* with good accuracy, opening the door to human investigations.

This work presented in Chapter 4 is under review by the Journal of Biomedical Optics in 2023 with the following authors and corresponding institutions:

Samuel S. Spink^a, Anahita Pilvar^b, Lina Lin Wei^a, Jodee Frias^a, Kylee Anders^a, Sabrina T. Franco^a, Olivia Claire Rose^a, Megan Freeman^a, Grace Bag^a, Huiru Huang^a, Darren Roblyer^{a,b}

^a Boston University, Dept. of Biomedical Engineering, Boston, MA, 02215, USA

^b Boston University, Dept. of Electrical and Computer Engineering, Boston, MA, 02215, USA

4.1 Introduction

The near infrared (NIR, ~700-1000 nm) wavelength band has dominated diffuse optical imaging and spectroscopy in tissue for decades. While often utilized to quantify hemoglobin quantifications, NIR technologies have also been used to measure water and lipid *in vivo*, *ex vivo*, and *in vitro*, typically using wavelengths in the 900-1000 nm range [25], [28], [105]–[109]. The accurate quantification of tissue water and lipid is of interest as this capability could enable a wide range of clinical, point-of-care, and consumer applications including volume status monitoring for end-stage kidney disease and heart

failure patients, tissue hydration monitoring for athletes, body composition during weight loss, cancer treatment monitoring, and others [110].

The shortwave infrared (SWIR, ~900-2,000 nm) wavelength band is currently being explored as an alternative to the NIR due in part to the recent improvements in the availability and performance characteristics of SWIR-active detectors. Potential advantages of the SWIR wavelength band include relatively low tissue scattering [111] which has been utilized for deep tissue fluorescence microscopy with applications including the imaging of cancer biomarkers, vascular disorders, liver disease, and bone structure [112]–[115]. Water and lipid also gain dominance as absorbing chromophores in the SWIR, potentially allowing for improved quantification of these species. Prior work employing SWIR spectroscopy for water and lipid quantification includes the use of frequency-domain (FD) measurements for absolute absorption and scattering concentrations, as well as hyperspectral continuous wave (CW) measurements employing spectral constraints [81], [109]. Our prior work has demonstrated water and lipid quantification using a technique called hyperspectral SWIR spatial frequency domain imaging (SFDI). While these prior investigations show promise, clinical and at-home translation in this space remains limited in part due to the complexity of current measurement techniques, which may require bulky spectrometers, custom electronics, and expensive scientific grade detectors [82], [116].

In this work, we present a simple LED-based wearable multi-distance CW SWIR probe for the quantification of water and lipid content in tissue. We first detail the design considerations, including a comparison of chromophore recovery performance between

NIR and SWIR wavelengths in simulation. We then describe the physical layout of the probe, its control system, and its performance metrics. Finally, we validate its ability to quantify water and lipid *in vitro* through two different optical phantom experiments involving water and lipid emulsions.

4.2 Comparison of SWIR and NIR in simulation

4.2.1 Wavelength and source-detector separation selection for simulation

Figure 4.1 shows representative absorption spectra of endogenous chromophores in tissue to provide a visual comparison of the NIR and SWIR wavelength bands. Absorption spectra were computed using published extinction spectra [85], [117], [118]. Tissue concentrations of water, HbO₂, and HHb are average values reported for healthy breast

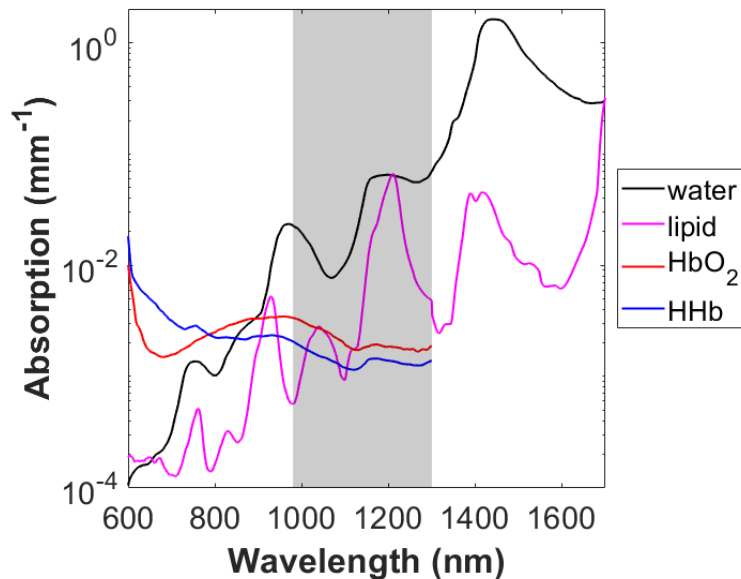


Figure 4.1. Absorption of endogenous chromophores in healthy breast tissue from 600-1700 nm (for water and lipid) and 600-1300 nm (for HbO₂ and HHb). Tissue concentrations for this example are as follows: water = 51.5%, lipid = 40%, HbO₂ = 11.3 μ M, HHb = 5.3 μ M. The shaded region (980 nm – 1300 nm) refers to desired SWIR wavelength region for our probe design.

tissue, with lipid estimated at 40% by volume [119]. As seen in this figure, water absorption overtakes that of hemoglobin past ~900 nm, while lipid exceeds hemoglobin absorption past ~1100 nm for this tissue type. Water absorption becomes very high past 1400 nm, limiting imaging penetration depth and signal levels. A SWIR window of 980 nm – 1300 nm (shaded region) in Figure 4.1) was chosen for the probe illumination based on these considerations. Discrete wavelengths at 980, 1200, and 1300 nm were then chosen based on LED availability. Water absorption is relatively high at all three of these wavelengths, while lipid absorption has a peak near 1200 nm. For the NIR, 900, 930, and 970 nm were chosen based on spectral features previously mentioned and LED availability. Four source-detector (S-D) separations (7, 10, 13, and 16 mm) were included in the simulations. In total, this resulted in 12 unique wavelength/separation pairs for the SWIR and NIR.

4.2.2 Simulation workflow

Simulations were performed using both Matlab and Python, and the workflow is described here and summarized in Figure 4.2a. For a single simulation, water, lipid, and scattering properties were randomized for the simulated “sample”. Water and lipid values were picked from uniform distributions between 0 and 100 % and always summed to 100 %. A power law (Equation 4.1) described the scattering relationship with wavelength, with scattering amplitude (A) and slope (b) as the randomized properties:

$$(4.1) \quad \mu'_s(\lambda) = A * \left(\frac{\lambda}{980 \text{ nm}} \right)^{-b}$$

Possible amplitude values were defined as a uniform distribution from $0.2 - 10 \text{ mm}^{-1}$ (referenced to 980 nm). Scattering slope values were defined as a normal distribution with $\mu = 1.29$, $\sigma = 0.52$, which are typical slope values for soft tissue [120]. Next, the absorption coefficient (μ_a) and reduced scattering coefficient (μ'_s) were computed for each of the three SWIR and NIR wavelengths. Beer's Law was used to compute μ_a (using the same extinction spectra from Section 4.2.1), and Equation 4.1 was used to compute μ'_s . A pre-generated look-up table (LUT) of Monte Carlo-derived diffuse reflectance (R_d) values then mapped optical property pairs to R_d values for each of the 12 unique wavelength/separation pairs, for both the SWIR and NIR groups (Monte Carlo simulations described in more detail in the following section). Zero-mean Gaussian noise was then added to the R_d values, with $\sigma = 5\%$. These noise-added R_d values were then input to an inverse model to recover water and lipid estimates. A fully connected deep neural network (DNN) was used as the inverse model. This process was repeated 25,000 times, resulting in 25,000 sets of recovered water and lipid values for both the SWIR and NIR groups. These recovered values were compared to the ground truth values in order to compute the mean and standard deviation of extraction errors.

4.2.3 Forward and inverse models: Monte Carlo and deep neural network

White Monte Carlo simulations were run and the results were used to map optical property pairs to surface diffuse reflectance. Simulations were run in Matlab using Monte Carlo eXtreme (MCX) [121]. The sample geometry was defined as a slab with dimensions of $6 \times 6 \times 10 \text{ cm}$, approximating a semi-infinite medium. Optical properties

were homogenous, with $\mu_a = 0 \text{ mm}^{-1}$ and μ'_s ranging from $0.2 - 10 \text{ mm}^{-1}$. Detectors were placed 7, 10, 13, and 16 mm and a steady-state illumination source fiber was used. Collected photons for each μ'_s value were then scaled for a range of absorption values using the Beer-Lambert law, with μ_a ranging from $0.001 - 0.2 \text{ mm}^{-1}$. Anisotropy factor g and index of refraction n were set to 0.7 and 1.435, respectively, which are values for lipid-water emulsions adapted from Flock et al. and Aernouts et al [122], [123]. After the Monte Carlo simulations were completed, the μ_a , μ'_s , and resultant R_d values at each S-D separation were saved in a LUT.

The DNN was implemented in Python using the Keras library. The architecture and training parameters are summarized in Figure 4.2b, and are briefly described here. The DNN consists of an input layer with 12 nodes (R_d each wavelength/separation pair), three hidden layers, each with 20 nodes, and an output layer with two nodes (recovered water and lipid). The rectified linear unit (ReLU) was selected as the activation function for hidden layer nodes, and a linear function was the activation function for the output layer. The Adam optimizer was the training algorithm with a learning rate = 0.001. The loss function (or error function) was the mean squared error (MSE) of water and lipid. For training data, 75,000 sets of water, lipid, and R_d values (generated using the same Monte Carlo LUTs described previously) were constructed in Matlab and imported into Python, using the same randomization process and parameters described for the 25,000 test datasets in Section 4.2.2. These parameters are also reported in Supplementary Table S4.1. The R_d inputs were log-normalized prior to training. The spectral constraints described in Section 4.2.2, namely 1) absorption limited to a linear sum of water and lipid

contributions, and 2) the wavelength dependence of scattering defined by a power law, provided important constraints during training which helped to reduce the solution space. Two DNNs were trained, one for SWIR and one for NIR. Initially, automatic stopping was implemented during training, stopping when the mean loss over the previous 200 epochs was no longer decreasing. This occurred after ~ 2000 epochs for both SWIR and NIR. To be cautious, the final DNNs used for comparison were trained with 3000 epochs. All subsequent DNNs in this study (after the SWIR vs. NIR comparison), however, were trained with 2000 epochs.

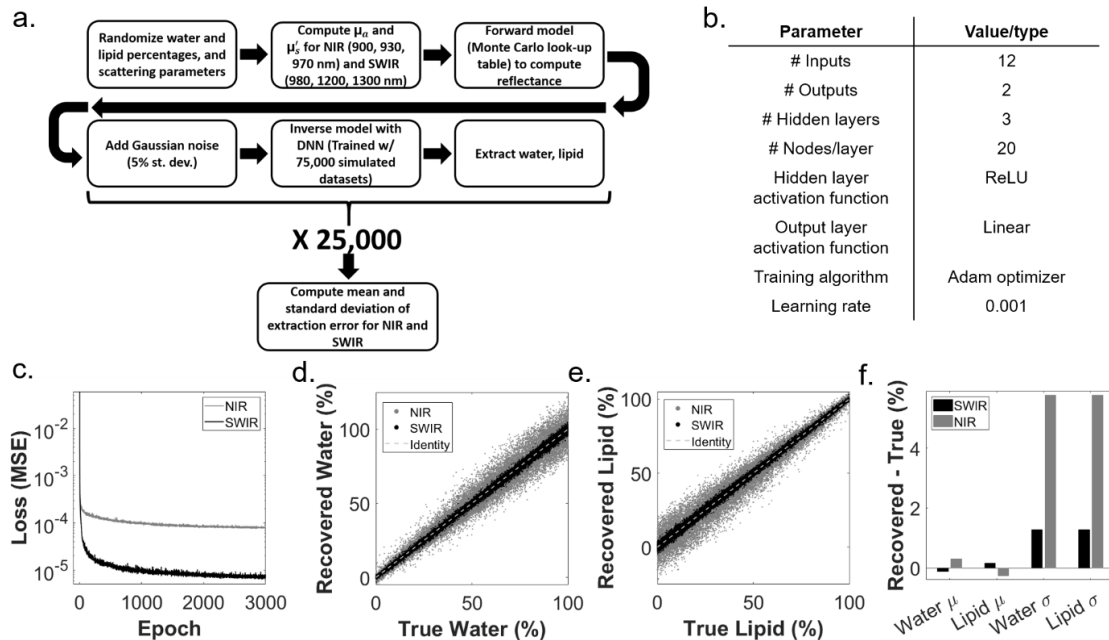


Figure 4.2. a) Simulation flowchart for the comparison of SWIR and NIR wavelengths. b) A table of architecture and training parameters for the DNNs used in this study. c) Loss (MSE) as a function of epoch during training for both the SWIR and NIR DNNs. d) All 25,000 recovered water values plotted vs. ground truth for SWIR and NIR wavelengths. e) Same as (d), but for lipid. f) Bar plots of the mean and standard deviation of differences between recovered and ground truth values for both SWIR and NIR.

2.4 Simulation results

Figure 4.2c illustrates the first indication that SWIR outperforms NIR in water and lipid recovery by showing the MSE during training of the two DNNs. The NIR MSE plateaued at around 10^{-4} , while the SWIR MSE dropped below 10^{-5} , indicating that, even prior to noise addition, the SWIR wavelengths were able to achieve a lower error in water and lipid extraction. Figures 4.2d and 4.2e show plots of recovered water and recovered lipid vs. their ground truths, respectively, for the 25,000 noise-added test sets described in Section 4.2.2. It is evident that for both water and lipid, the spread of recovered values more closely approaches the identity line for the SWIR wavelengths. This is especially true for high water/low lipid samples, with more comparable errors for near-100% lipid samples. Figure 4.2f quantifies this error, showing the mean and standard deviation of the difference between recovered and true values for all 25,000 sets of water and lipid values. For SWIR wavelengths, the errors for water and lipid recovery were $-0.1 \pm 1.3\%$ and $0.2 \pm 1.3\%$, respectively. The NIR error was higher, with values for water and lipid of $0.3 \pm 5.8\%$ and $-0.3 \pm 5.8\%$, respectively. These results suggest that the chosen SWIR wavelengths outperform NIR wavelengths in water and lipid recovery.

4.3 Instrument design and characterization

4.3.1 Printed circuit board and probe housing

The system consists of two components: a probe and a microcontroller (FRDM-K64F). The probe has one InGaAs PIN photodiode (G12180-30, Hamamatsu), four 980 nm LEDs (MTE9730CP), four 1200 nm LEDs (MTSM0012-843-IR) and four 1300 nm LEDs (MTSM0013-199-IR). All LEDs were purchased from Marktech. The photodiode

has an active area of $\sim 7 \text{ mm}^2$ and is sensitive to the 900 – 1700 nm wavelength range. The quantum efficiency at the illumination wavelengths is as follows: $\sim 63\%$ at 980 nm, $\sim 83\%$ at 1200 nm, $\sim 86\%$ at 1300 nm. LEDs were positioned at four different distances from the photodiode: 7, 10, 13, and 16 mm. These were the minimal distances achievable given the size of the optical elements. A transimpedance amplifier (OPA3S32), with three integrated switchable gain levels (0.5, 1, and 10 M Ω), was used to amplify and convert the photodiode current into voltage. This output voltage is read by a 16-bit analog to digital converter (ADC) embedded on the microcontroller. The intensity of the twelve LEDs is controlled with the 12-bit digital to analog converter (DAC) embedded on the microcontroller. The DAC output voltage is translated into current with an operational amplifier (TLV272IS-13) and NPN BJT (TTC1949-GR,LF). The microcontroller communicates with the probe through an HDMI connection, and the user can interact with the system with a python GUI. The sampling rate of the system was set to 1 Hz. The probe was adhered to skin surface with a Velcro strap or medical grade IV tape.

The SWIR probe is shown in Figure 4.3a and the probe with control hardware is shown in Figure 4.3b. Figure 4.3c shows the probe adhered to a forearm with Velcro. The probe was encased in a custom 3D-printed plastic housing with overall dimensions of 7.1 cm x 3.1 cm x 1.4 cm. Black silicone was used to isolate the optical elements. The silicone (Ecoflex-030, Smooth-On Inc.) and black dye (Silc-Pig, Smooth-On Inc.) are skin-safe, and were mixed together with a curing agent, de-gassed in a vacuum chamber for 15 minutes, and poured directly onto the exposed PCB surface.

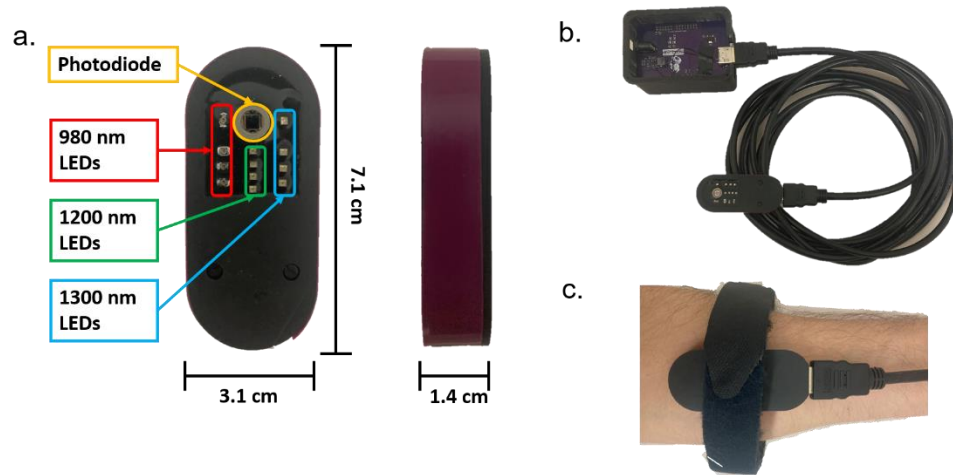


Figure 4.3. a) Sample-facing and side views of the encased SWIR probe, with optical elements labeled. b) The probe attached to its external control hardware (the microcontroller) via HDMI. c) An example of how the probe might be worn on the forearm of a human subject with a Velcro strap.

4.3.2 Performance characterization

Signal-to-noise ratio (SNR) and system drift were measured on a liquid optical phantom containing 1% Intralipid solution in water. Both the water and lipids absorb light at SWIR wavelengths, and the lipid micelles are highly scattering, creating a diffusive medium. The optical properties of 1% Intralipid across the SWIR probe wavelengths, calculated using Beer's Law and Mie theory, range from $0.04 - 0.13 \text{ mm}^{-1}$ for μ_a and $0.49 - 0.78 \text{ mm}^{-1}$ for μ'_s . The probe was wrapped tightly in clear plastic wrap and fixed in a slightly submerged position within the liquid phantom during measurement acquisition.

For the SNR measurement, the signal for each S-D pair was recorded for one minute at the fixed rate of 1 Hz. An initial background measurement was recorded with all of the LEDs off prior to the acquisition. SNR was then computed according to Equation 4.2:

$$(4.2) \quad 10 \cdot \log_{10} \left(\frac{\text{mean}(V_p - V_d)}{\text{std}(V_p - V_d)} \right)$$

where $V_p - V_d$ is the difference between each sample voltage and the background dark voltage. This dark subtraction was performed for all subsequent measurements. The SNRs for S-D separations ≤ 10 mm are >30 dB (Table 4.1).

For the drift measurement, the signal for each S-D pair was recorded for one hour. The voltage and time data were then fit to a linear function in order to quantify the slope, which was normalized to the initial voltage and multiplied by 100 to get units of %V/hr. Drift values for S-D separations ≤ 10 mm were $<1.1\%$ V/hour (Table 4.1).

Table 4.1. Performance characteristics of SWIR probe. SNR and drift values are shown for just the shortest and longest S-D separations (7 mm and 16 mm).

Parameter	Value (S-D separation)
Sampling Rate	1 Hz
SNR	
980 nm	36 dB (7 mm) 22 dB (16 mm)
1200 nm	42 dB (7 mm) 32 dB (16 mm)
1300 nm	41 dB (7 mm) 21 dB (16 mm)
Drift	
980 nm	$\leq 1\%$ V/hr (7 mm) $\leq 6\%$ V/hr (16 mm)
1200 nm	$\leq 1\%$ V/hr (7 mm) $\leq 4\%$ V/hr (16 mm)
1300 nm	$\leq 1\%$ V/hr (7 mm) $\leq 19\%$ V/hr (16 mm)

4.4 In vitro validation

4.3.1 Water-in-oil emulsion phantoms

Five water-in-oil emulsion phantoms were fabricated using soybean oil, water, and Triton X-100 as the emulsifier as described in Merritt et al [109]. Lipids concentrations were 65 – 85%, in steps of 5%. High ($\geq 65\%$) lipid concentrations were used to minimize scattering differences across phantoms, which occurs as a result of dependent scattering [123]. The SWIR probe was wrapped in clear plastic wrap and submerged in the emulsion phantoms. The probe optical elements were at least 1.5 cm from the phantom edge. 10 seconds of data were acquired at 1 Hz for each phantom measurement.

The processing pipeline is depicted in Figure 4.4. Measured sample and dark voltage measurements were first gain-corrected, and all sample voltage measurements were dark subtracted. Next, a forward model (Monte Carlo LUT) was used to map the known optical properties (μ_a and μ'_s) of the calibration phantom to a theoretical R_d value. As the photodiode operates linearly with incident light power, the R_d value was divided by the calibration measurement voltage to get a linear scaling factor, specific to each S-D pair. The corrected sample voltage was then multiplied by this scaling factor to compute R_d for that S-D pair.

The 85% lipid phantom was used as the calibration phantom. Beer's Law was used to compute μ_a , and the empirical formula given by Aernouts et al. was used to compute μ'_s [123]. This formula defines μ'_s as a function of wavelength and lipid concentration for emulsions up to 20% lipid concentration. However, the dependency on

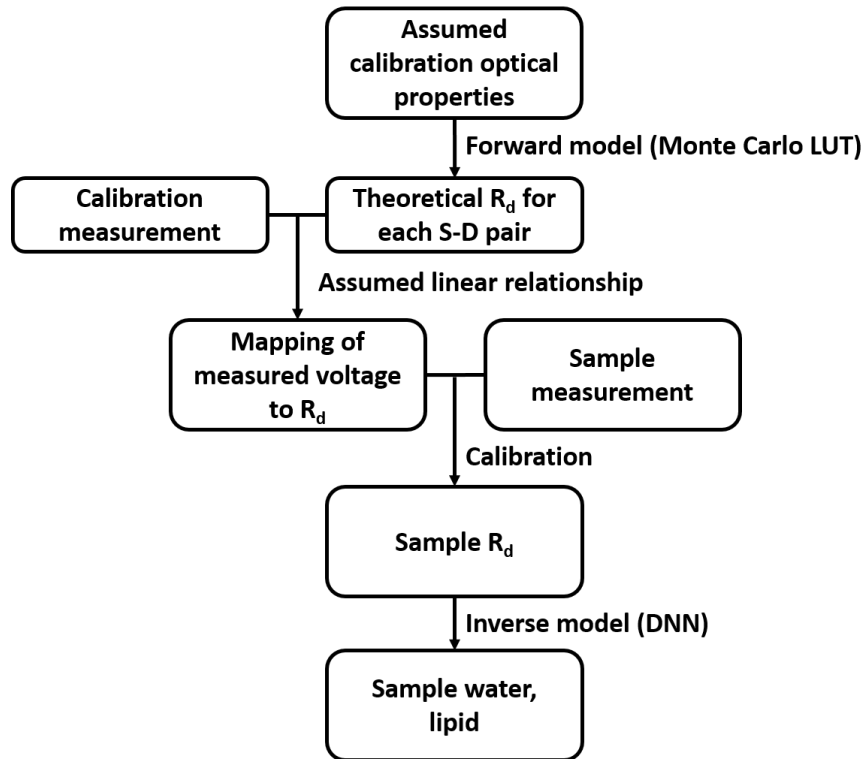


Figure 4.4. Data processing flowchart for in vitro validation experiments.

concentration nearly flattens at this upper limit due to dependent scattering. Therefore, we approximated the scattering values for 85% lipid as being equal to those of 20% lipid. These optical properties ranged from $0.04 - 0.13 \text{ mm}^{-1}$ for μ_a and $4.8 - 8.9 \text{ mm}^{-1}$ for μ'_s for the three measurements wavelengths. The DNN architecture was nearly identical to the DNN described in Section 2, except the 16 mm S-D separation measurements were removed due to low signal, resulting in 9 R_d inputs to the DNN. The DNN was trained with 75,000 sets of 9 R_d values. Additional information related to the training data is given in Supplementary Table S4.1.

Figures 4.5a and 4.5b show R_d vs. lipid concentration for the 7 mm and 10 mm separations. R_d increased as lipid concentration increased and water concentration

decreased. This is expected at 980 nm and 1300 nm as water has high absorption compared to lipid. While lipid's extinction coefficient at 1200 nm is slightly higher than water's, it is very close to an isosbestic point for the two chromophores, and the LED

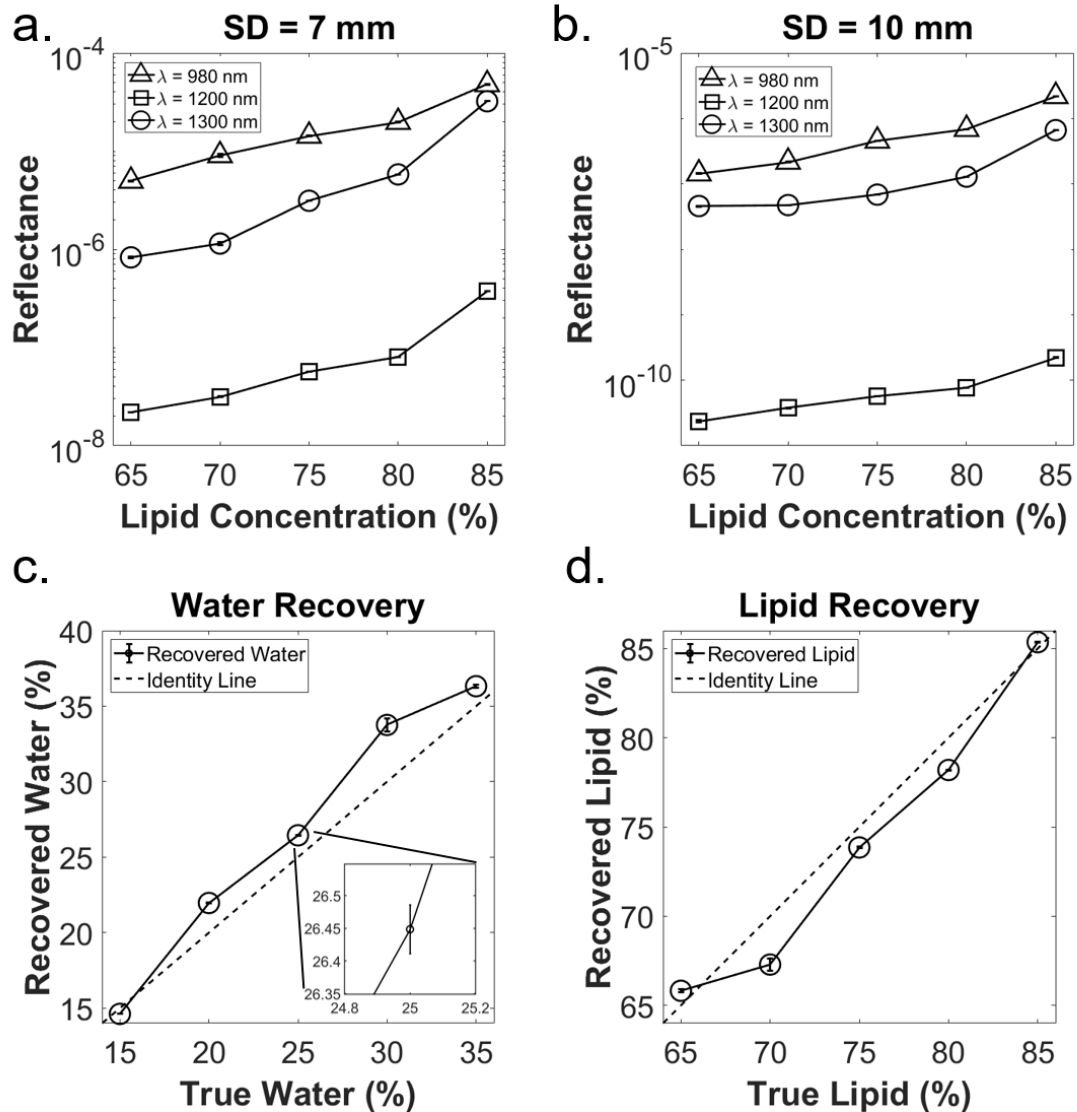


Figure 4.5. a) R_d vs. lipid concentration for S-D separation = 7 mm. b) Same as (a), but for SD separation = 10 mm. c) Recovered water vs. true water. The inset zooms in on the 25% water data point, showing the length of the error bars. These error bars refer to the standard deviation across the 10 consecutive time points that were acquired for each phantom. All four subfigures have these error bars, but they are barely visible when zoomed out. d) same as (c), but for lipid recovery.

illumination is broad (~80 nm full-width at half maximum, FWHM). This likely explains why the 1200 nm data appears to behave similarly to the other wavelengths. Also, R_d at 1200 nm is below that of both 980 nm and 1300 nm, which is consistent with the fact that both water and lipid have relatively high absorption here. Figures 4.5c and 4.5d show the correlations between recovered water and lipid, respectively, and their ground truth values. Both the water and lipid estimates follow the identity line closely. Removing the calibration phantom from the sample set, the mean \pm standard deviation of the error (defined as error = estimated – true) was $2.1 \pm 1.1\%$ for water recovery and $-1.2 \pm 1.5\%$ for lipid recovery. These results indicate that the SWIR probe is sensitive to variation in water and lipid content, and that given certain a priori information it can accurately quantify water and lipid content *in vitro*.

4.4.2 Dilution of oil-in-water emulsion with D_2O

To further validate the SWIR probe's sensitivity to water concentrations over a wide range, measurements were taken on a solution of 1% Intralipid in pure water (H_2O), which was serially diluted with 1% Intralipid in deuterium oxide (D_2O). D_2O molecules consist of two H^2 isotopes instead of H^1 , and their absorption is greatly reduced in the SWIR compared to H_2O molecules [124]. The initial 1% Intralipid solution was measured while in a well embedded in a diffusive solid silicone phantom. The well had a volume of 150 ml and was 2.5 cm deep. The SWIR probe was wrapped in clear plastic wrap and fixed at the surface of the solution, slightly submerged. Data acquisition was started and measurements were taken for 10 seconds at 1 Hz. Ten phantoms were

measured, with H₂O concentrations ranging from 99% to 9% in steps of 10%. The concentration of scattering lipid particles was preserved across all phantoms.

The 1% Intralipid in H₂O solution was used as the calibration phantom for this experiment, using the same known optical properties listed in Section 4.3.2. The Monte Carlo LUTs used to produce the DNN training data were generated with the index of refraction set to 1.33 to reflect the low lipid concentration. The combinations of H₂O and lipid were not constrained to sum to 100%, as the decreasing H₂O concentration was replaced by D₂O, not lipid. Furthermore, we assumed that D₂O absorption was collinear with H₂O absorption, but with 1/10th the magnitude, an estimate based on the extinction spectra reported in Wang et al [124]. This D₂O μ_a contribution was taken into account when generating the training data. Lastly, the scattering was fixed to be equal to that of 1% Intralipid. All 12 S-D pairs, spanning all four S-D separations, were input to this experiment's DNN. The DNN training data details are listed in Supplementary Table S4.1.

Figures 4.6a and 4.6b show R_d as a function of H₂O concentration for the 7 mm and 10 mm S-D separations respectively. The slope of R_d is steepest for 1300 nm, explained by the relatively high absorption from H₂O at this wavelength compared to the other two. We can assume these trends in R_d are strictly absorption-dependent since the scattering lipid particle concentration was held constant. Figure 4.6c shows the recovered H₂O concentration compared to the ground truth concentration. The estimates are within 4% of the ground truth from 49 – 99% H₂O and are within 10% for all data points. Over the full range of concentrations, the mean \pm standard deviation of the error was $3.1 \pm$

3.7%. This suggests that the SWIR probe has sensitivity to water at all concentrations, although the accuracy of water estimation appears to degrade at very low concentrations.

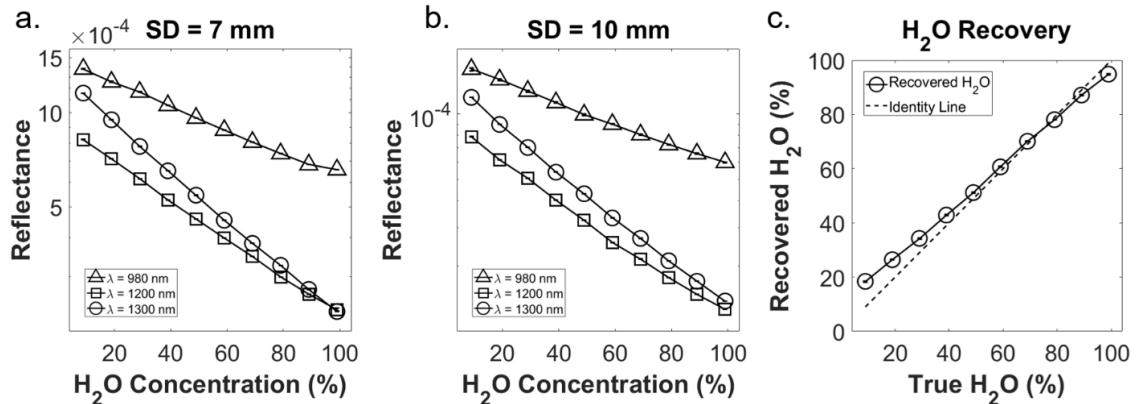


Figure 4.6. a) R_d vs H₂O concentration for S-D separation = 7 mm. (b) Same as (a), but for S-D separation = 10 mm. (c) Recovered H₂O vs. ground truth compared to the identity line. For all subfigures, error bars are presented as the standard deviation across the 10 consecutive time points for each phantom measurement. Error bars are present but barely visible.

4.5 Discussion

We have presented here a CW wearable SWIR probe with LEDs that span three wavelengths (980, 1200, 1300 nm) and four S-D separations (7, 10, 13, 16 mm), totaling 12 unique S-D pairs, and validated its ability to quantify water and lipid content *in vitro*. To our knowledge, this is the first wearable, LED-based SWIR probe capable of quantifying water and lipids.

There are a handful of prior reports showing that diffuse optical technologies are able to quantify *in vitro* water and lipid concentrations. Merritt et al. used a combined laser-based FD + broadband CW system with wavelengths from 650 – 1000 nm to estimate water and lipid concentrations of the same type of emulsion phantoms measured

here [109]. They included 12 phantoms in their study with water and lipid concentrations ranging from 35 – 94% and 6 – 63%, respectively. They reported water estimates within 2% of ground truth across this range, and lipid estimates within 9%. This error manifested as a constant offset and lipid recovery was highly linear. Lam et al. used a broadband CW system from 900 – 1000 nm to measure five similar emulsion phantoms with water and lipid concentrations ranging from 20 – 60% and 40 – 80%, respectively [107]. Errors ranged from 1.1 – 8.4%, with a mean error of $3.7 \pm 3.0\%$. Nachabe et al. achieved water and lipid errors of $<5\%$ over a wide variety of emulsion phantom types using a broadband CW system from 900 – 1600 nm [81]. In that study, both custom and commercial (butter and margarine) phantoms were measured, including sonication of custom emulsion phantoms to vary scattering while holding water and lipid concentration constant. This was the only other demonstration of CW diffuse optical measurements beyond 1000 nm of such phantoms besides ours. Our emulsion phantom results, with errors of $2.1 \pm 1.1\%$ for water recovery and $-1.2 \pm 1.5\%$ for lipid recovery, as well as $3.1 \pm 3.7\%$ in water recovery for the D₂O dilution experiment, compare well to these previous studies. Furthermore, the three other studies used broadband light sources allowing for the acquisition of hyperspectral data, whereas our SWIR probe minimizes the instrument design by using just three wavelengths.

One unique aspect of this study was the validation using the D₂O titration. Prior studies have utilized emulsions in which both water and lipid concentrations were changed simultaneously. This strategy is limited in one sense because the changes in lipid micelle concentrations also change optical scattering, making it difficult to know

whether observed water sensitivity is in part conflated with scattering sensitivity, especially when lipid concentration is <20%. Pilvar et al. demonstrated this by showing how a small increase from 1.5% to 2.5% Intralipid in water had a negligible effect on μ_a , but a significant effect on μ'_s . This makes it challenging to predict how performance would translate to applications in which only water concentration varies while scattering stays constant or changes in an unknown direction, which may occur in tissue. The D₂O experiment allowed for the confirmation of good sensitivity to water concentration changes over nearly the entire range of possible concentrations.

In this work we utilized DNNs trained with Monte Carlo simulated data as our inversion model. Other common inversion models, such as an iterative analytical solution based on the P1 approximation to the radiative transport equation, were not applicable here due to the relatively high absorption and low scattering at SWIR wavelengths. Others have utilized LUT-based inversion models that directly map R_d to μ_a and μ'_s on a per wavelength basis, but the addition of spectral constraints requires an iterative error minimization process, which is especially complex and computationally costly for highly discretized LUTs [125]–[127]. A DNN, in contrast, enables inverse solution to be found non-iteratively and rapidly. DNN inversion models have been utilized for a number of different diffuse optical modalities [128], including in our prior work [129], [130]. One important aspect of the DNN inversion used here was the incorporation of spectral constraints on the training data. While the DNN was not spectrally constrained per se, the constraint was effectively imposed on the inversion process through the training process.

Limitations of this study include the fact that constraints were applied to the training data in specific cases. For example, for the emulsion phantom study, it was assumed that water and lipid concentrations summed to 100%. In tissue samples, other chromophores such as hemoglobin, may be present in abundance, so this constraint would have to be removed. Our D₂O dilution experiment involved training a DNN without this constraint, but only one other chromophore (lipid) was present, and it was held constant. It remains to be seen if this method would be robust enough to quantify simultaneously varying amounts of both water and lipid in the presence of other chromophores. The DNN used for the D₂O experiment was further constrained as the scattering properties of the training data were fixed to that of 1% Intralipid solution in water. For future *in vivo* measurements, a scattering estimate could be assumed for different tissue types. That said, the water-in-oil emulsion phantom study did not incorporate a fixed scattering constraint, which suggests that the spectral constraints with our method may be sufficient for recovering water and lipid with unknown scattering in other applications.

In this work, we first confirmed the theoretical performance benefits of SWIR over NIR wavelengths in simulation, designed and fabricated a novel wearable SWIR probe, and characterized its performance. We then validated its sensitivity to water and lipid, and in doing so demonstrated its ability to quantify concentrations of these chromophores accurately *in vitro*. This opens the door to human studies that aim to test the functionality and utility of this probe *in vivo* for a variety of applications.

4.6 Supplementary Information

Table S4.1. Parameters that describe the training data used for each of the DNNs in this study.

Training data/DNN for:	g	n	Scattering amplitude (mm⁻¹)	Scattering slope	Water + Lipid = 1?	SD separations (mm)
SWIR vs. NIR comparison	0.7	1.435	Uniform distribution between 0.2 and 10	Normal distribution ($\mu = 1.29, \sigma = 0.52$)	Yes	7, 10, 13, 16
Emulsion phantom experiment	0.7	1.435	Uniform distribution between 0.2 and 10	Normal distribution ($\mu = 1.29, \sigma = 0.52$)	Yes	7, 10, 13
D ₂ O experiment	0.7	1.33	0.78	1.4	No	7, 10, 13, 16

CHAPTER FIVE: CONCLUSIONS AND FUTURE DIRECTIONS

5.1 Conclusions

To summarize the major accomplishments of this work, the validation of two custom wearable optical probes has been performed, and an initial clinical study was carried out involving the measurement of both traditional hemoglobin-based biomarkers and novel respiratory-related biomarkers.

The NIR wearable probe, which features an array of LEDs at 750 nm and 850 nm and silicon photodetectors, offers quantification of HbO₂ and HHb over a relatively wide spatial area. Measurements on tissue-simulating phantoms revealed high SNR, precision, and drift at most source-detector separations. Channel flow phantom measurements validated the ability of the probe to monitor changes in absorption spatially and temporally at a range of depths *in vitro*, and a cuff occlusion measurement on a human subject confirmed the ability to track expected trends in HbO₂ and HHb *in vivo*.

With this wearable NIR probe, hemodynamic oscillations at the respiratory rate were quantified in healthy and diseased breast tissue for the first time. A motion artifact human study (N=4) comparing the optical signal on breast tissue to a breast-mimicking phantom indicated that the majority of the signal measured during paced breathing was based in physiology, as opposed to motion. Repeatability measurements of paced breathing-related metrics (HbO_{2,PB}, HHb_{PB}, SrO₂) and traditional metrics (HbO_{2,abs}, HHb_{abs}, THb, StO₂) were then performed on an additional group of N=4 human subjects. These revealed high repeatability and low contralateral breast variation of traditional metrics and SrO₂, but relatively worse repeatability and higher variation for the other

breathing-related metrics. The initial clinical study of N=3 breast cancer patients demonstrated the ability of this probe to be practically implemented in the clinical setting at multiple time points during NAC. Some instances of both tumor contrast and treatment response separation were observed with multiple traditional and respiratory-related biomarkers, although the limited sample size prevented any conclusions from being drawn. In particular, the novel composite metric $\text{HbO}_{2,\text{PB}}/\text{HbO}_{2,\text{abs}}$ showed strong contrast between the pCR and non-pCR patients. A follow-up study with more subjects could further validate these findings.

Lastly, a custom wearable SWIR probe was designed and validated that offers quantification of water and lipid content – two additional biomarkers that have been shown to have prognostic value in monitoring breast cancer treatment response during NAC. Simulations of water and lipid recovery with both NIR and SWIR wavelengths first confirmed the theoretical advantage of using SWIR illumination. A probe was then fabricated with an array of 12 SWIR LEDs (980 nm, 1200 nm, 1300 nm) and a single InGaAs photodiode. A neural network was also designed as the inverse model for this probe, enabling high data processing speeds. Measurements on emulsion phantoms validated the ability of the probe to quantify water and lipid content simultaneously, and measurements during the dilution of an H_2O emulsion phantom with D_2O demonstrated water sensitivity over a wider range.

5.2 Future directions

While large-scale human studies were not conducted with either of the wearable probes described in this dissertation, both devices are ready to be implemented in such studies

going forward. With respect to the NIR probe, three future clinical studies can be envisioned that would help determine the clinical value of this device: 1) a continuation of the simultaneous paced breathing and traditional DOI biomarker measurements in the clinic, 2) a study involving just traditional DOI biomarker quantification in the clinic, and 3) a study involving traditional DOI biomarker quantification *at home*. The reason for separating clinical studies (1) and (2) is that the time and effort burden associated with the paced breathing protocol, particularly for the patients, might significantly slow down patient accrual. Examining this probe's clinical potential with traditional DOI biomarkers on a large scale would likely be the most impactful step toward clinical adoption. Clinical study (1) would be continued with a smaller patient population in order to determine if it is worth continuing to explore the paced breathing protocol and related metrics clinically. The third study proposed, involving the use of this probe at-home, would both expand the patient accrual pool even further and enable more frequent monitoring. There are non-trivial logistics that would need to be carefully planned, such as how to guide the patients to take repeatable measurements without having a trained operator present. However, if successful, this type of study could greatly expand the ability of clinicians to monitor treatment response and adapt healthcare decisions accordingly.

It would also be feasible to add SWIR probe measurements of water and lipid content to clinical studies (2) and/or (3) proposed above. This would enable measurement of all of the most commonly explored traditional DOI biomarkers in one study, exclusively acquired with wearable devices. To simplify the measurement procedure, it may be desirable to design a new wearable probe that has both NIR and SWIR LEDs, as

well as silicon and InGaAs photodiodes, so that all of these parameters can be quantified simultaneously with one device. Furthermore, while breast cancer treatment monitoring was the intended application initially, this SWIR probe could be extended to a variety of other applications, such as longitudinal body composition monitoring, hydration sensing, and volume status assessment.

The simplification and implementation of wearable devices in the clinic, and potentially at home, offers significant promise for more continuous and frequent monitoring of treatment response during NAC. Exploring new biomarkers further increases the likelihood of discovering metrics that have strong prognostic value, especially when multiple metrics can be combined to amplify this prognostic ability. The work described in this dissertation addresses both wearable device optimization and biomarker exploration, and in doing so represents a significant step toward clinical translation of diffuse optical imaging during NAC.

APPENDIX

As an extension of the flow phantom analysis described in Section 2.3.2, diffuse optical tomography (DOT) was also performed in order to create 3D volumetric reconstructions of the change in absorption during the flow phantom experiment. Tomographic reconstructions were performed in the Matlab version of Nirfast [90]. A slab geometry was assumed for the background phantom with optical properties listed in Section 2.3.2. The Rytov approximation with Tikhonov and spatially variant regularization were used to extract changes in absorption at each voxel from raw intensity values (normalized to baseline) for each NIR probe source-detector pair, which are methods described in Section 1.2.2. The NeuroDOT toolbox was utilized to implement these methods and visualize tomographic reconstructions in Matlab [131]. Figure A1 shows three slice views at the final time point of the flow phantom experiment for the channels with depths of 7 mm, 19 mm, and 28 mm. It is evident that at all three depths, a relatively accurate channel shape is reconstructed in each dimension, with X and Z slices showing long, tubular morphologies (along the length of the channel), and Y slices showing roughly circular morphologies (cross-sectional view of the circular side). Additionally, as seen in the Z slice reconstructions (the right panel of each row), the localization in X-Y space is very accurate. The X and Y slices reveal that localization accuracy in depth (Z-direction) is relatively high for the channel depths of 7 mm and 19 mm, but that the absorption depth is underestimated (too shallow) at the channel depth of 28 mm. This suggests that while depth localization accuracy diminishes beyond 20 mm, there still is sensitivity to absorption contrast at depths as great as 30 mm (and possibly deeper). While this

approach has not yet been extended to analysis of the *in vivo* breast data or SWIR probe data, the establishment of this framework will make the transition to those datasets more straightforward, should that route be explored. Regardless, it has provided valuable information about the limitations of the NIR probe's absorption sensitivity and localization capabilities.

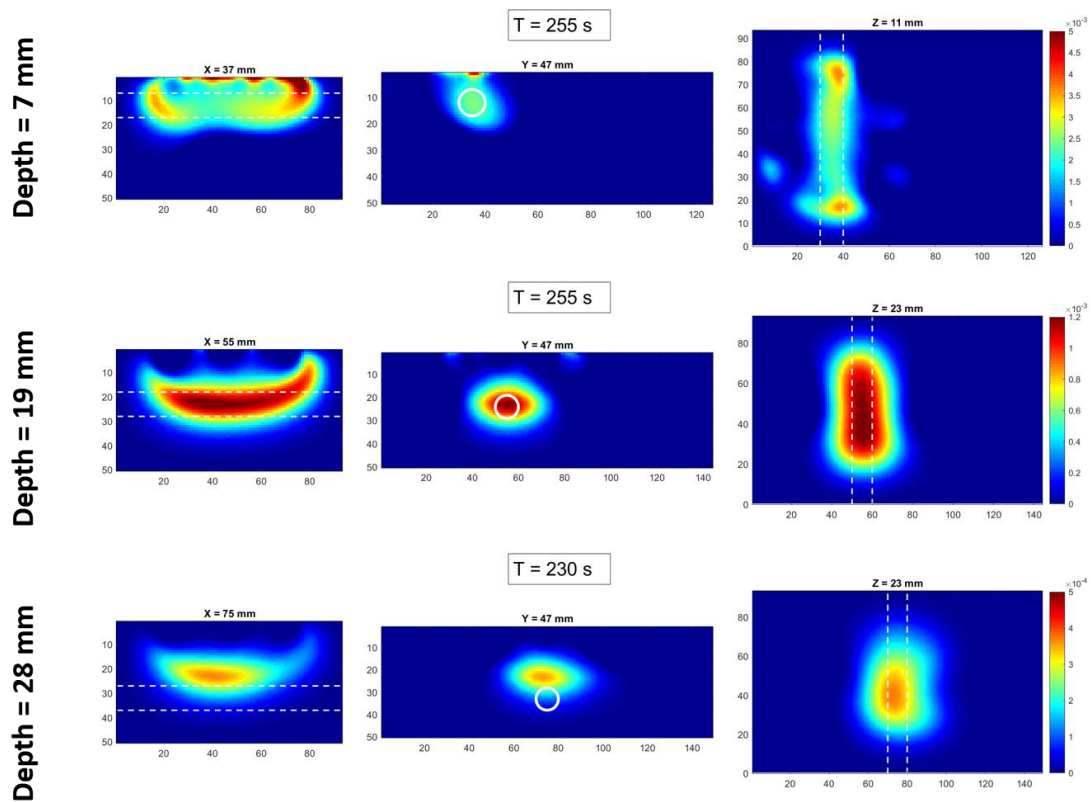


Figure A1. Tomographic reconstructions of channel flow phantom at final time point of experiment (nigrosin dye filling channel). The top row shows results for the channel whose upper edge was 7 mm from the surface of the background phantom, while the middle and bottom row show results for depths of 19 mm and 28 mm, respectively. The left slices show views along the length of the channel, the middle slices are cross-sectional views of the circular side of the channel, and the right slices are bird's-eye views of the channel. The colormap shows the reconstructed, normalized $\Delta\mu_a$ at each voxel. The regularization process distorts the scale of $\Delta\mu_a$, rendering the units arbitrary. The white dotted lines indicate the boundaries of the actual channel.

BIBLIOGRAPHY

- [1] Breastcancer.org, “https://www.breastcancer.org/symptoms/understand_bc/statistics.” 2022.
- [2] American Cancer Society, “<https://www.cancer.org/content/dam/cancer-org/research/cancer-facts-and-statistics/breast-cancer-facts-and-figures/breast-cancer-facts-and-figures-2017-2018.pdf>.” 2020.
- [3] National Cancer Institute, “SEER Cancer Stat Facts: Female Breast Cancer,” *National Cancer Institute*, 2020. [Online]. Available: <https://seer.cancer.gov/statfacts/html/breast.html>.
- [4] National Cancer Institute, “SEER Cancer Statistics Review, 1975-2015,” vol. 2005, no. July 1. p. 2016, 2005.
- [5] B. L. Murphy, C. N. Day, T. L. Hoskin, E. B. Habermann, and J. C. Boughey, “Neoadjuvant Chemotherapy Use in Breast Cancer is Greatest in Excellent Responders: Triple-Negative and HER2+ Subtypes,” *Annals of Surgical Oncology*, vol. 25, no. 8, pp. 2241–2248, 2018.
- [6] M. M. Kim *et al.*, “Pathologic complete response to neoadjuvant chemotherapy with trastuzumab predicts for improved survival in women with HER2-overexpressing breast cancer,” *Annals of Oncology*, vol. 24, no. 8, pp. 1999–2004, 2013.
- [7] E. R. Fisher, J. Wang, J. Bryant, B. Fisher, E. Mamounas, and N. Wolmark, “Pathobiology of preoperative chemotherapy: findings from the National Surgical Adjuvant Breast and Bowel (NSABP) protocol B-18,” *Cancer*, vol. 95, no. 4, pp. 681–695, 2002.
- [8] P. M. Spanheimer *et al.*, “The response to neoadjuvant chemotherapy predicts clinical outcome and increases breast conservation in advanced breast cancer,” *American Journal of Surgery*, vol. 206, no. 1, pp. 2–7, 2013.
- [9] W. F. Symmans *et al.*, “Measurement of residual breast cancer burden to predict survival after neoadjuvant chemotherapy,” *Journal of Clinical Oncology*, vol. 25, no. 28, pp. 4414–4422, 2007.
- [10] W. Haque, V. Verma, S. Hatch, V. Suzanne Klimberg, E. Brian Butler, and B. S. Teh, “Response rates and pathologic complete response by breast cancer molecular subtype following neoadjuvant chemotherapy,” *Breast Cancer Research and Treatment*, vol. 170, no. 3, pp. 559–567, 2018.
- [11] M. S. van Ramshorst *et al.*, “Neoadjuvant chemotherapy with or without

anthracyclines in the presence of dual HER2 blockade for HER2-positive breast cancer (TRAIN-2): a multicentre, open-label, randomised, phase 3 trial,” *The Lancet Oncology*, vol. 19, no. 12, pp. 1630–1640, 2018.

- [12] A. Santonja *et al.*, “Triple negative breast cancer subtypes and pathologic complete response rate to neoadjuvant chemotherapy,” *Oncotarget; Vol 9, No 41*, 2018.
- [13] L. J. Esserman, “Personalization of treatment is the way forward in care and trials,” *Clinical Cancer Research*, p. clincanres.0604.2020, Jan. 2020.
- [14] J. Heil *et al.*, “Eliminating the breast cancer surgery paradigm after neoadjuvant systemic therapy: current evidence and future challenges,” *Annals of Oncology*, vol. 31, no. 1, pp. 61–71, Jan. 2020.
- [15] H. M. Kuerer *et al.*, “Abstract P5-16-30: Feasibility trial for identification of patients for eliminating breast cancer surgery following neoadjuvant systemic therapy,” *Cancer Research*, vol. 77, no. 4 Supplement, pp. P5-16-30 LP-P5-16–30, Feb. 2017.
- [16] A. Francis *et al.*, “Abstract P5-16-14: NOSTRA PRELIM: A non randomised pilot study designed to assess the ability of image guided core biopsies to detect residual disease in patients with early breast cancer who have received neoadjuvant chemotherapy to inform the design of ,” *Cancer Research*, vol. 77, no. 4 Supplement, pp. P5-16-14 LP-P5-16–14, Feb. 2017.
- [17] H. Kuerer, “Eliminating Surgery After Systemic Therapy in Treating Patients With HER2 Positive or Triple Negative Breast Cancer,” *Clinicaltrials.gov*, 2017. [Online]. Available: <https://clinicaltrials.gov/ct2/show/study/NCT02945579>.
- [18] G. Cocconi, B. Di Blasio, G. Alberti, G. Bisagni, E. Botti, and G. Peracchia, “Problems in evaluating response of primary breast cancer to systemic therapy,” *Breast Cancer Research and Treatment Treat*, vol. 4, no. 4, pp. 309–313, 1984.
- [19] M. C. Segel, D. D. Paulus, and G. N. Hortobagyi, “Advanced primary breast cancer: assessment at mammography of response to induction chemotherapy,” *Radiology*, vol. 169, no. 1, pp. 49–54, 1988.
- [20] S. J. Vinnicombe *et al.*, “Primary breast cancer: mammographic changes after neoadjuvant chemotherapy, with pathologic correlation,” *Radiology*, vol. 198, no. 2, pp. 333–340, 1996.
- [21] N. M. Hylton *et al.*, “Locally advanced breast cancer: MR imaging for prediction of response to neoadjuvant chemotherapy--results from ACRIN 6657/I-SPY TRIAL,” *Radiology*, vol. 263, no. 3, pp. 663–672, 2012.

- [22] J. F. De Los Santos *et al.*, “Magnetic resonance imaging as a predictor of pathologic response in patients treated with neoadjuvant systemic treatment for operable breast cancer. Translational Breast Cancer Research Consortium trial 017,” *Cancer*, vol. 119, no. 10, pp. 1776–1783, 2013.
- [23] A. Quon and S. S. Gambhir, “FDG-PET and beyond: molecular breast cancer imaging,” *Journal of Clinical Oncology*, vol. 23, no. 8, pp. 1664–1673, 2005.
- [24] C. Rousseau *et al.*, “Monitoring of early response to neoadjuvant chemotherapy in stage II and III breast cancer by [18F]fluorodeoxyglucose positron emission tomography,” *Journal of Clinical Oncology*, vol. 24, no. 34, pp. 5366–5372, 2006.
- [25] A. Cerussi *et al.*, “Predicting response to breast cancer neoadjuvant chemotherapy using diffuse optical spectroscopy,” *Proceedings of the National Academy of Sciences of the United States of America*, vol. 104, no. 10, pp. 4014–4019, 2007.
- [26] A. E. Cerussi, V. W. Tanamai, D. Hsiang, J. Butler, R. S. Mehta, and B. J. Tromberg, “Diffuse optical spectroscopic imaging correlates with final pathological response in breast cancer neoadjuvant chemotherapy,” *Philosophical Transactions of the Royal Society A: Mathematical, Physical and Engineering Sciences*, vol. 369, no. 1955, pp. 4512–4530, 2011.
- [27] B. J. Tromberg *et al.*, “Imaging in breast cancer: diffuse optics in breast cancer: detecting tumors in pre-menopausal women and monitoring neoadjuvant chemotherapy,” *Breast Cancer Research*, vol. 7, no. 6, pp. 279–285, 2005.
- [28] B. J. Tromberg *et al.*, “Predicting Responses to Neoadjuvant Chemotherapy in Breast Cancer: ACRIN 6691 Trial of Diffuse Optical Spectroscopic Imaging,” *Cancer Research*, vol. 76, no. 20, pp. 5933–5944, 2016.
- [29] A. D. Klose, “The forward and inverse problem in tissue optics based on the radiative transfer equation: A brief review,” *Journal of Quantitative Spectroscopy and Radiative Transfer*, vol. 111, no. 11, pp. 1852–1853, 2010.
- [30] S. R. Arridge and M. Schweiger, “Image reconstruction in optical tomography,” *Philosophical Transactions of the Royal Society B: Biological Sciences*, vol. 352, no. 1354, pp. 717–726, 1997.
- [31] T. D. O’Sullivan, A. E. Cerussi, D. J. Cuccia, and B. J. Tromberg, “Diffuse optical imaging using spatially and temporally modulated light,” *Journal of Biomedical Optics*, vol. 17, no. 7, p. 71311, 2012.
- [32] D. J. Cuccia, F. Bevilacqua, A. J. Durkin, F. R. Ayers, and B. J. Tromberg, “Quantitation and mapping of tissue optical properties using modulated imaging,” *Journal of Biomedical Optics*, vol. 14, no. 2, p. 24012, 2009.

- [33] D. A. Boas, A. M. Dale, M. A. Franceschini, and M. A. Franceschini, “Diffuse optical imaging of brain activation: approaches to optimizing image sensitivity, resolution, and accuracy,” *NeuroImage*, vol. 23 Suppl 1, pp. S275–S288, 2004.
- [34] A. Sassaroli and S. Fantini, “Comment on the modified Beer–Lambert law for scattering media,” *Physics in Medicine and Biology*, vol. 49, no. 14, pp. N255–N257, Jul. 2004.
- [35] A. Corlu *et al.*, “Uniqueness and wavelength optimization in continuous-wave multispectral diffuse optical tomography,” *Optics Letters*, vol. 28, no. 23, pp. 2339–2341, Dec. 2003.
- [36] A. Li, Q. Zhang, J. P. Culver, E. L. Miller, and D. A. Boas, “Reconstructing chromosphere concentration images directly by continuous-wave diffuse optical tomography,” *Optics Letters*, vol. 29, no. 3, pp. 256–258, Feb. 2004.
- [37] Y. Xu, N. Iftimia, H. Jiang, L. L. Key, and M. B. Bolster, “Imaging of in vitro and in vivo bones and joints with continuous-wave diffuse optical tomography,” *Optics Express*, vol. 8, no. 7, pp. 447–451, Mar. 2001.
- [38] F. Scholkmann *et al.*, “A review on continuous wave functional near-infrared spectroscopy and imaging instrumentation and methodology,” *NeuroImage*, vol. 85, pp. 6–27, Jan. 2014.
- [39] D. A. Boas, T. Gaudette, and S. R. Arridge, “Simultaneous imaging and optode calibration with diffuse optical tomography,” *Optics Express*, vol. 8, no. 5, pp. 263–270, Feb. 2001.
- [40] H. Jiang, “Frequency-domain fluorescent diffusion tomography: a finite-element-based algorithm and simulations,” *Applied Optics*, vol. 37, no. 22, pp. 5337–5343, Aug. 1998.
- [41] Y. Yamada and S. Okawa, “Diffuse optical tomography: Present status and its future,” *Optical Review*, vol. 21, no. 3, pp. 185–205, 2014.
- [42] J. P. Culver, A. M. Siegel, J. J. Stott, and D. A. Boas, “Volumetric diffuse optical tomography of brain activity,” *Optics Letters*, vol. 28, no. 21, pp. 2061–2063, Nov. 2003.
- [43] D. Roblyer *et al.*, “Optical imaging of breast cancer oxyhemoglobin flare correlates with neoadjuvant chemotherapy response one day after starting treatment,” *Proceedings of the National Academy of Sciences of the United States of America*, vol. 108, no. 35, pp. 14626–14631, Aug. 2011.
- [44] O. Falou *et al.*, “Diffuse optical spectroscopy evaluation of treatment response in

women with locally advanced breast cancer receiving neoadjuvant chemotherapy,” *Translational oncology*, vol. 5, no. 4, pp. 238–246, Aug. 2012.

- [45] H. Soliman *et al.*, “Functional imaging using diffuse optical spectroscopy of neoadjuvant chemotherapy response in women with locally advanced breast cancer,” *Clinical Cancer Research*, vol. 16, no. 9, pp. 2605–2614, 2010.
- [46] S. Ueda *et al.*, “Near-infrared diffuse optical imaging for early prediction of breast cancer response to neoadjuvant chemotherapy: a comparative study using FDG-PET/CT,” *Journal of Nuclear Medicine*, vol. 57, no. 8, p. jnumed.115.167320, Mar. 2016.
- [47] A. E. Cerussi, N. S. Shah, D. Hsiang, A. Durkin, J. A. Butler, and B. J. Tromberg, “In vivo absorption, scattering, and physiologic properties of 58 malignant breast tumors determined by broadband diffuse optical spectroscopy,” *Journal of Biomedical Optics*, vol. 11, no. 4, pp. 1–6, Jul. 2006.
- [48] S. Ueda *et al.*, “Baseline tumor oxygen saturation correlates with a pathologic complete response in breast cancer patients undergoing neoadjuvant chemotherapy,” *Cancer Research*, vol. 72, no. 17, pp. 4318–4328, 2012.
- [49] S. Jiang *et al.*, “Predicting breast tumor response to neoadjuvant chemotherapy with diffuse optical spectroscopic tomography prior to treatment,” *Clinical Cancer Research*, vol. 20, no. 23, pp. 6006–6015, 2014.
- [50] M. L. Flexman *et al.*, “Digital optical tomography system for dynamic breast imaging,” *Journal of Biomedical Optics*, vol. 16, no. 7, p. 76014, 2011.
- [51] M. L. Flexman *et al.*, “Optical biomarkers for breast cancer derived from dynamic diffuse optical tomography,” *Journal of Biomedical Optics*, vol. 18, no. 9, p. 96012, 2013.
- [52] J. E. Gunther *et al.*, “Dynamic Diffuse Optical Tomography for Monitoring Neoadjuvant Chemotherapy in Patients with Breast Cancer,” *Radiology*, vol. 287, no. 3, pp. 778–786, Feb. 2018.
- [53] S. Lee and J. G. Kim, “Breast tumor hemodynamic response during a breath-hold as a biomarker to predict chemotherapeutic efficacy: preclinical study,” *Journal of Biomedical Optics*, vol. 23, no. 4, pp. 1–5, Apr. 2018.
- [54] A. Y. Sajjadi *et al.*, “Normalization of compression-induced hemodynamics in patients responding to neoadjuvant chemotherapy monitored by dynamic tomographic optical breast imaging (DTOBI),” *Biomedical Optics Express*, vol. 8, no. 2, pp. 555–569, Feb. 2017.

- [55] F. Yuan, H. A. Salehi, Y. Boucher, U. S. Vasthare, R. F. Tuma, and R. K. Jain, "Vascular Permeability and Microcirculation of Gliomas and Mammary Carcinomas Transplanted in Rat and Mouse Cranial Windows," *Cancer Research*, vol. 54, no. 17, pp. 4564 LP – 4568, Sep. 1994.
- [56] R. T. Tong, Y. Boucher, S. V Kozin, F. Winkler, D. J. Hicklin, and R. K. Jain, "Vascular Normalization by Vascular Endothelial Growth Factor Receptor 2 Blockade Induces a Pressure Gradient Across the Vasculature and Improves Drug Penetration in Tumors," *Cancer Research*, vol. 64, no. 11, pp. 3731 LP – 3736, Jun. 2004.
- [57] P. Cluzel, T. Similowski, C. Chartrand-Lefebvre, M. Zelter, J.-P. Derenne, and P. A. Grenier, "Diaphragm and Chest Wall: Assessment of the Inspiratory Pump with MR Imaging—Preliminary Observations," *Radiology*, vol. 215, no. 2, pp. 574–583, May 2000.
- [58] A. De Troyer and T. A. Wilson, "Action of the diaphragm on the rib cage," *Journal of Applied Physiology*, vol. 121, no. 2, pp. 391–400, Jun. 2016.
- [59] A. De Troyer and A. M. Boriek, "Mechanics of the Respiratory Muscles," *Comprehensive Physiology*. pp. 1273–1300, 01-Jul-2011.
- [60] R. A. Wise, J. L. Robotham, and W. R. Summer, "Effects of spontaneous ventilation on the circulation," *Lung*, vol. 159, no. 1, pp. 175–186, 1981.
- [61] L. Shekerdemian and D. Bohn, "Cardiovascular effects of mechanical ventilation," *Archives of Disease in Childhood*, vol. 80, no. 5, pp. 475 LP – 480, May 1999.
- [62] K. Toska and M. Eriksen, "Respiration-synchronous fluctuations in stroke volume, heart rate and arterial pressure in humans.," *The Journal of Physiology*, vol. 472, no. 1, pp. 501–512, Dec. 1993.
- [63] G. Billman, "Heart Rate Variability – A Historical Perspective ," *Frontiers in Physiology* , vol. 2. p. 86, 2011.
- [64] M. A. Franceschini *et al.*, "Near-infrared sioximetry: noninvasive measurements of venous saturation in piglets and human subjects," *Journal of Applied Physiology*, vol. 92, no. 1, pp. 372–384, 2002.
- [65] M. Wolf, G. Duc, M. Keel, P. Niederer, K. von Siebenthal, and H.-U. Bucher, "Continuous noninvasive measurement of cerebral arterial and venous oxygen saturation at the bedside in mechanically ventilated neonates," *Critical Care Medicine*, vol. 25, no. 9, 1997.
- [66] L. Bernardi, A. Gabutti, C. Porta, and L. Spicuzza, "Slow breathing reduces

- chemoreflex response to hypoxia and hypercapnia, and increases baroreflex sensitivity,” *Journal of Hypertension*, vol. 19, no. 12, 2001.
- [67] L. Bernardi, C. Porta, A. Gabutti, L. Spicuzza, and P. Sleight, “Modulatory effects of respiration,” *Autonomic Neuroscience*, vol. 90, no. 1, pp. 47–56, 2001.
- [68] L. Bernardi, G. Spadacini, J. Bellwon, R. Hajric, H. Roskamm, and A. W. Frey, “Effect of breathing rate on oxygen saturation and exercise performance in chronic heart failure,” *The Lancet*, vol. 351, no. 9112, pp. 1308–1311, 1998.
- [69] G. Bilo *et al.*, “Effects of Slow Deep Breathing at High Altitude on Oxygen Saturation, Pulmonary and Systemic Hemodynamics,” *PLOS ONE*, vol. 7, no. 11, p. e49074, Nov. 2012.
- [70] T. E. Dick, J. R. Mims, Y.-H. Hsieh, K. F. Morris, and E. A. Wehrwein, “Increased cardio-respiratory coupling evoked by slow deep breathing can persist in normal humans,” *Respiratory physiology & neurobiology*, vol. 204, pp. 99–111, Dec. 2014.
- [71] J. M. Kainerstorfer, A. Sassaroli, and S. Fantini, “Optical oximetry of volume-oscillating vascular compartments: contributions from oscillatory blood flow,” *Journal of Biomedical Optics*, vol. 21, no. 10, p. 101408, 2016.
- [72] J. M. Lynch *et al.*, “Noninvasive optical quantification of cerebral venous oxygen saturation in humans,” *Academic Radiology*, vol. 21, no. 2, pp. 162–167, Feb. 2014.
- [73] B. Chance, Q. Luo, S. Nioka, D. C. Alsop, and J. A. Detre, “Optical investigations of physiology: a study of intrinsic and extrinsic biomedical contrast,” *Philosophical Transactions of the Royal Society B: Biological Sciences*, vol. 352, no. 1354, pp. 707–716, 1997.
- [74] Q. Zhang, H. Ma, S. Nioka, and B. Chance, “Study of near infrared technology for intracranial hematoma detection,” *Journal of Biomedical Optics*, vol. 5, no. 2, 2000.
- [75] T. Muehleemann, D. Haensse, and M. Wolf, “Wireless miniaturized in-vivo near infrared imaging,” *Optics Express*, vol. 16, no. 14, pp. 10323–10330, 2008.
- [76] C. J. McManus, J. Collison, and C. E. Cooper, “Performance comparison of the MOXY and PortaMon near-infrared spectroscopy muscle oximeters at rest and during exercise,” *Journal of Biomedical Optics*, vol. 23, no. 1, pp. 1–14, Jan. 2018.
- [77] M. A. Fuglestad *et al.*, “A low-cost, wireless near-infrared spectroscopy device detects the presence of lower extremity atherosclerosis as measured by computed

- tomographic angiography and characterizes walking impairment in peripheral artery disease,” *Journal of Vascular Surgery*, vol. 71, no. 3, pp. 946–957, Mar. 2020.
- [78] G. Hu, Q. Zhang, V. Ivkovic, and G. E. Strangman, “Ambulatory diffuse optical tomography and multimodality physiological monitoring system for muscle and exercise applications,” *Journal of Biomedical Optics*, vol. 21, no. 9, pp. 1–14, Jul. 2016.
- [79] H. Atsumori *et al.*, “Development of wearable optical topography system for mapping the prefrontal cortex activation,” *Review of Scientific Instruments*, vol. 80, no. 4, p. 43704, 2009.
- [80] E. B. Elkin, C. Hudis, C. B. Begg, and D. Schrag, “The effect of changes in tumor size on breast carcinoma survival in the U.S.: 1975–1999,” *Cancer*, vol. 104, no. 6, pp. 1149–1157, Sep. 2005.
- [81] R. Nachabe, B. H. W. Hendriks, A. E. Desjardins, M. van der Voort, M. B. van der Mark, and H. J. C. M. Sterenborg, “Estimation of lipid and water concentrations in scattering media with diffuse optical spectroscopy from 900 to 1600 nm,” *Journal of Biomedical Optics*, vol. 15, no. 3, p. 37015, May 2010.
- [82] Y. Zhao *et al.*, “Shortwave-infrared meso-patterned imaging enables label-free mapping of tissue water and lipid content,” *Nature Communications*, vol. 11, no. 1, p. 5355, 2020.
- [83] S. S. Spink *et al.*, “High optode-density wearable diffuse optical probe for monitoring paced breathing hemodynamics in breast tissue,” *Journal of Biomedical Optics*, vol. 26, no. 6, pp. 1–20, Jun. 2021.
- [84] F. Teng *et al.*, “Wearable near-infrared optical probe for continuous monitoring during breast cancer neoadjuvant chemotherapy infusions,” *Journal of Biomedical Optics*, vol. 22, no. 1, pp. 1–8, Jan. 2017.
- [85] W. G. Zijlstra, A. Buursma, and O. W. van Assendelft, *Visible and Near Infrared Absorption Spectra of Human and Animal Haemoglobin determination and application*. VSP, 2000.
- [86] A. T. Eggebrecht *et al.*, “Mapping distributed brain function and networks with diffuse optical tomography,” *Nature photonics*, vol. 8, no. 6, pp. 448–454, Jun. 2014.
- [87] B. Khan *et al.*, “Improving optical contact for functional near-infrared brain spectroscopy and imaging with brush optodes,” *Biomedical Optics Express*, vol. 3, no. 5, pp. 878–898, May 2012.

- [88] L. Li, M. Cazzell, O. M. Babawale, and H. Liu, “Automated voxel classification used with atlas-guided diffuse optical tomography for assessment of functional brain networks in young and older adults,” *Neurophotonics*, vol. 3, no. 4, pp. 1–17, Oct. 2016.
- [89] K. L. Perdue, Q. Fang, and S. G. Diamond, “Quantitative assessment of diffuse optical tomography sensitivity to the cerebral cortex using a whole-head probe,” *Physics in medicine and biology*, vol. 57, no. 10, pp. 2857–2872, 2012.
- [90] H. Dehghani *et al.*, “Near infrared optical tomography using NIRFAST: Algorithm for numerical model and image reconstruction,” *Communications in numerical methods in engineering*, vol. 25, no. 6, pp. 711–732, Aug. 2008.
- [91] N. Shah, A. E. Cerussi, D. B. Jakubowski, D. Hsiang, J. A. Butler, and B. J. Tromberg, “Spatial variations in optical and physiological properties of healthy breast tissue,” *Journal of Biomedical Optics*, vol. 9, no. 3, pp. 534–540, May 2004.
- [92] T. Durduran *et al.*, “Bulk optical properties of healthy female breast tissue,” *Physics in Medicine and Biology*, vol. 47, no. 16, p. 302, Aug. 2002.
- [93] A. Torjesen, R. Istfan, and D. Roblyer, “Ultrafast wavelength multiplexed broad bandwidth digital diffuse optical spectroscopy for *in vivo* extraction of tissue optical properties,” *Journal of Biomedical Optics*, vol. 22, no. 3, pp. 1–8, Mar. 2017.
- [94] M. B. Applegate, C. A. Gómez, and D. M. Roblyer, “Modulation frequency selection and efficient look-up table inversion for frequency domain diffuse optical spectroscopy,” *Journal of Biomedical Optics*, vol. 26, no. 3, pp. 1–15, Mar. 2021.
- [95] L. Kocsis, P. Herman, and A. Eke, “The modified Beer–Lambert law revisited,” *Physics in Medicine and Biology*, vol. 51, no. 5, pp. N91–N98, Mar. 2006.
- [96] S. R. Arridge, M. Cope, and D. T. Delpy, “The theoretical basis for the determination of optical pathlengths in tissue: temporal and frequency analysis,” *Physics in Medicine and Biology*, vol. 37, no. 7, pp. 1531–1560, Jul. 1992.
- [97] M.-A. Franceschini, E. Gratton, D. M. Hueber, and S. Fantini, “Near-infrared absorption and scattering spectra of tissues *in vivo*,” in *Proceedings of SPIE--the International Society for Optical Engineering*, 1999, vol. 3597.
- [98] S. J. Matcher, M. Cope, and D. T. Delpy, “*In vivo* measurements of the wavelength dependence of tissue-scattering coefficients between 760 and 900 nm measured with time-resolved spectroscopy,” *Applied Optics*, vol. 36, no. 1, pp. 386–396, 1997.

- [99] H. M. Peterson *et al.*, “In vivo noninvasive functional measurements of bone sarcoma using diffuse optical spectroscopic imaging,” *Journal of Biomedical Optics*, vol. 22, no. 12, pp. 1–9, Dec. 2017.
- [100] C. M. Robbins, G. Raghavan, J. F. Antaki, and J. M. Kainerstorfer, “Feasibility of spatial frequency-domain imaging for monitoring palpable breast lesions,” *Journal of Biomedical Optics*, vol. 22, no. 12, pp. 1–9, Aug. 2017.
- [101] A. Samani, J. Zubovits, and D. Plewes, “Elastic moduli of normal and pathological human breast tissues: an inversion-technique-based investigation of 169 samples,” *Physics in Medicine and Biology*, vol. 52, no. 6, pp. 1565–1576, Mar. 2007.
- [102] T. A. Krouskop, T. M. Wheeler, F. Kallel, B. S. Garra, and T. Hall, “Elastic Moduli of Breast and Prostate Tissues under Compression,” *Ultrasonic Imaging*, vol. 20, no. 4, pp. 260–274, Oct. 1998.
- [103] R. V. Warren, “Development of Non-Invasive, Functional, Optical Imaging for Monitoring and Detecting Cardiovascular Disease,” University of California, Irvine, 2017.
- [104] J. M. Cochran *et al.*, “Tissue oxygen saturation predicts response to breast cancer neoadjuvant chemotherapy within 10 days of treatment,” *Journal of Biomedical Optics*, vol. 24, no. 2, pp. 1–11, 2018.
- [105] H. M. Peterson *et al.*, “Characterization of bony anatomic regions in pediatric and adult healthy volunteers using diffuse optical spectroscopic imaging,” *Journal of Biomedical Optics*, vol. 25, no. 8, p. 86002, Aug. 2020.
- [106] J. Q. M. Nguyen *et al.*, “Spatial frequency domain imaging of burn wounds in a preclinical model of graded burn severity,” *Journal of Biomedical Optics*, vol. 18, no. 6, pp. 1–8, Jun. 2013.
- [107] J. H. Lam, K. J. Tu, and S. Kim, “Narrowband diffuse reflectance spectroscopy in the 900-1000 nm wavelength region to quantify water and lipid content of turbid media,” *Biomedical Optics Express*, vol. 12, no. 6, pp. 3091–3102, 2021.
- [108] B. Song, X. Yin, Y. Fan, and Y. Zhao, “Quantitative spatial mapping of tissue water and lipid content using spatial frequency domain imaging in the 900- to 1000-nm wavelength region,” *Journal of Biomedical Optics*, vol. 27, no. 10, p. 105005, Oct. 2022.
- [109] S. Merritt *et al.*, “Comparison of Water and Lipid Content Measurements Using Diffuse Optical Spectroscopy and MRI in Emulsion Phantoms,” *Technology in Cancer Research & Treatment*, vol. 2, no. 6, pp. 563–569, Dec. 2003.

- [110] R. H. Wilson, K. P. Nadeau, F. B. Jaworski, B. J. Tromberg, and A. J. Durkin, "Review of short-wave infrared spectroscopy and imaging methods for biological tissue characterization," *Journal of Biomedical Optics*, vol. 20, no. 3, p. 30901, Mar. 2015.
- [111] H. Zhang, D. C. Salo, D. M. Kim, S. Komarov, Y.-C. Tai, and M. Y. Berezin, "Penetration depth of photons in biological tissues from hyperspectral imaging in shortwave infrared in transmission and reflection geometries," *Journal of Biomedical Optics*, vol. 21, no. 12, p. 126006, Dec. 2016.
- [112] M. M. M. Swamy, Y. Murai, K. Monde, S. Tsuboi, and T. Jin, "Shortwave-Infrared Fluorescent Molecular Imaging Probes Based on π -Conjugation Extended Indocyanine Green," *Bioconjugate Chemistry*, vol. 32, no. 8, pp. 1541–1547, Aug. 2021.
- [113] Z. Yu *et al.*, "High-Resolution Shortwave Infrared Imaging of Vascular Disorders Using Gold Nanoclusters," *ACS Nano*, vol. 14, no. 4, pp. 4973–4981, Apr. 2020.
- [114] Y. Che *et al.*, "In vivo live imaging of bone using shortwave infrared fluorescent quantum dots," *Nanoscale*, vol. 12, no. 43, pp. 22022–22029, 2020.
- [115] M. Saif *et al.*, "Non-invasive monitoring of chronic liver disease via near-infrared and shortwave-infrared imaging of endogenous lipofuscin," *Nature Biomedical Engineering*, vol. 4, no. 8, pp. 801–813, 2020.
- [116] A. Pilvar, J. Plutzky, M. C. Pierce, and D. M. Roblyer, "Shortwave infrared spatial frequency domain imaging for non-invasive measurement of tissue and blood optical properties," *Journal of Biomedical Optics*, vol. 27, no. 6, p. 66003, Jun. 2022.
- [117] D. J. Segelstein, "The complex refractive index of water," 1981.
- [118] T. J. Allen, P. C. Beard, A. Hall, A. P. Dhillon, and J. S. Owen, "Spectroscopic photoacoustic imaging of lipid-rich plaques in the human aorta in the 740 to 1400 nm wavelength range," *Journal of Biomedical Optics*, vol. 17, no. 6, p. 61209, May 2012.
- [119] S. Srinivasan *et al.*, "In Vivo Hemoglobin and Water Concentrations, Oxygen Saturation, and Scattering Estimates From Near-Infrared Breast Tomography Using Spectral Reconstruction¹," *Academic Radiology*, vol. 13, no. 2, pp. 195–202, Feb. 2006.
- [120] S. L. Jacques, "Optical properties of biological tissues: a review," *Physics in Medicine and Biology*, vol. 58, no. 11, pp. R37–R61, Jun. 2013.

- [121] Q. Fang and D. A. Boas, "Monte Carlo Simulation of Photon Migration in 3D Turbid Media Accelerated by Graphics Processing Units," *Optics Express*, vol. 17, no. 22, pp. 20178–20190, 2009.
- [122] S. T. Flock, S. L. Jacques, B. C. Wilson, W. M. Star, and M. J. C. van Gemert, "Optical properties of intralipid: A phantom medium for light propagation studies," *Lasers in Surgery and Medicine*, vol. 12, no. 5, pp. 510–519, Jan. 1992.
- [123] B. Aernouts, R. Van Beers, R. Watté, J. Lammertyn, and W. Saeys, "Dependent scattering in Intralipid® phantoms in the 600-1850 nm range," *Optics Express*, vol. 22, no. 5, pp. 6086–6098, 2014.
- [124] Y. Wang, W. Wen, K. Wang, P. Zhai, P. Qiu, and K. Wang, "Measurement of absorption spectrum of deuterium oxide (D_2O) and its application to signal enhancement in multiphoton microscopy at the 1700-nm window," *Applied Physics Letters*, vol. 108, no. 2, p. 021112, Jan. 2016.
- [125] G. M. Palmer and N. Ramanujam, "Monte Carlo-based inverse model for calculating tissue optical properties Part I: Theory and validation on synthetic phantoms," *Applied Optics*, vol. 45, no. 5, p. 1062, Feb. 2006.
- [126] P. Naglič, F. Pernuš, B. Likar, and M. Bürmen, "Estimation of optical properties by spatially resolved reflectance spectroscopy in the subdiffusive regime," *Journal of Biomedical Optics*, vol. 21, no. 9, p. 095003, Sep. 2016.
- [127] R. J. Hennessy, S. L. Lim, M. K. Markey, and J. W. Tunnell, "Monte Carlo lookup table-based inverse model for extracting optical properties from tissue-simulating phantoms using diffuse reflectance spectroscopy," *Journal of Biomedical Optics*, vol. 18, no. 3, p. 037003, Mar. 2013.
- [128] M. Ivančič, P. Naglič, F. Pernuš, B. Likar, and M. Bürmen, "Efficient estimation of subdiffusive optical parameters in real time from spatially resolved reflectance by artificial neural networks," *Optics Letters*, vol. 43, no. 12, pp. 2901–2904, 2018.
- [129] Y. Zhao, Y. Deng, F. Bao, H. Peterson, R. Istfan, and D. Roblyer, "Deep learning model for ultrafast multifrequency optical property extractions for spatial frequency domain imaging," *Optics Letters*, vol. 43, no. 22, pp. 5669–5672, 2018.
- [130] Y. Zhao, M. B. Applegate, R. Istfan, A. Pande, and D. Roblyer, "Quantitative real-time pulse oximetry with ultrafast frequency-domain diffuse optics and deep neural network processing," *Biomedical Optics Express*, vol. 9, no. 12, pp. 5997–6008, 2018.
- [131] A. T. Eggebrecht and J. P. Culver, "NeuroDOT: An extensible Matlab toolbox for

streamlined optical functional mapping,” in *Clinical and Preclinical Optical Diagnostics II*, 2019, vol. EB101, p. 11074_26.

CURRICULUM VITAE

Samuel S. Spink
1 Granite Street, Cambridge, MA 02139
Cell phone: (401) 714-3871
E-mail: sspink@bu.edu

EDUCATION

2017-Present	Boston University Boston, Massachusetts Ph.D. in Biomedical Engineering 4.0 GPA
2017-2020	Boston University Boston, Massachusetts M.S. in Biomedical Engineering 4.0 GPA
2013-2017	University of Rhode Island Kingston, Rhode Island B.S. in Biomedical Engineering Minor in Spanish 4.0 GPA

RESEARCH EXPERIENCE

Jan. 2018 – Present	Boston University, Department of Biomedical Engineering Boston, Massachusetts <i>Ph.D. Candidate</i> Adviser: Dr. Darren Roblyer <ul style="list-style-type: none"> • Developed and characterized a wearable continuous wave (CW) near infrared (NIR) diffuse optical probe for monitoring paced breathing hemodynamics in breast tumors <ul style="list-style-type: none"> ○ Designed and performed validation experiments <i>in vitro</i> with optical phantoms ○ Designed and performed a healthy volunteer study to test feasibility <i>in vivo</i> ○ Designed and began an ongoing clinical study to test feasibility in breast cancer patients at Boston Medical Center ○ Made modifications to the custom Labview program that controls the probe ○ Acquired all data and performed digital signal processing and data analysis in Matlab
---------------------	---

- Designed a shortwave infrared (SWIR) diffuse optical probe for monitoring tissue hydration and lipid content with deep learning
 - Informed design of probe by running simulations in Matlab to optimize wavelength selection and source/detector positions
 - Designed and performed validation experiments *in vitro* with optical phantoms
 - Acquired all data and performed data analysis in Matlab
 - Designed deep neural networks for faster processing in Python
- Developed and characterized a hyperspectral spatial frequency domain imaging (SFDI) system
 - Designed and performed validation experiments *in vitro* with optical phantoms
 - Aligned optics to ensure proper function of the device
 - Made modifications to the custom Labview program that controls the SFDI system
 - Acquired all data and performed data analysis in Matlab

Sept. 2014 -
August 2017

University of Rhode Island, Department of Chemistry

Kingston, Rhode Island

Undergraduate Researcher

Adviser: Dr. Matthew Kiesewetter

- Designed and synthesized more efficient and selective organocatalytic systems for the ring-opening polymerization of cyclic ester monomers
- Analyzed reactions and products via NMR spectroscopy and GPC

Fall 2016,
Spring 2017

University of Rhode Island, Department of Biomedical Engineering

Kingston, Rhode Island

Senior Capstone Design

Adviser: Dr. Ying Sun

- Designed a graphical user interface (GUI) for optic disc and cup characterization from fundus images
- Developed an algorithm that estimates the optic cup-to-disc area ratio from fundus images

TEACHING EXPERIENCE

Fall 2019

Boston University, Department of Biomedical Engineering

Boston, MA

Teaching Assistant

Biomedical Measurements I (BE 491)

Fall 2018

Boston University, Department of Biomedical Engineering

Boston, MA
 Teaching Assistant
 Linear Algebra and Statistical and Numerical Methods (BE 601/604)

Spring 2017 **University of Rhode Island, Department of Electrical, Computer, and Biomedical Engineering**
 Kingston, RI
 Teaching Assistant
 Biomedical Instrumentation Design Laboratory (BME 363)

Fall 2016 **University of Rhode Island, Department of Electrical, Computer, and Biomedical Engineering**
 Kingston, RI
 Teaching Assistant
 Biomeasurement Lab (BME 361)

PEER-REVIEWED PUBLICATIONS

1. **Spink, S. S.**; Pilvar, A.; Lin Wei, L.; Frias, J.; Anders, K.; Franco, S. T.; Rose, O.C.; Freeman, M.; Bag, G.; Huang, H.; Roblyer, D. "A shortwave infrared diffuse optical wearable probe for quantification of water and lipid content using deep learning". *Manuscript under review*, **2023**
2. **Spink, S. S.**[‡]; Teng, F.[‡]; Pera, V.; Peterson, H. M.; Cormier, T.; Sauer-Budge, A.; Chargin, D.; Brookfield, S.; Eggebrecht, A.; Ko, N.; Roblyer, D. "A high optode-density wearable diffuse optical probe for monitoring paced breathing hemodynamics in breast tissue". *J. Biomed. Opt.* **2021**, 26(6), 062708. [‡]Co-first authors.
3. Applegate, M. B.[‡]; **Spink, S. S.**[‡]; Roblyer, D. "Dual-DMD hyperspectral spatial frequency domain imaging (SFDI) using dispersed broadband illumination with a demonstration of blood stain spectral monitoring". *Biomed. Opt. Express* **2021**, 12, 676-688. [‡]Co-first authors.
4. Applegate, M.B.; Istfan, R.E.; **Spink, S. S.**; Tank, A.; Roblyer, D. "Recent advances in high speed diffuse optical imaging in biomedicine." *APL Photonics* **2020**, 5, 040802
5. **Spink, S. S.**[‡]; Fastnacht, K. V.[‡]; Dharmaratne, N. U.; Pothupitiya, J. U.; Datta, P. P.; Kiesewetter, E. T.; Kiesewetter, M. K. "Bis- and Tris-Urea H-Bond Donors for Ring-Opening Polymerization: Unprecedented Activity and Control from an Organocatalyst." *ACS Macro Letters* **2016**, 5 (8), 982-986. [‡]Co-first authors.
6. **Spink, S. S.**; Kazakov, O. I.; Kiesewetter, E. T.; Kiesewetter, M. K. "Rate Accelerated Organocatalytic Ring-Opening Polymerization of L-Lactide via the Application of a Bis(thiourea) H-bond Donating Cocatalyst." *Macromolecules* **2015**, 48 (17), 6127–6131.

ORAL PRESENTATIONS

1. **Spink, S. S.**; Eggebrecht, A.; Ko, N.; Roblyer, D. "Paced breathing hemodynamics in breast tumors measured with a high-optode density wearable diffuse optical probe." *SPIE Photonics West*, Virtual recorded talk (originally scheduled for San Francisco, CA), **March 2021**.

2. **Spink, S. S.;** Teng, F.; Pera, V.; Peterson, H.; Eggebrecht, A.; Ko, N.; Roblyer, D. "High Optode-density Wearable Probe for Monitoring Breast Tumor Dynamics during Neoadjuvant Chemotherapy." *OSA BioMed, Virtual* (originally scheduled for Ft. Lauderdale, FL), **April 21, 2020.**
3. **Spink, S. S.;** Teng, F.; Pera, V.; Peterson, H.; Eggebrecht, A.; Ko, N.; Roblyer, D. "High optode-density wearable probe for monitoring breast tumor hemodynamics: normal volunteer and initial clinical results." *SPIE Photonics West, San Francisco, CA*, **February 2, 2020.**
4. **Spink, S. S.;** Teng, F.; Pera, V.; Peterson, H.; Eggebrecht, A.; Ko, N.; Roblyer, D. "A rigid-flex wearable probe for monitoring breast tumor hemodynamics during neoadjuvant chemotherapy." *SPIE Photonics West, San Francisco, CA*, **February 1, 2020.**
5. **Spink, S. S.;** Teng, F.; Pera, V.; Peterson, H.; Ko, N.; Roblyer, D. "High optode-density wearable probe for monitoring breast tumor dynamics during neoadjuvant chemotherapy." *NESBO Conference, Cambridge, MA*, **October 15, 2019.**
6. **Spink, S. S.;** Teng, F.; Pera, V.; Peterson, H.; Ko, N.; Roblyer, D. "High optode-density wearable probe for monitoring tumor dynamics during neoadjuvant chemotherapy." *SPIE Photonics West, San Francisco, CA*, **February 2, 2019.**

POSTER PRESENTATIONS

1. **Spink, S. S.;** Pilvar, A.; Lin Wei, L.; Roblyer, D. "Quantifying tissue hydration and lipid content with shortwave infrared (SWIR) optical measurements and deep learning." *Boston University Photonics Center Symposium, Boston, MA*, **December 1, 2022.**
2. **Spink, S. S.;** Eggebrecht, A.; Ko, N.; Roblyer, D. "Paced breathing hemodynamics in healthy and cancerous breast tissue measured with a high-optode density wearable diffuse optical probe." *Gordon Research Conference on Optics and Photonics in Medicine and Biology, Lewiston, ME*, **July 13, 2022.**
3. **Spink, S. S.;** Teng, F.; Pera, V.; Peterson, H.; Eggebrecht, A.; Ko, N.; Roblyer, D. "High optode-density wearable probe for monitoring breast tumor dynamics during neoadjuvant chemotherapy." *Boston University Precision Diagnostics Center Symposium, Boston, MA*, **February 24, 2020.**
4. **Spink, S. S.;** Teng, F.; Pera, V.; Peterson, H.; Eggebrecht, A.; Ko, N.; Roblyer, D. "High optode-density wearable probe for monitoring breast tumor dynamics during neoadjuvant chemotherapy." *Boston University Photonics Center Symposium, Boston, MA*, **November 21, 2019.**
5. **Spink, S. S.;** Apatow, M.; Goyette, S.; Wu, J.; Sun, Y. "GUI-Based Optic Disc and Cup Characterization from Fundus Images." *NEBEC, Newark, NJ*, **March 31, 2017.**
6. **Spink, S. S.;** Kazakov, O. I.; Kiesewetter, E. T.; Kiesewetter, M. K. "Unprecedented rate acceleration of organocatalytic ring-opening polymerization through the application of Bis- and Tris- (thio)urea H- bond donors." *INBRE SURF Conference, Kingston, RI*, **July 31, 2016.**
7. **Spink, S. S.;** Kiesewetter, E. T.; Kiesewetter, M. K. "Rate accelerated organocatalytic ring-opening polymerization via the application of a bistiourea H-bond donating cocatalyst." *INBRE SURF Conference, Kingston, RI*, **July 31, 2015.**
8. **Spink, S. S.;** Kiesewetter, E. T.; Kiesewetter, M. K. "Organocatalytic ring-opening polymerization of d-valerolactone with tethered co-catalysts." *INBRE SURF Conference, Kingston, RI*, **August 1, 2014.**

HONORS/AWARDS

2017	Biomedical Engineering Excellence Award
2016-2017	Barry M. Goldwater Scholarship
2016-2017	Peter A. Pelletier Endowed Scholarship
2016	URI Undergraduate Student Research and Scholarship Excellence Award
2016	IDeA Network (INBRE) Summer Undergraduate Research Fellowship
2016	Phi Beta Kappa Honor Society
2015-2016	URI College of Engineering Scholarship
2015	IDeA Network (INBRE) Summer Undergraduate Research Fellowship
2014-2015	Walter Schmid Engineering Scholarship
2014	IDeA Network (INBRE) Summer Undergraduate Research Fellowship
2013-2017	URI Centennial Scholarship
2013-2017	Dean's List

RELEVANT SKILLS

Computer Applications: Matlab, Multisim, Microsoft Office, some experience with KiCad

Programming: Matlab, Labview, some experience in Python

Hardware: Electronics test equipment

Fields of Study/Lab Skills: Diffuse optical imaging (DOI), spatial frequency domain imaging (SFDI), digital signal processing, deep neural network design in Python with TensorFlow and Keras, nuclear magnetic resonance (NMR) spectroscopy, gel permeation chromatography (GPC), ring-opening polymerization (ROP)